

# UNIVERSITÀ DEGLI STUDI DI PADOVA

Dipartimento di Fisica e Astronomia “Galileo Galilei”

Master Degree in Astrophysics and Cosmology

Final Dissertation

## Stochastic Gravitational Wave Background from Primordial Black Holes

Thesis supervisor

Prof. Alvise Raccanelli

Candidate

Alberto Magaraggia

Thesis co-supervisors

Dr. Angelo Ricciardone

Dr. Sarah Libanore

Academic Year 2022/2023



# Abstract

One of the biggest problems in modern cosmology is to assess the nature of dark matter. We propose Primordial Black Holes (PBHs) as a possible candidate and we investigate how this scenario can be probed with the Stochastic Gravitational Wave Background (SGWB). We begin by briefly analyzing the  $\Lambda$ CDM model, summarizing the main tools used for cosmology. After having described how PBHs could have formed in the early Universe, we present recent observational constraints on their masses. Moreover, we explore the possibility that two Primordial Black Holes form a binary either in the early Universe by decoupling from the Hubble flow, or in the late Universe by gravitational capture. Then, we investigate a tool to probe PBHs as dark matter candidate: we introduce gravitational waves, and in particular the stochastic gravitational wave background. We describe the SGWB that could be generated from PBH binaries and we review a numerical code for the computation of the SGWB from Astrophysical Black Holes. The final goal of this Master Thesis is to improve such tool so to include the SGWB from PBH binaries. Finally, we present the analysis of the SGWB from 5 different mass functions (3 monochromatic and 2 extended), both for early and late binaries. We conclude by emphasizing the importance of the SGWB as a new tool to be used by the next generation of gravitational wave detectors.



# Contents

<b>Contents</b>	<b>i</b>
<b>Physical constants</b>	<b>iii</b>
<b>Introduction</b>	<b>v</b>
<b>1 The <math>\Lambda</math>CDM Model</b>	<b>1</b>
1.1 The homogeneous and isotropic Universe . . . . .	1
1.1.1 Geometry of the Universe . . . . .	1
1.2 Einstein Field Equations . . . . .	2
1.3 The evolution of the scale factor . . . . .	3
1.4 A multifluid model . . . . .	5
1.5 Redshift . . . . .	6
1.6 Brief thermal history of the Universe . . . . .	7
<b>2 Primordial Black Holes</b>	<b>9</b>
2.1 Introduction . . . . .	9
2.2 The Dark Matter problem . . . . .	10
2.3 Formation mechanisms . . . . .	11
2.3.1 Other mechanisms . . . . .	13
2.4 Initial conditions . . . . .	13
2.5 Constraints on abundance . . . . .	14
2.5.1 Evaporation constraints . . . . .	15
2.5.2 Lensing constraints . . . . .	15
2.5.3 Gravitational Waves constraints . . . . .	15
2.5.4 Accretion constraints . . . . .	16
2.5.5 Dynamical constraints . . . . .	16
2.5.6 Summary of constraints . . . . .	17
2.6 Claimed signatures . . . . .	19
2.6.1 Lensing evidence . . . . .	19
2.6.2 Dynamical and Accretion evidence . . . . .	19
2.6.3 LIGO-Virgo upper limits . . . . .	19
2.7 Binary Formation . . . . .	20
2.7.1 PBH binary formation in the early Universe . . . . .	20
2.7.2 PBH binary formation in the late Universe . . . . .	22
2.7.3 Hyperbolic encounters . . . . .	23
<b>3 Gravitational Waves</b>	<b>25</b>
3.1 Introduction to GWs . . . . .	25
3.2 Indirect evidence of GWs . . . . .	28
3.3 Gravitational-Wave Detectors . . . . .	29
3.3.1 LIGO-Virgo-KAGRA collaboration . . . . .	29
3.3.2 Pulsar Timing Array and SKA . . . . .	30
3.3.3 LISA . . . . .	31

3.3.4 Einstein Telescope . . . . .	31
3.4 Stochastic GW Background . . . . .	31
<b>4 SGWB</b>	<b>35</b>
4.1 SGWB from astrophysical sources . . . . .	36
4.1.1 CLASS_GWB . . . . .	37
4.2 SGWB from early PBH binaries . . . . .	41
4.3 SGWB from late PBH binaries . . . . .	43
<b>5 Original results</b>	<b>47</b>
5.1 Modification of CLASS_GWB . . . . .	47
5.2 Initial parameters' setup . . . . .	48
5.3 General considerations . . . . .	50
5.4 Monochromatic mass function . . . . .	51
5.4.1 $M_{PBH} = 30 M_\odot$ . . . . .	51
5.4.2 $M_{PBH} = 0.1 M_\odot$ . . . . .	53
5.4.3 $M_{PBH} = 10^{-5} M_\odot$ . . . . .	53
5.5 Extended mass function . . . . .	55
5.5.1 Log-normal mass function . . . . .	56
5.5.2 Power law mass function . . . . .	57
5.6 Future prospects . . . . .	58
<b>6 Conclusions</b>	<b>59</b>
<b>A Plots</b>	<b>61</b>
<b>Bibliography</b>	<b>67</b>

# Physical constants

List of the approximate values of the flat- $\Lambda$ CDM physical constants used in this thesis. The cosmological parameters here reported are the best-fit estimation from *Planck 2018*. [1]

Any physical quantity in this Master thesis will be either defined here or once presented for the first time.

- Speed of light:  $c = 299792458 \text{ m s}^{-1}$
- Gravitational constant:  $G = 6.67 \cdot 10^{-11} \text{ m}^3 \text{kg}^{-1} \text{s}^{-2}$
- Mass of the Sun:  $M_{\odot} = 1.989 \cdot 10^{30} \text{ kg}$
- Hubble constant:  $H_0 = 67.66 \text{ km s}^{-1} \text{Mpc}^{-1} = 2.25 \cdot 10^{-18} \text{ s}^{-1}$
- Critical density today:  $\rho_{c,0} = \frac{3H_0^2}{8\pi G} = 8.58 \cdot 10^{-27} \text{ kg m}^{-3}$
- Radiation density:  $\Omega_R = \frac{\rho_R}{\rho_{c,0}} = 5.39 \cdot 10^{-5}$
- Barion density:  $\Omega_B = \frac{\rho_B}{\rho_{c,0}} = 0.05$
- Dark Matter density:  $\Omega_{DM} = \frac{\rho_{DM}}{\rho_{c,0}} = 0.26$
- Matter density:  $\Omega_M = \frac{\rho_m}{\rho_{c,0}} = \Omega_{DM} + \Omega_B = 0.31$
- Cosmological constant density:  $\Omega_{\Lambda} = \frac{\rho_{\Lambda}}{\rho_{c,0}} = 0.69$
- Boltzmann constant:  $k_B = 1.380649 \cdot 10^{-23} \text{ m}^2 \text{kg s}^{-2} \text{K}^{-1}$



# Introduction

The Standard Modern of Cosmology explains quite well our Universe. Still, it is incomplete, and many open questions need to be addressed: one of them is the nature of Dark Matter, that from decades puzzles the researchers. Many explanations have been proposed, but no conclusive solution has been reached. Appealing candidates to solve the Dark Matter problem are Primordial Black Holes (PBHs), and the interest towards them increased and renewed after the detection of the first gravitational wave event. Moreover, Gravitational-Wave Astronomy is now one of the most active fields of research: an increasing number of different detectors have been built and are planned for the next future. We can now use gravitational waves as a new tool to understand the Universe.

Indeed, the work of this thesis aims to characterize the interplay between Primordial Black Holes and gravitational waves: if Primordial Black Holes are present in the Universe, they should interact gravitationally between each others, and their signatures should be visible at some level. Rather than gravitational waves from single, resolved events, we analyze the possibility to detect the Stochastic Gravitational Wave Background (SGWB), i.e. the sum of all the unresolved contributions throughout the entire history of the Universe. To do so, a precise analysis of all the interactions between PBHs and the other components of the Universe is needed. The first step in this direction is to characterize the contribution of Primordial Black Hole binary inspirals and mergers. These, together with the analogous contribution from astrophysical black holes, will determine the main contribution to the gravitational wave background.

To model such processes, the first thing is to understand the way two Primordial Black Holes gravitationally bound. This can happen at two distinct moment in the history of the Universe: primordially, if they effectively decouple from the Hubble flow, or in the late Universe by gravitational capture. We analyze the characteristics of these two populations of PBH binaries and we compute the background they produce. To do so, we adopt and opportunely improve the numerical code CLASS\_GWB, a state of the art tool for the computation of the stochastic gravitational wave background. By studying the detectability of planned gravitational wave detectors, we show that the SGWB from PBH binaries will be seen in the near future. In case this detection will not occur, this will introduce new constraints on the existence and abundance of PBHs of different masses in our Universe, providing a new tool to constrain many theoretical models.

This Master thesis is organized as follows. In Chapter 1 we introduce the  $\Lambda$ CDM model and we review the main results of modern Cosmology. In Chapter 2 we propose Primordial Black Holes as a possible candidate to solve the dark matter problem; we review their formation mechanisms and the current constraints on their abundance. Moreover, we analyze the possibility of two PBHs forming binary systems, either in the early Universe by decoupling from the Hubble flow, or in the late Universe by gravitational capture. In Chapter 3 we introduce gravitational waves and we present the current and planned experiments to detect them. In Chapter 4 we characterize the stochastic gravitational wave Background and we analyze its contribution from astrophysical sources and from the two binary PBH populations presented. Moreover, we describe a robust numerical approach to compute the SGWB from astrophysical black holes. Chapter 5 describes the work we realized in the context of this thesis: we implement the tool required to estimate the SGWB from primordial black hole binaries and we analyze PBH binaries with 5 mass distributions. We finally compute the expected background signal and we discuss the current and future prospects that such kind of analysis implies. All the outputs required to understand and interpret our results are reported in Chapter 5 and Appendix 6.



# Chapter 1

## The $\Lambda$ CDM Model

Over a century of observations of the Universe, together with extensive theoretical studies, helped us to outline the Standard Model of Cosmology, the so-called  $\Lambda$ CDM model, which currently represents the best explanation of the observable Universe. The  $\Lambda$  indicates the cosmological constant responsible for the accelerated expansion of the Universe, while the CDM stands for the dominant form of matter in the Universe, the Cold Dark Matter. Quite interestingly, the nature of these two major components of the Universe represents two of the most puzzling questions of modern cosmology. In this chapter we will review the basics of the  $\Lambda$ CDM model, and we will use the convention  $c = 1$  for the speed of light.

### 1.1 The homogeneous and isotropic Universe

Modern Cosmology is based on the so-called *Cosmological Principle*: the Universe is thought to be homogeneous and isotropic, at least on sufficiently large scales (over  $\sim 100$  Mpc) [2]. This is equivalent to state that every point of the Universe is like any other one (homogeneity) and that every direction is like any other one (isotropy). In other words, “Viewed on a sufficiently large scale, the properties of the Universe are the same for all observers” [3].

#### 1.1.1 Geometry of the Universe

The main idea to describe a homogeneous and isotropic Universe is to find a metric that reflects such properties: this is the case of the Friedmann-Lemaître-Robertson-Walker (FLRW) metric, that is symmetric under rotations and spatial translations [4]. The geometry described is encoded in the metric tensor  $g_{\mu\nu}$ , or equivalently in the line element:

$$ds^2 = g_{\mu\nu} dx^\mu dx^\nu \quad (1.1)$$

which represents the spacetime interval between two points  $x^\mu$  and  $x^\mu + dx^\mu$ . In particular, the FLRW line element can be written as:

$$ds^2 = -(dt)^2 + a^2(t) d\sigma^2 = -(dt)^2 + a^2(t) \tilde{g}_{ij} dx^i dx^j, \quad (1.2)$$

where  $t$  is the cosmic time,  $a(t)$  is the scale factor,  $\tilde{g}_{ij}$  is the spatial metric tensor and  $i, j$  indicate the spatial indices. In particular, the scale factor describes how the Universe size evolves in time, expanding if  $a(t) > 0$ , contracting if  $a(t) < 0$  or maintaining the same size if  $a(t) = \text{const.}$

Killing vectors are vectors oriented in the direction of a symmetry. The spatial part  $d\sigma^2$  of the FLRW metric is maximally symmetric, since it can be shown that 6 Killing vectors are present. Because we have maximal symmetry in the 3-dimensional space, we can define the 3D Riemann tensor as:

$${}^{(3)}R_{ijkl} = K(\tilde{g}_{ik}\tilde{g}_{jl} - \tilde{g}_{il}\tilde{g}_{jk}), \quad (1.3)$$

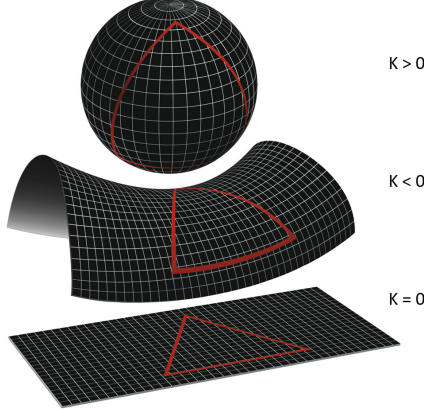


Figure 1.1: Shape of the Universe as a function of  $K$ . If  $K > 0$  the Universe is closed, if  $K < 0$  the Universe is open, while if  $K = 0$  the Universe is flat. [5]

where  $K$  is a constant and the superscript  $(3)$  indicates we are indeed referring to the 3-dimensional spatial case. Moreover, from the 3D Ricci tensor  ${}^{(3)}R_{jl} = {}^{(3)}R_{jkl}^k = {}^{(3)}R_{ijkl}\tilde{g}^{ik}$ , we can write the 3D Ricci scalar  ${}^{(3)}R$  as:

$${}^{(3)}R = {}^{(3)}R_{jkl}g^{jl} = 6K \quad (1.4)$$

The 3 dimensional Ricci scalar is thus a constant. Therefore,  $K$  defines the curvature of the Universe: if  $K > 0$  the curvature of the space is positive and constant (closed Universe), if  $K < 0$  the curvature is negative and constant (open Universe), while if  $K = 0$  the space has zero curvature (flat Universe). In order to normalize  $K$  we can consider the new radial coordinate:

$$d\chi = \frac{dr}{\sqrt{1 - Kr^2}} , \quad (1.5)$$

so that the spatial part of the FLRW metric can be written as:

$$d\sigma^2 = d\chi^2 + f^2(\chi)(d\theta^2 + \sin^2\theta d\phi^2) , \quad (1.6)$$

where  $(\chi, \theta, \phi)$  are the comoving spherical coordinate,  $d\theta^2 + \sin^2\theta d\phi^2 = d\Omega^2$  is the infinitesimal solid angle and  $f(\chi)$  is defined as:

$$f(\chi) = \begin{cases} \sin(\chi) & \text{if } K = +1 \longrightarrow \text{Closed Universe} \\ \chi & \text{if } K = 0 \longrightarrow \text{Flat Universe} \\ \sinh(\chi) & \text{if } K = -1 \longrightarrow \text{Open Universe} \end{cases} \quad (1.7)$$

For a closed Universe, 3 dimensional slices are spheres, for a flat Universe 3D slices are planes, while for an open Universe 3D slices are hyperboloids. This can be seen in Fig. 1.1. In principle, our Universe is compatible with any of these possibilities; however, observations points to a nearly flat Universe [1]. The full expression for the Friedmann-Lemaître-Robertson-Walker metric then is [4]:

$$ds^2 = -(dt)^2 + a^2(t)[d\chi^2 + f^2(\chi)(d\theta^2 + \sin^2\theta d\phi^2)]. \quad (1.8)$$

The comoving distance  $\chi$  between two points is linked to their physical proper distance  $r$  through the scale factor  $a(t)$  as:

$$r = a(t)\chi. \quad (1.9)$$

## 1.2 Einstein Field Equations

Once the metric is specified, the dynamics of the Universe is determined by the Hilbert-Einstein action (which accounts for gravity) and the matter one (which is associated to all the other components, such as scalar fields, fermions, bosons, etc.). We can write the Hilbert-Einstein action

as [4]:

$$S_{HE} \equiv \int d^4x \sqrt{-g} \frac{R}{16\pi G}, \quad (1.10)$$

where  $g$  is the metric trace and  $G$  is the gravitational constant, whose value can be found in the Physical constants section. The matter action can be expressed as [4]:

$$S_M = \int d^4x \sqrt{-g} \mathcal{L}_M, \quad (1.11)$$

where  $\mathcal{L}_M$  is the Lagrangian of all the components under consideration. From the variation with respect to the metric of the total action  $S_{TOT} = S_{HE} + S_M$  it is possible to find the famous Einstein field equations [4]:

$$R_{\mu\nu} - \frac{1}{2}Rg_{\mu\nu} = 8\pi GT_{\mu\nu}, \quad (1.12)$$

where  $T_{\mu\nu}$  is the so-called stress-energy tensor or energy-momentum tensor. In particular, by computing the variation of the Hilbert-Einstein action  $\delta S_{HE}/\delta g_{\mu\nu}$ , it is possible to recover the left-hand side of Eq. 1.12, while from the variation of the matter action  $\delta S_M/\delta g_{\mu\nu}$ , it is possible to find the stress-energy tensor  $T_{\mu\nu}$ . However, to study the action, every particle field should be defined developing a very detailed theory. Alternatively, it is possible to focus on the global properties of the tensor itself: the possibility we are going to analyze is that the correct source of the cosmological background solution, i.e. the average geometry of the spacetime, is a perfect fluid.

A perfect fluid can be completely specified by two quantities: the rest-frame energy density  $\rho$ , and an isotropic rest-frame pressure  $p$ , that specifies the pressure in every direction. The energy-momentum tensor of a perfect fluid takes the following form [4]:

$$T_{\mu\nu} = (p + \rho)u_\mu u_\nu + pg_{\mu\nu}, \quad (1.13)$$

where  $u^\mu$  is the 4-velocity of the fluid such as  $u^\mu u_\mu = -1$ . In its rest frame, where  $u^\mu = (1, 0, 0, 0)$  the stress-energy tensor can be written as:

$$T_{\mu\nu} = \begin{bmatrix} \rho & 0 & 0 & 0 \\ 0 & p & 0 & 0 \\ 0 & 0 & p & 0 \\ 0 & 0 & 0 & p \end{bmatrix} \quad (1.14)$$

We can see that it is diagonal, due to the isotropy requirement. The energy-momentum tensor has the important property of being conserved. This can be expressed by the energy-momentum conservation equations [4]:

$$\nabla_\mu T^{\mu\nu} = 0, \quad (1.15)$$

where  $\nabla_\mu$  denotes the covariant derivative, defined as:

$$\nabla_\mu T^{\mu\nu} = \partial_\mu T^{\mu\nu} + \Gamma_{\mu\lambda}^\mu T^{\lambda\nu} + \Gamma_{\mu\lambda}^\nu T^{\mu\lambda}. \quad (1.16)$$

In turn,  $\partial_\mu$  is the usual partial derivative, while  $\Gamma_{\mu\nu}^\alpha$  are the Christoffel symbols, defined as:

$$\Gamma_{\mu\nu}^\alpha \equiv \frac{1}{2}g^{\alpha\lambda}(g_{\lambda\mu,\nu} + g_{\lambda\nu,\mu} - g_{\mu\nu,\lambda}) \quad (1.17)$$

### 1.3 The evolution of the scale factor

In order to completely characterize the equations governing the dynamics of the Universe, we still need to describe the evolution of the scale factor  $a(t)$ . This can be done by computing explicitly the temporal (00) and spatial ( $ij$ ) components of the Einstein equations (Eq. 1.12) [4]:

$$\begin{cases} R_{00} - \frac{1}{2}R = 8\pi GT_{00} & \rightarrow H^2 \equiv \left(\frac{\dot{a}}{a}\right)^2 = \frac{8\pi G}{3}\rho - \frac{K}{a^2} \\ R_{ij} - \frac{1}{2}R = 8\pi GT_{ij} & \rightarrow \frac{\ddot{a}}{a} = -\frac{4\pi G}{3}(3p + \rho) \end{cases}, \quad (1.18)$$

where the dot indicates the derivative with respect to the cosmic time  $t$  and  $H = H(t)$  is the Hubble parameter, defined as:

$$H(t) = \frac{\dot{a}(t)}{a(t)} \quad (1.19)$$

As we have already seen in Subsection 1.1.1,  $a(t)$  is called the scale factor and it describes the expansion rate of the Universe; its local value is  $a(t=0) = a_0 = 1$ . Similarly,  $H(t=0) = H_0 \simeq 67.66 \text{ km s}^{-1} \text{ Mpc}^{-1}$  (as estimated by *Planck 2018* [1]), is the local Hubble rate, also called the Hubble constant.

These two equations are the so-called Friedmann equations. Since the first Friedmann equation contains only first order time-derivatives of the scale factor, it is not a dynamical equation, but only a constraint that has to be satisfied at all times; it is called the energy constraint. On the other hand, the second Friedmann equation contains second order derivatives of the scale factor, and thus it is a dynamical equation. Moreover, by setting  $\nu = 0$  in Eq. 1.15, we obtain the continuity equation:

$$\dot{\rho} + 3H(p + \rho) = 0 \quad (1.20)$$

With some calculation, it can be shown that the system of equations composed by Eq. 1.18 and Eq. 1.20 is redundant: only two of the three equations are independent. Indeed, we can think the dynamical equation as the consequence of the continuity equation and the energy constraint. Therefore, we are left with the following system [4]:

$$\begin{cases} \left(\frac{\dot{a}}{a}\right)^2 = \frac{8\pi G}{3}\rho - \frac{K}{a^2} \\ \dot{\rho} + 3H(p + \rho) = 0 \end{cases} \quad (1.21)$$

To close the previous system, we need to introduce another important relation, the equation of state. The equation of state relates the pressure and the energy density in the following way:

$$p = w\rho. \quad (1.22)$$

The parameter  $w$  depends on the fluid considered:

$$w = \begin{cases} 0 & \text{for (non-relativistic) matter} \\ 1/3 & \text{for radiation} \\ -1 & \text{for a cosmological constant} \end{cases}. \quad (1.23)$$

By substituting Eq. 1.22 into the system in Eq. 1.21, we can finally find that:

$$\begin{cases} \left(\frac{\dot{a}}{a}\right)^2 = \frac{8\pi G}{3}\rho - \frac{K}{a^2} \\ \dot{\rho} + 3H\rho(1+w) = 0 \end{cases}, \quad (1.24)$$

We can start by taking the second equation of the previous system and integrating it, so we can find that:

$$\rho(t) = \rho(t_*) \left( \frac{a(t)}{a(t_*)} \right)^{-3(1+w)} \quad (1.25)$$

where  $t_*$  is a freely chosen time. Therefore, we can see the different behaviours of the energy density depending on the type of fluid considered:

$$\rho(t) \propto \begin{cases} a(t)^{-3} & \text{for (non-relativistic) matter} \\ a(t)^{-4} & \text{for radiation} \\ \text{constant} & \text{for a cosmological constant} \end{cases}, \quad (1.26)$$

This is intuitive if we consider how energy gets diluted as the Universe expands: for matter, since the number of particles remains the same in a given volume, the energy density scales as the inverse

of a volume, so as  $a^{-3}$ ; for radiation the reasoning is nearly the same, but since also the wavelength gets diluted by expansion (for more details, see Sec. 1.5), the overall scaling is  $a^{-4}$ ; instead, the value of a cosmological constant remains constant by definition, and thus also its value of energy density remains unchanged. [4].

If we consider a flat Universe ( $K = 0$ ), by inserting Eq. 1.25 in the first equation of the system 1.24 and integrating it, we can finally find an expression for the evolution of the scale factor, which results to be:

$$a(t) = \begin{cases} a_* \left( \frac{t}{t_*} \right)^{\frac{2}{3(1+w)}} & \text{if } w \neq -1 \\ a_* e^{H(t-t_*)} & \text{if } w = -1 \end{cases}. \quad (1.27)$$

## 1.4 A multifluid model

To conclude the discussion, we want now to describe all the components of the Universe in the  $\Lambda$ CDM model. To do so, we define the so-called critical density  $\rho_c(t)$  as the density needed to the Universe to be flat ( $K = 0$ ). If we look at the first Friedmann equation in the system 1.18, we can thus write:

$$\rho_c(t) = \frac{3H^2(t)}{8\pi G} \quad (1.28)$$

It is useful to define the total density parameter  $\Omega_{tot}(t)$  as the ratio between the observed total energy density  $\rho_{tot}(t)$  and the critical one  $\rho_c(t)$ :

$$\Omega_{tot}(t) = \frac{\rho_{tot}(t)}{\rho_c(t)}. \quad (1.29)$$

Then, we can make use of this quantity to rewrite the first Friedmann equation (Eq. 1.18) as [4]:

$$\Omega_{tot}(t) - 1 = \frac{K}{a^2 H^2} \quad (1.30)$$

Therefore, we can see that:

- If  $\rho_{tot}(t) = \rho_c(t) \implies \Omega_{tot}(t) = 1 \implies K = 0$ : the Universe is flat.
- If  $\rho_{tot}(t) < \rho_c(t) \implies \Omega_{tot}(t) < 1 \implies K < 0$ : the Universe is open.
- If  $\rho_{tot}(t) > \rho_c(t) \implies \Omega_{tot}(t) > 1 \implies K > 0$ : the Universe is closed.

Finally, we can consider the total energy density today, so with  $t = t_0$ . With this choice, we can rewrite the critical density today as:

$$\rho_c(t_0) = \frac{3H^2(t_0)}{8\pi G} \longrightarrow \rho_{c,0} = \frac{3H_0^2}{8\pi G}, \quad (1.31)$$

and the total density parameter today as:

$$\Omega_{tot}(t_0) = \frac{\rho_{tot}(t_0)}{\rho_c(t_0)} \longrightarrow \Omega_{tot,0} = \frac{\rho_{tot,0}}{\rho_{c,0}}. \quad (1.32)$$

Then, we can decompose  $\Omega_{tot,0}$  as the sum of all the species present in the Universe:

$$\Omega_{tot,0} = \Omega_\Lambda + \Omega_M + \Omega_R = \Omega_\Lambda + \Omega_B + \Omega_{DM} + \Omega_R, \quad (1.33)$$

where

$$\Omega_i = \frac{\rho_i}{\rho_{c,0}}, \quad (1.34)$$

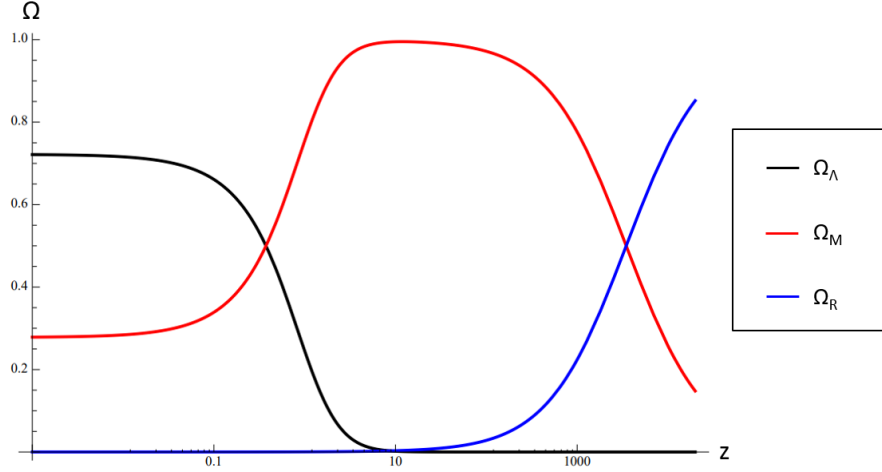


Figure 1.2: Evolution of the various density parameters  $\Omega_\Lambda, \Omega_M, \Omega_R$  as a function of time. The time dependence is described by the redshift. [6]

and the subscript  $\Lambda$  stands for the cosmological constant,  $M$  for matter,  $R$  for radiation,  $B$  for baryons and  $DM$  for dark matter. All these quantities have been estimated by the *Planck 2018* mission [1] and their numerical values can be found in the Physical constants section. Since it might be useful to the reader, we report also here their values:

- Radiation density:  $\Omega_R = \frac{\rho_R}{\rho_{c,0}} = 5.39 \cdot 10^{-5}$
- Barion density:  $\Omega_B = \frac{\rho_B}{\rho_{c,0}} = 0.05$
- Dark Matter density:  $\Omega_{DM} = \frac{\rho_{DM}}{\rho_{c,0}} = 0.26$
- Matter density:  $\Omega_M = \frac{\rho_m}{\rho_{c,0}} = \Omega_{DM} + \Omega_B = 0.31$
- Cosmological constant density:  $\Omega_\Lambda = \frac{\rho_\Lambda}{\rho_{c,0}} = 0.69$

Even though observations seem to indicate that  $\Omega_{tot,0} \sim 1$  (flat Universe), the other two possibilities are not ruled out (open or closed Universe with very large curvature).

Of course, the values of the various contributions to the total density parameter at a given time  $t$  depend in turn on time (Eq. 1.25). This can be also seen explicitly in Fig. 1.2.

## 1.5 Redshift

As we saw qualitatively in the previous section, wavelengths in an expanding Universe get diluted. More in detail, when a light source receding from us (e.g. a distant galaxy) is considered, the wavelength of its light is stretched proportionally to the rate of expansion of the Universe. This can be described by a quantity called redshift, defined as:

$$z = \frac{\lambda_{obs} - \lambda_{em}}{\lambda_{em}} \quad (1.35)$$

where  $\lambda_{obs}$  is the wavelength of the observed radiation and  $\lambda_{em}$  is the wavelength of the emitted one. We can also relate the redshift  $z$  to the scale factor in a FLRW Universe through the following relation:

$$1 + z = \frac{a(t_{obs})}{a(t_{em})} \quad (1.36)$$

where  $a(t_{obs})$  is the scale factor at the time of observation and  $a(t_{em})$  is the scale factor at the time of radiation emission. We can note that if the scale factor is a monotonic function, then the

redshift can be considered as a temporal variable. Local, near-Earth sources have  $z = 0$ , while sources ideally located at the Big-Bang would have  $z = \infty$ .

It is possible to show that, by using the density parameters of the previous section and the redshift, the Hubble parameter can be expressed as:

$$H(z) = H_0 \sqrt{\Omega_M(1+z)^3 + \Omega_R(1+z)^4 + \Omega_\Lambda} \quad (1.37)$$

## 1.6 Brief thermal history of the Universe

The Hot Big Bang model explains how the Universe evolved from an initial state of high density and temperature (“Big Bang singularity”) to the cooling expanding Universe we observe today [4]. The description of the thermal history of the Universe can start at  $t = 10^{-43}$ s after the Big Bang, when the energy reached the so-called Planck scale  $c^2 m_{pl} = 10^{19}$  GeV, where  $m_{pl}$  is the Planck mass. To describe the Universe before that moment, a more refined theory of gravity (i.e. quantum gravity) is needed.

After this first moment, when the energy reached the value of  $E \simeq 10^{16}$  GeV, inflation occurred. This is a period of accelerated expansion, in which the Universe expanded up to cosmological scales [4]. After that, the QCD (Quantum Chromodynamics) phase transition occurred ( $t \simeq 20\ \mu\text{s}$ ,  $E \simeq 150$  MeV) and bounded quark states were created. Approximately  $t \simeq 3$  min after the Big Bang, the first nuclei began to form, in the process named Big Bang Nucleosynthesis (BBN) [4]. After nucleosynthesis, one last step is needed to describe the thermal history of the Universe: electrons and protons combined to form hydrogen atoms. Since then, the Compton scattering ( $e^- + \gamma \rightarrow e^- + \gamma$ ) that previously placed photons and baryons in thermal equilibrium, became no longer effective and radiation could decouple from matter. From that moment on ( $z_{rec} \simeq 1100$  [4]), photons became free to stream across the Universe: today, we can observe them thanks to the Cosmic Microwave Background (CMB). The CMB has an almost perfect black-body spectrum, with an average temperature of 2.725 K; on top of that, anisotropies consisting of small ( $\Delta T/T \sim 10^{-5}$ ) temperature fluctuations arise.

As we have seen in the previous section, across cosmic time the energy density of the different species evolved differently. In particular, by equating the first two lines of Eq. 1.26, we can find that there was a time in which the matter density and the radiation density were the same. This moment is known as the matter-radiation equality, and its redshift corresponds to  $z_{eq} \sim 3400$  (when the red and blue lines in Fig. 1.2 cross). Before that moment, the Universe was dominated by radiation (radiation-dominated epoch), while after that matter dominated the Universe (matter-dominated epoch). Considering also the presence of a cosmological constant, we can see that there was a moment in which the energy density of this terms began to dominate over the matter density ( $z \simeq 0.3$ , when the red and black lines in Fig. 1.2 cross).



## Chapter 2

# Primordial Black Holes

### 2.1 Introduction

A black hole (BH) is a region of space-time where gravity is so strong that nothing -nor particles nor electromagnetic radiation- can escape from it. Objects whose gravitational fields are too strong for light to escape were first considered in the 18th century by John Michell and Pierre-Simon Laplace. The first modern solution of General Relativity (GR) that would characterize a black hole was found by Karl Schwarzschild in 1916 [7], although its interpretation as a region of space from which nothing can escape was first published by David Finkelstein in 1958 [8]. Indeed, general relativity predicts that a region of mass  $M$  forms a black hole if it falls within its Schwarzschild radius, defined as

$$R_S \equiv \frac{2GM}{c^2} \quad (2.1)$$

where  $c$  is the speed of light, whose value can be found in the Physical constants section.

Essentially, there are three types of black holes, depending on the formation mechanism: stellar black holes, Primordial Black Holes (PBHs) and supermassive black holes (SMBHs). There is now overwhelming evidence for stellar and supermassive black holes, while no conclusive confirmation for PBHs has been found.

A stellar black hole originates when a massive star ( $M \gtrsim 25M_\odot$ , with  $M_\odot$  being the mass of the Sun, whose numerical value is also reported in the Physical constants section) ends its evolutionary phase and eventually collapses, losing its external layers and leaving a central compact object as a remnant [9]. The mass range of the remnant goes from  $\sim 3M_\odot$ , the maximum mass of a neutron star given by the Tolman-Oppenheimer-Volkoff limit [10], to  $\sim O(100)M_\odot$ . The upper limit strongly depends on the evolution processes of a massive star, which are rather uncertain and not clear yet [9].

Primordial Black Holes are very different from stellar BHs: as we are going to see much more in detail in the following sections, the formation of Primordial Black Holes is based on the direct gravitational collapse of a highly overdense region of inhomogeneities in the primordial Universe [11] [12].

Supermassive black holes reside in galactic nuclei, with  $10^6 M_\odot \lesssim M_{SMBH} \lesssim 10^{10} M_\odot$ . These SMBHs are usually assumed to form as a result of dynamical processes after galaxy formation, but it may be hard to explain how they could have formed so early in the standard picture [13]. Therefore, some authors have investigated the possibility that supermassive black holes could be seeded by a massive population of PBHs [14]. Indeed, very massive PBHs ( $10^5 M_\odot$ ) could accrete very efficiently in the early Universe up to masses similar to those of the SMBHs. It is now still debated if SMBHs originate after galaxy formation or if they can be included in the PBHs theory [14] [15].

The history of Primordial Black Holes started in the late sixties, when Zel'dovich and Novikov first showed that a black hole in the early Universe might grow catastrophically by accreting the surrounding radiation. The treatment of such objects was carried on by Hawking some years later, when he proposed the formation of BHs as a consequence of direct gravitational collapse of inhomogeneities in the primordial Universe [16]. This initiated the modern theory of the mechanism of PBHs formation.

## 2.2 The Dark Matter problem

Assuming general relativity is correct and according to the  $\Lambda$ CDM model, there is extensive astronomical and cosmological evidence that the majority ( $\sim 85\%$ ) of the matter in the Universe, about 26% of the entire energy content, is made of non-luminous matter [1]. This type of matter is called cold dark matter (CDM), it is non-baryonic and it does not interact with observable electromagnetic radiation, making it extremely difficult to detect with standard astronomical equipment. All the observational probes we have of dark matter are due to the effects induced by its gravitational potential. Here we describe the most famous ones.

Historically, dark matter was postulated as a consequence of the application of the virial theorem [17]. The virial theorem states that the total kinetic energy of a self-gravitating body due to the motions of its constituent parts ( $K$ ) is related to the gravitational potential energy of the body ( $U$ ) through the following relation:  $2K + U = 0$ . While examining the Coma galaxy cluster in 1933, Zwicky [17] found that the rotational velocities of galaxies inside that cluster were excessive for the cluster to remain compact. The gravitational mass of the cluster as computed from those velocities exceeded the luminous mass: Zwicky named that gravitational anomaly as *Dunkle Materie* (Dark Matter) [17]. Another clue for the existence of dark matter is that also stars in bound systems must obey to the virial theorem [18]. This theorem can be then exploited to measure the mass distribution of a galaxy. However, velocity dispersion estimates of elliptical galaxies do not match the predicted velocity dispersion from the observed mass distribution [18]. Also in this case, one way to resolve the inconsistency is to postulate the existence of dark matter.

The most famous example of the need for the introduction of dark matter was due to discrepancies between the expected spiral galaxy rotation curves and the observed ones [19]. The luminous mass density of a spiral galaxy decreases going from the center to the outskirts, so we would expect that rotation velocities should decrease too. Indeed, the velocity of stars  $v(r)$  at the distance  $r$  from the galactic centre reads:

$$v(r) = \sqrt{\frac{GM(r)}{r}}. \quad (2.2)$$

Instead, the galaxy rotation curve is observed to remain flat as the distance from the center increases. This inconsistency is relieved if a huge quantity of non-luminous matter (i.e., dark matter) is postulated to be present in the outskirts of the spiral galaxy. [19]

Gravitational lensing is a solid prediction of general relativity: massive objects between the observer and a source act as lenses, bending the light of the source itself. More massive the object, more lensing effect there is, and it is possible to estimate the mass of an object by measuring the gravitational distortions produced. It has been observed that the lensing effects overcome those expected only by the luminous mass, suggesting the presence of much more matter than the one detected [20].

The Cosmic Microwave Background is the thermal relic radiation from the early phase of the Universe. We have seen that dark matter, unlike ordinary matter, does not interact with light. However, it does affect the cosmic microwave background due to its gravitational potential. The study of the CMB and its temperature anisotropies can then be used as a tool to understand dark matter. Indeed, a sky map of anisotropies can be decomposed into an angular power spectrum (that captures how much difference there is between the function values at different points as a function of the angular distance between them), which presents various peaks. If the first three peaks can be measured with good precision, the baryon density and the total density of non-relativistic matter (Eq. 1.34) can be determined accurately. Therefore, we can estimate the abundance of dark matter

from the relative heights: a higher proportion of dark matter would enhance the height of the third peak of the power spectrum as compared to the second [4].

Another argument that suggests the presence of DM is connected to structure formation at large scales. In fact, those structures have been generated by the small matter anisotropies which gradually grew in the universe. However, if there were only ordinary matter anisotropies, the presence of radiation during radiation domination would have washed them out. Dark matter provides a solution to this problem, since it is unaffected by radiation [4]. Therefore, its density perturbations can grow to form the structures in the universe.

Together with those presented in this section, there are many other hints that indicate the existence of dark matter. Yet, its nature is one of the most longstanding and puzzling questions in modern physics and to date there is no conclusive answer to that. Many candidates have been proposed to solve this problem. We can divide the DM candidates in six macro-categories:

- Light bosons: QCD axions, axion-like particles, fuzzy dark matter, etc.
- Neutrinos: Standard-model neutrinos, sterile neutrinos, etc.
- Other particles: WIMPs, superfluid, etc.
- Modified Gravity: MOND, emergent gravity, MOG, etc.
- Weak Scale features: Super-symmetry, extra-dimensions, Little-Higgs, etc.
- Macroscopic objects: Primordial Black Holes, MaCHOs, etc.

A full analysis of all of these is beyond the scope of this thesis, which instead focuses on the possibility that (at least part of) dark matter is made by Primordial Black Holes. One important feature of Primordial Black Holes is that, as we will describe in Sec. 2.3, they could have been produced during the radiation-dominated era in the early Universe. This is a crucial difference compared to astrophysical black holes, because ABHs form at late times from the collapse of stars and thus can not provide all the dark matter. Indeed, they form from baryons and they are subject to the well-known big bang nucleosynthesis (BBN) constraint that baryons can have at most 5% of the critical density [1]. On the contrary, since PBHs formed in the radiation-dominated era, they are not subject to this constraint and they should therefore be classed as nonbaryonic; moreover, from a dynamical perspective they behave like any other form of cold dark matter (CDM) [21]. Therefore, Primordial Black Holes are appealing candidates to solve the dark matter problem: even if they do need special initial conditions, they do not require new physics, unlike most of the other candidates.

## 2.3 Formation mechanisms

Primordial Black Holes could have been produced during the radiation-dominated era (see Section 1.6) in the early Universe due to various mechanisms. The most natural mechanism to form Primordial Black Holes can be developed as follows and it is sketched in Fig. 2.1, taken from [22].

In the early Universe after inflation, the background spacetime can be well-described by the spatially-flat Friedmann-Lemaître-Robertson-Walker metric [4]. By recalling what we saw in Subsect. 1.1.1, we can write:

$$ds^2 = -dt^2 + a(t)^2 \delta_{ij} dx^i dx^j. \quad (2.3)$$

where  $\delta_{ij}$  is the Kronecker delta of spatial indices  $i, j$ . This background is characterised by the mean energy density  $\bar{\rho}$ . At first approximation, PBH formation can be studied through spherical collapse of a positive curvature perturbation over the background spacetime. Such perturbation would initially have comoving size larger than the cosmological horizon  $d_H = (aH)^{-1}$ . [16]. Depending on their scales  $\lambda$ , perturbations entered the horizon in different epochs (larger scales entered later).

We saw (Eq. 1.22) that the equation of state that relates the pressure ( $p$ ) of the fluid with its energy density ( $\rho$ ) is given by

$$p = w\rho, \quad (2.4)$$

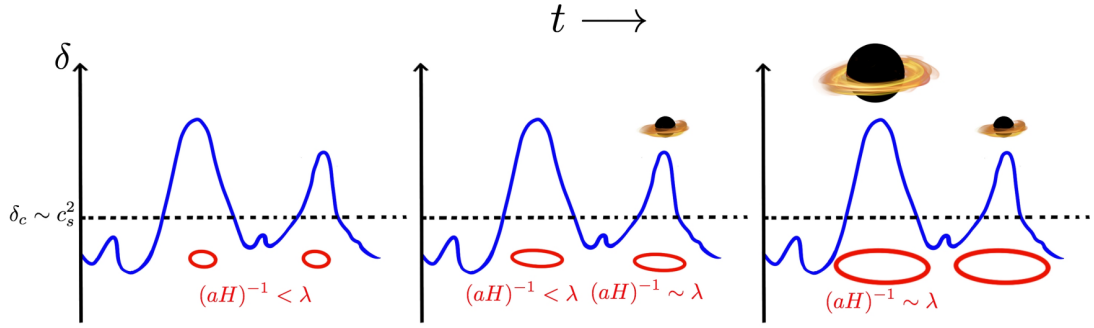


Figure 2.1: Schematic representation of the formation of PBHs from overdensities for three different successive moments. When fluctuations larger than the critical threshold  $\delta_c \sim c_s^2$  enter the horizon the overdense region collapses and a PBH is produced. Note that depending on their scales, perturbations entered the horizon in different epochs. Since larger scales entered later, they lead to more massive PBHs. [22]

where  $w$  is a dimensionless constant. In particular, for the radiation dominated era we are considering for PBH formation,  $w = 1/3$  and radiation pressure can balance gravitational collapse of inhomogeneities up to the Jeans length  $\ell_J$ . This is defined as the critical wavelength below which a small perturbation is unstable and collapses under its own gravity; it is defined by the relation  $\ell_J = c_s/H$ , where  $c_s = 1/\sqrt{3}$  is the sound speed in the radiation dominated era. Therefore, for gravity to overcome pressure, the inhomogeneous region must be larger than the Jeans length. This leads to the requirement that the density contrast  $\delta$ , defined as:

$$\delta = \frac{\delta\rho}{\bar{\rho}} = \frac{\rho - \bar{\rho}}{\bar{\rho}} \quad (2.5)$$

at horizon crossing must exceed a critical value  $\delta_c \approx w = c_s^2$  [23]. If this happens, a PBH forms. The criteria for PBH formation in a matter dominated Universe with  $w = 0$  are somewhat different. In this case, because the pressure is zero, it is possible for PBHs to form well within the horizon [16].

Since the Jeans length at horizon crossing is roughly the size of the horizon itself, at first approximation the mass of the formed PBH can be estimated as the mass included in the horizon at collapse. We can thus estimate the mass of the primordial black hole ( $M_{PBH}$ ) that collapses at  $t_f$  assuming that it forms immediately after a perturbation enters the horizon. Denoting with  $M_H$  the horizon mass at horizon crossing, we can find an estimation of the mass of the PBH as [24]:

$$M_{PBH} \sim M_H = \frac{4\pi}{3} \rho_H R_H^3 = \frac{4\pi}{3} \frac{3H^2}{8\pi G} \left( \frac{c}{H} \right)^3 = \frac{c^3 t_f}{G} = 10^{15} \left( \frac{t_f}{10^{-23} \text{ s}} \right) \text{ g}, \quad (2.6)$$

where we assumed a spatially flat Friedmann–Lemaître–Robertson–Walker metric and we used the fact that  $H \propto 1/(2t)$  during the radiation domination era. In the equation,  $R_H = c/H$  is the Hubble radius and  $\rho_H = 3H^2/8\pi G$  is the horizon energy density.

From Eq. 2.6 we can see that, depending on their formation time, PBHs can have a wide range of masses: those formed at Planck time ( $10^{-43}$  s) would have the Planck mass ( $10^{-5}$  g), those formed at the QCD phase transition at  $t \sim 10^{-6}$  s would have mass of order one solar mass, while those formed at 1 s would be as large as  $10^5 M_\odot$ , comparable to the mass of the black holes thought to reside in galactic nuclei. Indeed, already  $\sim 10^3 - 10^4 M_\odot$  PBHs could accrete and thus form what we see now as SMBHs [25].

### 2.3.1 Other mechanisms

There are other possible scenarios for PBH formation; in this subsection we will simply describe them, since their specific analysis is beyond the scope of this thesis.

Cosmic strings are one-dimensional topological defects which may form during phase transitions in the very early Universe [26]. In the cosmic string scenario, one expects long strings to self-intersect and form cosmic loops [21]. If this is achieved, there is a non-vanishing probability that this string will be in a configuration where all its dimensions are less than its Schwarzschild radius. If this is achieved too, then it collapses and a PBH with mass roughly equal to the horizon mass is expected to form. Cosmic string loops can collapse to form PBHs at any point during radiation domination, therefore the resulting PBHs should have an extended mass function [23]. Both the previously mentioned probability and the number of PBHs formed depend on the mass per unit length of the strings, which is related to the symmetry breaking scale.

In the Universe, when a symmetry is spontaneously broken, bubbles of broken symmetry might arise. These bubbles of the new phase would expand into the old phase until they collide with other expanding bubbles of the new phase [27]. In the collision of two bubbles, Primordial Black Holes could form. However, the bubble formation rate per Hubble volume must be finely tuned in order to produce PBHs [21]: if the bubble formation rate is much larger than the Hubble one, there is no time to form black holes; on the opposite case, if the formation rate is much less than the Hubble rate, the bubbles are very rare and never collide. Therefore, forming the right abundance of PBHs requires fine tuning of the bubble collision rate.

A domain wall is a type of topological soliton that occurs whenever a discrete symmetry is spontaneously broken [15]. The collapse of sufficiently large closed domain walls produced at a 2<sup>nd</sup>-order phase transition in the vacuum state of a scalar field, such as might be associated with inflation, could lead to Primordial Black Holes formation. These PBHs would have a small mass for a thermal phase transition with the usual equilibrium conditions. However, they could be much larger if one invoked a non-equilibrium scenario [15].

## 2.4 Initial conditions

The initial set of parameters that characterize a population of Primordial Black Holes will ultimately depend on the precise prescriptions for that population, such as the formation mechanisms and the mass function. However, many recent works ([28], [29], [29], [30]) seem to agree on the expected initial clustering and spin distribution of a generic PBH population.

Indeed, Primordial Black Holes are thought to be spatially Poisson distributed at formation, and therefore they are not clustered, independently on the mass functions. The subsequent evolution of the clustering depends upon the merging and accretion of the PBHs, and it might be fully captured only by real-time numerical simulations [28]. However, some authors point out that PBHs could be clustered into subhalos if they are part of a larger-scale overdense region and this conclusion is supported by the study on the clustering dynamics of PBHs in N-body simulations [29] [31] [32].

Moreover, Primordial Black Holes at formation should not have large spins, with the dimensionless spin parameter  $a_{PBH}$  being of the percentage order (i.e.  $a_{PBH} \sim 0.01$ ) [30]. The late evolution of this parameter depends on the accretion history of the primordial black hole. In particular, accretion is important for PBH with mass  $M_{PBH} > 10M_\odot$  and Primordial Black Holes with mass higher than that could acquire spin due to accretion [30]. On the contrary, spins should remain small for lighter PBHs, since accretion is negligible.

## 2.5 Constraints on abundance

It is customary to describe primordial black holes' abundance in terms of the ratio between the current PBH mass density  $\Omega_{PBH}$  and that of the CDM density  $\Omega_{CDM}$  (previously denoted as  $\Omega_{DM}$  in Eq. 1.34):

$$f_{PBH} \equiv \frac{\Omega_{PBH}}{\Omega_{CDM}}, \quad (2.7)$$

where if Primordial Black Holes comprise the totality of DM then  $f_{PBH} = 1$ . Since this parameter has been defined locally, it is constant in redshift and can be used as an indication of the abundance of PBHs irrespective of time. Moreover, once we specify a mass function  $\Psi(M)$  for Primordial Black Holes, the following must be true:

$$f_{PBH} \equiv \frac{\Omega_{PBH}}{\Omega_{CDM}} = \int_{M_{PBH}^{min}}^{M_{PBH}^{max}} \Psi(M) dM. \quad (2.8)$$

As firstly realised by Hawking [33], black holes radiate thermally because of relativistic quantum effects. Under this process, the so called Hawking radiation, black holes evaporate on a timescale  $\tau_{BH}$  that depends on their mass in the following way:

$$\tau_{BH} \sim 10^{10} \left( \frac{M_{PBH}}{10^{15} \text{ g}} \right)^3 \text{ Gyrs} \quad (2.9)$$

From this relation we can thus see that, while for stellar black holes  $\tau_{BH}$  is longer than the age of the Universe, PBHs with masses of  $M_{PBH} \sim 5 \times 10^{14} \text{ g}$  will be evaporating today.

To study Primordial Black Holes' abundance and features we must specify the expected PBH mass function  $\Psi(M)$ . In principle, Primordial Black Holes could have two types of mass functions: either it is monochromatic, so all the PBHs would form with nearly the same mass, or it is extended, and their masses spread in a wide range. Most of the PBH dark-matter proposals assume that the mass function of the black holes is very narrow (i.e. nearly monochromatic, with width  $\Delta M \ll M$ ). Even if this is the simplest approach, this is also the most unrealistic case and in most scenarios one would expect the mass function to be extended [34]. In the context of the dark matter problem, this is a double-edged sword. On the one hand, it means that the total PBH density may suffice to explain the dark matter, even if the density in any particular mass band is small and within the observational bounds. On the other hand, even if PBHs can provide all the dark matter at some mass scale, the extended mass function may still violate the constraints at some other scale [21].

Often in Primordial Black Holes' literature (e.g. [35], [36], [37]) a log-normal distribution is used, since it is very flexible. Such a distribution, characterized by the central mass  $\mu$  and width  $\sigma$  (which thus determines if the mass function is monochromatic or extended), has the following form:

$$\Psi(m) = \frac{1}{m} \frac{1}{\ln(10)\sqrt{2\pi\sigma^2}} \exp\left(-\frac{\log_{10}(\frac{m}{\mu})^2}{2\sigma^2}\right) \quad (2.10)$$

where  $m$  is the mass of the primordial black hole. In the analysis we will develop in Chapter 4 and Chapter 5, we will as well adopt a log-normal distribution.

Thus, we will now analyze the various constraints for PBHs which are too large to have evaporated completely by now (namely, with masses  $M_{PBH} \geq 10^{-18} M_\odot$ ). Indeed, even if Primordial Black Holes have not been detected yet, we can constrain their abundance on the different mass ranges by combining different probes and based on non-detection of some features in the Universe. All these constraints have been recently summarized in [26]; we show them in Fig. 2.3 and will be now analyzed in detail. We stress that the constraints have been derived for quasi-monochromatic mass spectra, and therefore are valid only for mass functions narrow enough; for very extended mass functions they are not valid and, in case, one should recompute them with the extended mass function prescription.

### 2.5.1 Evaporation constraints

We can define the temperature  $T$  of a Primordial Black Hole as [38]:

$$k_B T \simeq 1.06 \left( \frac{M_{PBH}}{10^{13} \text{g}} \right)^{-1} \text{GeV} \quad (2.11)$$

where  $M_{PBH}$  is the mass of the PBH and  $k_B$  is the Boltzmann constant, whose value can be found in the Physical constants section. A black hole emits all particles whose rest masses are less than or of the order of its temperature [38]. Photons and massless neutrinos are emitted in substantial numbers at all temperatures. Therefore, if the black hole temperature exceeds the QCD confinement scale ( $T = 160 \text{ Mev}$ , which corresponds to  $M_{PBH} \simeq 0.4 M_*$ ), quark and gluon jets are emitted directly. In turn, the quark and gluon jets fragment and decay producing astrophysically stable particles: photons, neutrinos, electrons, protons and their anti-particles [23].

All these particles impact and distort other radiation fields in the Universe. By measuring those fields we can place constraints on the particles emitted and thus on the abundance of Primordial Black Holes. For example, the galactic and extragalactic  $\gamma$ -ray background, the positron data from Voyager 1 and the 511 keV annihilation line radiation from the Galactic centre have been exploited to constrain the abundance of PBH with masses  $M_{PBH} < 10^{-16} M_\odot$  ([39], [40], [41]). The sum of these constraints is reported in orange in Figure 2.3.

### 2.5.2 Lensing constraints

Lensing constraints exploit gravitational lensing, which is a very powerful technique, since it does not depend on all the uncertainties that characterize the interactions between the primordial black holes and the surrounding matter. The basic geometry of gravitational lensing is depicted in Fig. 2.2: a mass between the observer and a source deflects the light from the source. In general this translates in two lensed images seen by the observer, while if the source and the object are on the same line then the image on the lens plane becomes the so-called Einstein Ring [42]. If the angular separation of the two images is smaller than the angular resolution of a given experiment, then such experiment would detect the superposition of the two images, which is brighter than the original source. Therefore, if a compact object (CO) is between a star and the Earth, the experiment would observe a magnification of that star. In this way, it is possible to detect a PBH if it transits between the Earth and a star; depending on the PBH abundance, the rate of lensing events should be altered [16].

For  $10^{17} \text{g} < M_{CO} < 10^{20} \text{g}$  the image separation is of order femto ( $10^{-15}$ ) arc-seconds. Microlensing ( $10^{-6}$  arc-seconds) occurs when a CO with mass in the range  $10^{24} \text{g} < M_{CO} < 10^{34} \text{g}$  crosses the line of sight to a star or a quasar. Massive compact objects with  $10^{39} \text{g} < M_{CO} < 10^{41} \text{g}$  can millilens ( $10^{-3}$  arc-seconds) radio sources. Many experiments, such as the MACHO project [43], EROS (Experience pour la Recherche d'Objets Sombres [44]), and OGLE (Optical Gravitational Lensing Experiment survey [45]), have been exploited to detect/constrain Primordial Black Holes. The sum of all these constraints is reported in blue in Figure 2.3.

### 2.5.3 Gravitational Waves constraints

As we are going to analyze in this Master thesis, Primordial Black Holes, if they exist, are expected to interact with each other and to generate a Stochastic Gravitational Wave Background (SGWB, for more details, see Sec. 3.4). Moreover, if a binary of PBHs will be coalescing at the present epoch we could be able to detect Gravitational Waves (GW) from that event. First of all, the non-observation of a gravitational wave background gives constraints on the fraction of dark matter in PBHs [21] of masses  $0.5 M_\odot < M_{PBH} < 30 M_\odot$ , depending on the GW frequency observed. Besides, the current coalescing rate from LIGO-Virgo [46] can constrain directly PBHs abundance in the  $\sim 10 - 100 M_\odot$  mass range. However, as we will discuss more in detail in Chapter 4, constraints from the gravitational wave events detected by experiments depend quite strongly on whether the binaries formed in the early Universe or after galaxy formation and therefore they are rather uncertain.

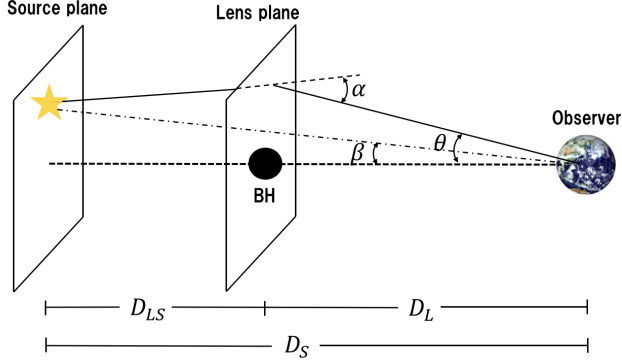


Figure 2.2: Schematic representation of gravitational lensing: a compact object (BH) would deflect the light ray coming from a distant star. [16]

Stochastic gravitational waves can also arise from the primordial density perturbations seeding the PBHs [16]. The limits on their amplitude constrain the amplitude of the density perturbations and hence the abundance of PBHs formed. Constraints related with pulsar timing array place a tight limit on the present day density parameter of PBHs in the mass range  $10^{35} \text{ g} < M_{\text{PBH}} < 10^{37} \text{ g}$  [23].

We can see the sum of all these constraints reported in violet in Figure 2.3.

#### 2.5.4 Accretion constraints

Due to gravitational interaction, Primordial Black Holes can accrete surrounding gas. As the gas falls towards the black hole, it gets compressed, increasing its density and temperature and eventually becoming fully ionized. Therefore, intense radiation beams of ionized gas can be emanated outside the primordial black hole.

However, this is important only for massive ( $M_{\text{PBH}} \gtrsim 1 M_{\odot}$ ) PBHs, since for lighter black holes the effect is completely negligible [16]. We can think of two distinct moments when PBHs can accrete, that in turn give rise to two different types of constraints: those related to accretion effects on the CMB that arise in the early Universe and those associated to the electromagnetic waves from the accreted matter from the present PBHs.

In the first case, the radiation ionizes or heats the gas filling the Universe, modifying the spectrum of the CMB photons from the Planckian distribution, the decoupling time of the CMB photons, and the ionization history [16]. In this way Primordial Black Holes could leave imprints of non-standard features in the CMB observables. The non-detection of such features can be thus translated into constraints on PBHs abundance.

The very same situation (but with different imprints) can occur in the present Universe for PBHs in dense environments. It was found that, by comparing observational data with the theoretical predictions of electromagnetic waves from accreting PBHs, both x-ray and radio observations result in a meaningful constraint  $f_{\text{PBH}} < 1$  [16]. We stress that for this type of constraints much physics is involved, often with strong assumptions and empirical rules, and therefore they are very model-dependent [16]. Indeed, different astrophysical assumptions could lead very different constraints. This can be seen in Figure 2.4, taken from [47], where PBHs in the mass window  $10^0 M_{\odot} \lesssim M_{\text{PBH}} \lesssim 10^2 M_{\odot}$  could still provide a non negligible fraction of dark matter.

The sum of all the constraints from early and present-universe accretion are reported in red in Figure 2.3.

#### 2.5.5 Dynamical constraints

To a certain degree, every astrophysical system is affected gravitationally by Primordial Black Holes. Therefore, we can exploit this fact to constrain PBH by making comparison with observa-

tional data. As we are going to see now, many astrophysical systems can be studied to constrain PBHs in the mass window  $M_{PBH} > 10 M_\odot$ .

For example, white dwarfs (WD) can be used as a probe for PBHs abundance [16]. Indeed, the passage of a PBH through a white dwarf would ignite the thermonuclear runaway and make the white dwarf explode. This argument can be used only for a certain PBHs mass range: very light PBHs do not give enough energy to WDs to make them explode, while massive PBHs do not encounter often white dwarfs due to their rareness. From the number of white dwarfs observed in our Galaxy, we can constrain the PBH abundance.

Similar arguments can be exploited for encounters with neutron stars (NS): if a PBH approaches a NS, these two can bound in a binary system. Then, the PBH would transfer its kinetic energy to the neutron star and eventually it will be trapped inside the NS itself. When this happens, the PBH quickly accretes the matter from the neutron star, making the NS explode. Thus, neutron stars must not be exposed to frequent encounters with the PBHs, from which a certain upper limit on PBH abundance can be derived. [16].

Wide halo binaries are binaries of stars in the Milky Way halo separated by wide separation and therefore they have weak binding energy. Thus, they are particularly subject to disruption if a PBH passes near to them [16]. Observations of such binaries can then put limits on PBHs abundance. Similarly, this reasoning can be used also for globular clusters, with the only difference that here many star are involved. [16]

We can constrain PBHs also by means of ultra-faint dwarf galaxies (UFDGs): if PBHs that reside inside those galaxies are more massive than stars, they could transfer kinetic energy to the stars, making them move faster and spread wider, until UFDGs are disrupted [16]. Observations of this type of galaxies constrain then Primordial Black Holes.

In addition, if massive PBHs are present in the galactic halo and can be found near the galactic center, they would receive strong dynamical friction from stars and spiral in to the center. If this infall time scale is shorter than the age of the Universe, accumulation of PBHs continues in the central region, leading to a highly concentrated region near the galactic center [16]. Since the mass of the galactic center can be calculated, this translates in constraints to PBHs.

We can see the sum of all the dynamical constraints reported in green in Figure 2.3.

### 2.5.6 Summary of constraints

The constraints on the fraction of dark matter in the form of Primordial Black Holes are summarized in Figure 2.3, which was taken from [26]. In the figure, evaporation constraints are marked in orange, lensing constraints are marked in blue, gravitational wave constraints are marked in violet, accretion constraints are marked in red and dynamical constraints are marked in green. Primordial Black Holes of a given mass  $M_{PBH}$  must lie below the various lines provided by the observations: this corresponds to constrain the maximum fraction  $f_{PBH}$  allowed for every mass. All the limits assume that the PBHs have a monochromatic mass function and cluster in the Galactic halo in the same way as other forms of cold dark matter. We can see from the figure that three windows are currently permitting  $f_{PBH} \sim 0.1 - 1$ , i.e. the mass windows for which Primordial Black Holes could provide a non-negligible source of dark matter:

- The asteroid mass range ( $10^{-16} M_\odot - 10^{-11} M_\odot$ )
- The sublunar mass range ( $10^{-7} M_\odot - 10^{-4} M_\odot$ )
- The intermediate mass range ( $10^{-2} M_\odot - 100 M_\odot$ )

The existence of PBHs in other mass ranges are still allowed for smaller values of  $f_{PBH}$  and for extended mass distributions.

In the analysis we will develop in 5, we will consider 5 populations of PBHs: 3 monochromatic ( $10^{-5} M_\odot, 10^{-1} M_\odot, 30 M_\odot$ ) and 2 extended (log-normal and power-law distributions).

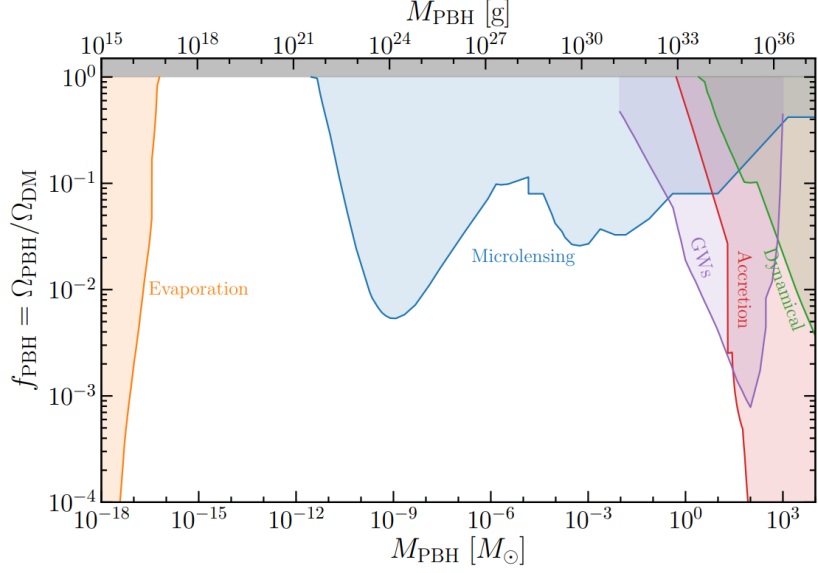


Figure 2.3: Current constraints from different probes on primordial black hole abundance as function of their masses. As labeled in the figure, we can see the evaporation constraints in orange, the microlensing constraints in blue, the gravitational waves constraints in violet, the accretion constraints in red and the dynamical constraints in green. The white region of the figure indicates where, assuming a monochromatic mass distribution, Primordial Black Holes of a given mass could exist and with which abundance. We can see that there is still an open window in which Primordial Black Holes could be the totality of dark matter ( $10^{-16} M_\odot \lesssim M_{PBH} \lesssim 10^{-11} M_\odot$ ), and other two ( $10^{-7} M_\odot \lesssim M_{PBH} \lesssim 10^{-4} M_\odot$  and  $10^{-2} M_\odot \lesssim M_{PBH} \lesssim 10^0 M_\odot$ ) in which they could represent a non-negligible fraction of it. [26]

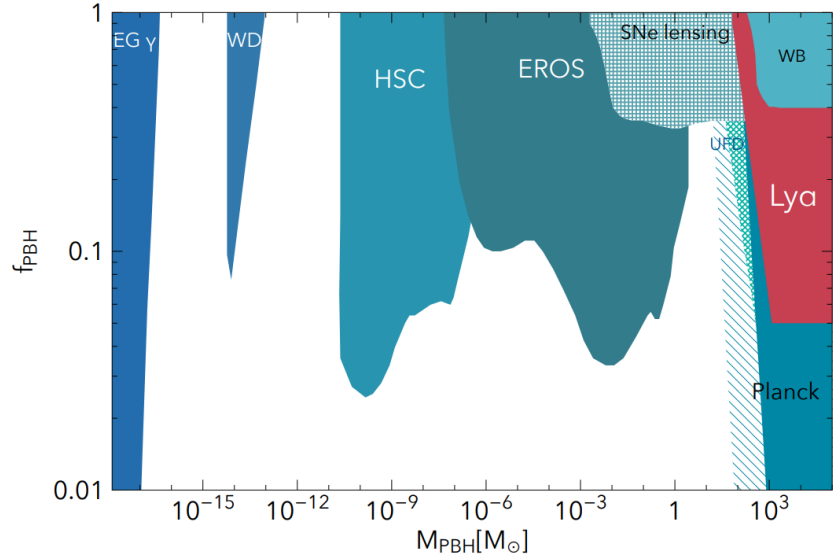


Figure 2.4: Other current constraints from several probes on primordial black hole abundance as function of their masses. We can see that these constraints are slightly different from those in Fig. 2.3. This is because of the different astrophysical assumptions. With these assumptions, PBHs in the mass window  $10^0 M_\odot \lesssim M_{PBH} \lesssim 10^2 M_\odot$  could still provide a non negligible fraction of dark matter. [47]

## 2.6 Claimed signatures

Although there is no ultimate evidence of Primordial Black Holes, some authors claimed to have found possible signatures of such objects. We will now review the most important ones, being aware that they are rather uncertain and to date there is no agreement on those.

### 2.6.1 Lensing evidence

Most of the claimed evidences exploit the lensing mechanism we already saw for the constraints. In particular, microlensing and millilensing techniques have led to possible positive evidence of Primordial Black Holes. For example, millilensing observation of the Andromeda Galaxy (M31) in [48] seemed to indicate the presence of one PBH candidate with mass  $10^{-10} M_\odot \lesssim M_{PBH} \lesssim 10^{-6} M_\odot$ . The same technique has been used again by the authors of [49] with the 5-year Optical Gravitational Lensing Experiment survey (OGLE) of the Galactic bulge. Using 2622 microlensing events they claimed to have found 6 candidates for Primordial Black Holes in the Earth-Jupiter mass range  $10^{-6} M_\odot \lesssim M_{PBH} \lesssim 10^{-3} M_\odot$ . Besides, the OGLE survey has detected 60 long-duration millilensing events in the galactic bulge with a mass distribution between  $0.8 M_\odot \lesssim M_{PBH} \lesssim 5 M_\odot$  [50] that could be associated to PBHs. Instead, by making use of quasar millilensing, two different authors claimed to have found Primordial Black Holes, of around  $1 M_\odot$  in [51], while  $0.05 M_\odot \lesssim M_{PBH} \lesssim 0.45 M_\odot$  in [52]. Lastly, the MAssive Compact Halo Object (MACHO) collaboration searched for microlensing towards the Large Magellanic Cloud (LMC), finding 17 candidate events; they found that the most likely MACHO mass is between  $0.15 M_\odot \lesssim M_{PBH} \lesssim 0.9 M_\odot$  [43]. Note that all these observations could be related also to other compact objects.

### 2.6.2 Dynamical and Accretion evidence

One argument for the existence of Primordial Black Holes concerns ultra faint dwarf galaxies. Indeed, CDM-dominated UFDGs would be dynamically unstable if Primordial Black Holes were present with appreciable abundance. Therefore, the non-detection of such galaxies smaller than  $r_c \sim 10 - 20$  pc, despite their magnitude being above the detection limit, could suggest the presence of PBH in the halo. Moreover, recent N-body simulations seem to support this hypothesis [21].

Another point for PBHs can be made by requiring  $f_{PBH} \ll 1$ : the  $10^6 - 10^{10} M_\odot$  supermassive black holes at the center of galaxies in this case could actually be of primordial origin and seed the formation of their hosts. Indeed, PBHs of  $10^5 - 10^6 M_\odot$  (produced in some models due to the primordial softening of the pressure at  $e^+ - e^-$  annihilation at  $t = 10$  s [15]) could accrete and drastically increase their masses. For a given PBH mass distribution, it is possible to calculate the number of supermassive PBHs for each halo. Assuming a standard Press-Schechter halo mass function and identifying the PBH mass that has the same number density, one can obtain the relation  $M_h \approx M_{PBH}/f_{PBH}$ , in agreement with the observations [21].

Lastly, some authors [53] suggested that the level of infrared background could be related with an overabundance of high-redshift halos, that could be easily explained as the Poisson effect of solar-mass PBHs if they comprise a large fraction of dark matter. It is challenging to find other scenarios to produce such features [21].

### 2.6.3 LIGO-Virgo upper limits

Primordial Black Holes can form binary systems, either in the early Universe or when passing sufficiently close one to another, if they radiate enough energy in gravitational waves to become gravitationally bound (for more details, see Sec. 2.7). Therefore, the possibility that some of the  $\sim 90$  events detected so far by the LIGO-Virgo-KAGRA collaboration (see Subsection 3.3.1) were of primordial origin has been explored. It has been first argued that the event rate detected by LIGO-Virgo was compatible with PBHs comprising the totality of dark matter [54], but later refinements showed that this is not the case [55]. The general conclusion is that PBHs can comprise only a fraction of dark matter if the mass function is nearly monochromatic, while they could still provide the totality of dark matter if their mass function is extended. However, the PBH mass

distribution should peak at a lower-mass signal than the coalescence signal seen by LIGO-Virgo. Also a mixed scenario in which the LIGO-Virgo events are due to both stellar BHs and primordial ones is still open [21].

Moreover, even if the statistical significance of this result is low [56], most of the detected events have spins compatible with zero. As we saw in Section 2.4, this is actually a prediction of PBH models, while it is disfavoured for coalescences of stellar BHs. Also the mass distributions of the events seems hard to explain only through stellar evolution prescriptions, with at least one merging component in the pair-instability mass gap (i.e., with mass  $M = 150M_{\odot}$ ) [57].

## 2.7 Binary Formation

Primordial black hole binaries could have formed due to two mechanisms, operating at separate times in cosmic history: they could have formed primordially, if two PBHs decoupled from the cosmic expansion and became gravitationally bound, or they could have formed in the late Universe, if two PBHs had a close encounter. It is important to note that these two mechanisms are not incompatible, and therefore we need to understand the physics of each in order to figure out which one is more efficient.

### 2.7.1 PBH binary formation in the early Universe

We can start by considering the early Universe during the radiation dominated epoch. We saw in Sec. 2.3 that PBHs could have formed, and in Sec. 2.4 that initially they are not clustered, i.e. just after their formation in the early Universe PBHs were distributed sparsely in space. This means that the mean distance between two Primordial Black Holes at the time was much greater than the Hubble horizon [16], defined as  $r_H = c/H(z)$ . Due to the rapid cosmic expansion their mean distance, that we can denote as  $\ell_{PBH}(z)$ , grew proportionally to the scale factor  $a(t)$ . By solving the Friedmann equations (Eq. 1.18), we can see that during the radiation dominated epoch:

$$a(t) \propto t^{\frac{1}{2}} \quad \longrightarrow \quad \frac{d}{dt} a(t) = \dot{a}(t) \propto t^{-\frac{1}{2}}. \quad (2.12)$$

Given that we can write the Hubble horizon as  $r_H(z) = c/H(z)$ , where  $H(z) = \dot{a}(t)/a(t)$ , we can find that  $r_H(z) \propto H(z)^{-1} \propto t$ : the Hubble horizon grows in time. This also means that the mean distance between PBHs relative to the Hubble horizon decreases as the Universe expands:

$$\frac{\ell_{PBH}}{r_H} \propto t^{-\frac{2}{3}}. \quad (2.13)$$

To describe in detail this ratio, we can follow the procedure presented by the authors of [58]: we can rewrite everything using the scale factor normalized to unity at matter-radiation equality,

$$s = \frac{1 + z_{eq}}{1 + z}, \quad (2.14)$$

where  $z_{eq} \simeq 3400$  is indeed the redshift of the matter–radiation equality (see Sec. 1.6). Since the Hubble rate can be written as:

$$H(z) = H_0 \sqrt{\Omega_M(1+z)^3 + \Omega_R(1+z)^4 + \Omega_{\Lambda}}, \quad (2.15)$$

the Hubble rate for a radiation-dominated Universe and with the normalized scale factor is:

$$H(z) \simeq H_0 \sqrt{\Omega_R} (1+z)^2 \longrightarrow H(s) \simeq \sqrt{\frac{8\pi G \rho_{eq}}{3}} s^{-2}, \quad (2.16)$$

where  $\rho_{eq}$  is the density (of matter or radiation) at equality:

$$\rho_{eq} = \rho_R(1+z_{eq})^4 = \rho_m(1+z_{eq})^3. \quad (2.17)$$

The characteristic comoving separation between two PBHs with mass  $M_{PBH}$  can be written as:

$$\bar{x} = \frac{1}{n_{PBH}^{1/3}} = \left( \frac{M_{PBH}}{f \cdot \rho_{eq}} \right)^{1/3} = \left( \frac{M_{PBH}}{f_{PBH} \cdot \rho_{DM}} \right)^{1/3} \frac{1}{1 + z_{eq}}. \quad (2.18)$$

where  $n_{PBH}$  is the comoving number density of PBHs and  $f = 0.85 \cdot f_{PBH}$  is the fraction of matter in the form of cold dark matter. Therefore, the mean physical distance  $\ell_{PBH}$  between PBHs can be written as:

$$\ell_{PBH} = \bar{x} \frac{1 + z_{eq}}{1 + z} = \left( \frac{M_{PBH}}{f_{PBH} \cdot \rho_{DM}} \right)^{1/3} \frac{1}{1 + z}. \quad (2.19)$$

The mean length normalized by the Hubble horizon is thus given by:

$$\frac{\ell_{PBH}}{r_H} = \frac{H(s)}{c} \left( \frac{M_{PBH}}{f_{PBH} \cdot \rho_{DM}} \right)^{1/3} \frac{1}{1 + z}. \quad (2.20)$$

Then, by rearranging this expression and substituting all the values of the constants (that can be found in the Physical constants section), we can find that:

$$\frac{\ell_{PBH}}{r_H} \simeq 6 \times 10^{-6} f_{PBH}^{-1/3} \left( \frac{1 + z}{1 + z_{eq}} \right) \left( \frac{M_{PBH}}{30 M_\odot} \right)^{1/3}. \quad (2.21)$$

for  $z > z_{eq}$ . Therefore, unless  $f_{PBH}$  is extremely small as  $f_{PBH} \lesssim 10^{-15}$ , for stellar-mass Primordial Black Holes there is a period in the radiation-dominated epoch in which there are typically more than one PBH in the Hubble horizon.

We can now study the motion of two PBHs in this phase of the Universe history, following the analysis developed in [58]. We can consider two point masses with the same  $M_{PBH}$  that are initially at comoving separation  $x$ , with vanishing peculiar velocity, in an homogeneous expanding Universe. We can characterize their motion with the dimensionless parameter  $X$ :

$$X = \left( \frac{x}{\bar{x}} \right)^3. \quad (2.22)$$

Indeed, the solution of the equation of motion is entirely characterized by  $\lambda$ , defined as [58]:

$$\lambda \equiv \frac{X}{f} = \frac{1}{f} \left( \frac{x}{\bar{x}} \right)^3, \quad (2.23)$$

where  $f$  was previously defined. If  $\lambda < 1$ , the PBH pair effectively decouples from the expansion, since the Newtonian force dominates in the equation of motion. Thus, a PBH pair becomes gravitationally bound if:

$$\frac{X}{f} < 1 \longrightarrow x < x_{max} \equiv f^{1/3} \bar{x} = f^{1/3} \ell_{PBH}(z = z_{eq}). \quad (2.24)$$

The redshift of decoupling  $z_{dec}$  can be computed by requiring that also the corresponding scale factor is of the order of  $\lambda$  [16], [58]:

$$s_{dec} = \frac{1 + z_{eq}}{1 + z_{dec}} \approx \lambda \longrightarrow 1 + z_{dec} = (1 + z_{eq}) \left( \frac{\bar{x} f^{1/3}}{x} \right)^3 = (1 + z_{eq}) \left( \frac{x_{max}}{x} \right)^3. \quad (2.25)$$

Another effect needs to be taken into account. As the two PBHs come closer, the surrounding PBHs, especially the nearest one, exert torques on the bound system. As a result, the two PBHs avoid a head-on collision, and typically form a highly eccentric binary [16], which emits gravitational radiation and eventually merges. A schematic representation of the mechanism of pair formation in the early Universe just presented can be seen in Fig. 2.5, which was taken from [16].

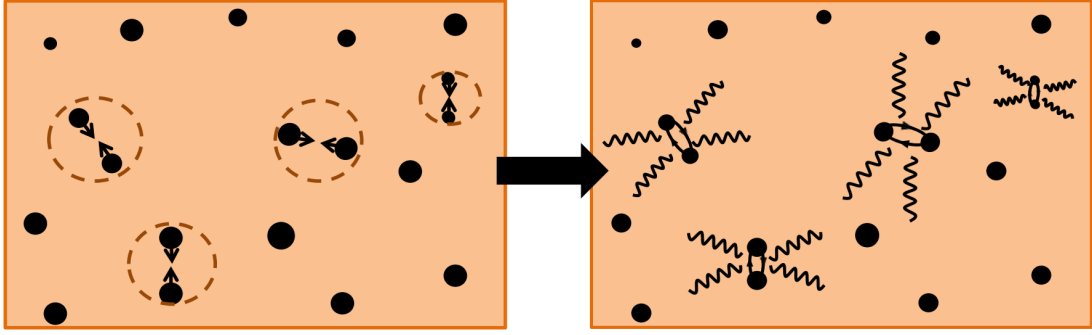


Figure 2.5: Schematic representation of the mechanism of pair formation in the early Universe: when two PBHs are separated by a comoving distance  $x < x_{max}$ , they decouple from the Hubble flow, becoming gravitationally bound and forming highly eccentric binaries. [16]

### 2.7.2 PBH binary formation in the late Universe

In addition to the mechanism just seen, Primordial Black Holes could form also in the late Universe. Indeed, let us consider a situation where a PBH traveling in space has a near-miss with another PBH. These PBHs may be concentrated in a local region, such as inside a larger dark matter halo, or simply moving freely in space [16].

We can thus consider two PBHs of mass  $m_A$  and  $m_B$ , each of those with their own velocity  $v_A$  and  $v_B$  and with relative velocity at infinity  $v_0$ . The impact parameter  $b$  of the system can be expressed by:

$$b = \frac{GM}{v_0^2} \sqrt{e^2 - 1} \quad (2.26)$$

where  $M = m_A + m_B$  is the total mass of the system and  $e$  is the eccentricity. The eccentricity of an orbit is a non-negative number that defines its shape and that can be written as:

$$e = \sqrt{1 + \frac{2EL^2}{\mu^3 G^2 M^2}} \quad (2.27)$$

where  $E$  is the orbital energy (sum of the potential energy  $E_p = -G\mu/r$  and the kinetic energy  $E_\infty = \mu v_0/2$ ),  $L$  is the angular momentum and  $\mu$  is the reduced mass of the system  $\mu = \frac{m_A m_B}{M}$ . A circular orbit has  $e = 0$ , an elliptic one has  $0 < e < 1$ , a parabolic motion has  $e = 1$  while an hyperbolic one has  $e > 1$ . The condition for which two PBHs form a binary is that the energy radiated in the form of gravitational waves during their encounter, denoted as  $\Delta E_{GW}$ , must exceed the kinetic energy  $E_\infty$ . The energy loss due to gravitational radiation in the Newtonian limit is given by [59]:

$$\Delta E_{GW} = -\frac{8}{15} \frac{G^{7/2}}{c^5} \frac{M^{1/2} m_A^{2/3} m_B^{2/3}}{r_{min}^{7/2}} f(e), \quad (2.28)$$

where  $r_{min} = (GM/v_0^2)(e - 1)$  is the distance of closest approach and

$$f(e) = \frac{1}{(e + 1)^{7/2}} \left[ 24 \arccos \left( -\frac{1}{e} \right) \left( 1 + \frac{73}{24} e^2 + \frac{37}{96} e^4 \right) + \sqrt{e^2 - 1} \left( \frac{301}{6} + \frac{673}{12} e^2 \right) \right]. \quad (2.29)$$

The maximal impact parameter so that the condition  $E_\infty \leq |\Delta E_{GW}|$  is satisfied and a binary can form can be rewritten as:

$$b_{max} = \sqrt{2} \left( \frac{85\pi}{6\sqrt{2}} \right)^{1/7} \frac{GM^{5/7}}{c^2} (m_A m_B)^{1/7} \left( \frac{c}{v_0} \right)^{9/7}. \quad (2.30)$$

The mechanism of binary formation in the late Universe is depicted in Fig. 2.6.

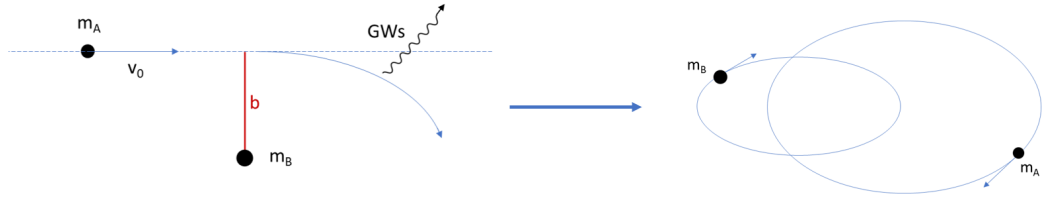


Figure 2.6: Schematic representation of binary formation in the late Universe due to a near-miss of two PBHs traveling in space.

After the formation of the PBH binaries, the system evolves, emitting gravitational waves and eventually merging. The rate of such process is strictly related to the rate of binary formation combined to the time delay between the formation and the merger. In Chapter 3 we will present gravitational waves, while in Sec. 4.3 we will analyse in detail the rate of such events.

### 2.7.3 Hyperbolic encounters

Another interesting case is to consider two PBHs with the opposite condition on the energies described in the previous section. Indeed, we could consider the case in which the kinetic energy exceeds the energy lost due to gravitational radiation, i.e.,  $E_\infty > |\Delta E_{GW}|$ . This requirement is equivalent to consider the impact parameter  $b$  greater than the maximum impact parameter for binary formation (Eq. 2.30). Therefore, the two Primordial Black Holes can not form a binary, but they continue their motion in an hyperbolic trajectory, as depicted in Fig. 2.7. During this process, the scattering of one primordial black hole on the other induces gravitational radiation emission, which is maximal at the point of closest approach. Studies on hyperbolic encounters are still ongoing (see e.g., [60] [61] [62]), but their gravitational emission seem to be negligible with respect to the binary one. For this reason, we decided not to include them in the analysis developed in chapter 5.

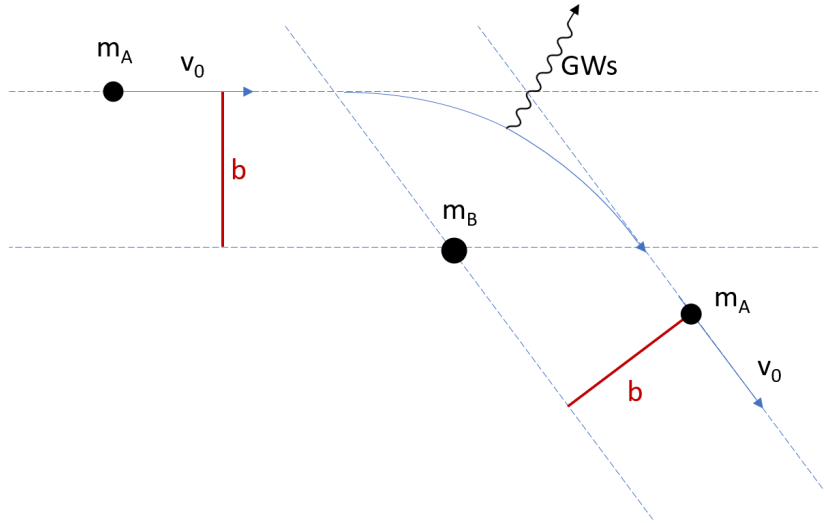


Figure 2.7: Schematic representation of hyperbolic encounter between two PBHs.



# Chapter 3

## Gravitational Waves

### 3.1 Introduction to Gravitational Waves

Gravitational Waves (GW) are solutions of linearized vacuum Einstein's equations and therefore they are a direct consequence of General Relativity [63]. Just as an accelerated electro-magnetic charge produces electro-magnetic waves, gravitational waves are produced when a mass accelerates. Indeed, gravitational waves are generated by a time-varying quadrupole moment in the mass distribution. In this Section we will analyze the general context for gravitational waves, while in Sec. 4.1 we will provide some examples of the astrophysical sources involved in the emission of GWs.

Since we are working in linearized general relativity, gravitational waves are assumed to introduce only a slight modification to flat space-time:

$$g_{\mu\nu}(x) \simeq \eta_{\mu\nu} + h_{\mu\nu}(x), \quad (3.1)$$

where  $g_{\mu\nu}(x)$  is the spacetime metric,  $\eta_{\mu\nu}$  is the Minkowski flat metric and  $h_{\mu\nu}(x) \ll 1$  is the metric perturbation. Thus, the line element can be written as:

$$ds^2 = g_{\mu\nu}(x)dx^\mu dx^\nu \simeq [\eta_{\mu\nu} + h_{\mu\nu}(x)]dx^\mu dx^\nu. \quad (3.2)$$

We saw in Sec. 1.2 that the Einstein's equations can be written as:

$$R_{\mu\nu} - \frac{R}{2}g_{\mu\nu} = 8\pi G T_{\mu\nu}, \quad (3.3)$$

where  $R_{\mu\nu}$  is the Ricci tensor,  $R = g^{\mu\nu}R_{\mu\nu}$  is the Ricci scalar and  $T_{\mu\nu}$  is the stress-energy tensor, which describes the density and flux of energy and momentum in spacetime. In turn, the Ricci tensor can be written as  $R_{\mu\nu} = R_{\mu\alpha\nu}^\alpha$ , where  $R_{\mu\sigma\nu}^\alpha$  is the Riemann tensor, that takes the following form:

$$R_{\mu\sigma\nu}^\alpha = \partial_\sigma \Gamma_{\mu\nu}^\alpha - \partial_\nu \Gamma_{\mu\sigma}^\alpha + \Gamma_{\sigma\lambda}^\alpha \Gamma_{\mu\nu}^\lambda - \Gamma_{\nu\lambda}^\alpha \Gamma_{\mu\sigma}^\lambda. \quad (3.4)$$

By writing the Riemann tensor we exploited the Christoffel symbols, defined as:

$$\Gamma_{\mu\nu}^\alpha \equiv \frac{1}{2}g^{\alpha\lambda}(g_{\lambda\mu,\nu} + g_{\lambda\nu,\mu} - g_{\mu\nu,\lambda}) \quad (3.5)$$

where we used the convention  $g_{\lambda\mu,\nu} = \partial_\nu g_{\lambda\mu} = \frac{\partial g_{\lambda\mu}}{\partial x^\nu}$ .

Since we want to study how GW propagates in the spacetime, we are interested in the vacuum solution of the Einstein's equations. In vacuum,  $T_{\mu\nu} = 0$  and so we want to solve  $R_{\mu\nu} - \frac{R}{2}g_{\mu\nu} = 0$ . Contracting this equation with  $g^{\mu\nu}$ , we can see that this is completely equivalent to solve  $R_{\mu\nu} = 0$ .

We can then proceed by substituting Eq. 3.1 in Eq. 3.5, obtaining the perturbed Christoffel symbols [63]:

$$\Gamma_{\mu\nu}^\alpha = \frac{1}{2}\eta^{\alpha\lambda}(h_{\lambda\mu,\nu} + h_{\lambda\nu,\mu} - h_{\mu\nu,\lambda}) \quad (3.6)$$

where we considered only the terms which make the Christoffel symbols at most of order  $O(h)$ . We can do the same for the Ricci tensor, obtaining then:

$$R_{\mu\nu} = \partial_\alpha \Gamma_{\mu\nu}^\alpha - \partial_\nu \Gamma_{\mu\alpha}^\alpha + O(h^2) \quad (3.7)$$

We can now insert Eq. 3.6 inside the last equation to compute also the perturbed Ricci tensor:

$$R_{\mu\nu} = \frac{1}{2} \eta^{\alpha\lambda} \partial_\alpha (h_{\lambda\mu,\nu} + h_{\lambda\nu,\mu} - h_{\mu\nu,\lambda}) - \frac{1}{2} \eta^{\alpha\lambda} \partial_\nu (h_{\lambda\alpha,\mu} + h_{\mu\lambda,\alpha} - h_{\mu\alpha,\lambda}) = \quad (3.8)$$

$$= \dots = -\frac{1}{2} \square h_{\mu\nu} + \frac{1}{2} \partial_\mu \left( \partial_\lambda h_\nu^\lambda - \frac{1}{2} \partial_\nu h \right) + \frac{1}{2} \partial_\nu \left( \partial_\lambda h_\mu^\lambda - \frac{1}{2} \partial_\mu h \right), \quad (3.9)$$

where we defined  $\square = \eta^{\alpha\lambda} \partial_\alpha \partial_\lambda$  as the d'Alembertian and  $h = h_\alpha^\alpha$  as the trace [63]. We would like to work in a coordinate system in which the Ricci tensor becomes simpler than the one found in Eq. 3.9. We can thus consider a change of coordinate between two different metrics that describe the same spacetime. The relation between the metrics can be written as [63]:

$$g_{\alpha\beta} = \frac{\partial \tilde{x}^\mu}{\partial x^\alpha} \frac{\partial \tilde{x}^\nu}{\partial x^\beta} \tilde{g}_{\mu\nu}. \quad (3.10)$$

Considering an infinitesimal change of coordinate  $\tilde{x}^\mu = x^\mu + \epsilon^\mu$ , with  $\epsilon \ll 1$ ,  $\tilde{g}_{\mu\nu} = \eta_{\mu\nu} + \tilde{h}_{\mu\nu}$  and  $g_{\alpha\beta} = \eta_{\alpha\beta} + h_{\alpha\beta}$ , we can find that, at linear order:

$$\tilde{h}_{\mu\nu} = h_{\mu\nu} - \partial_\mu \epsilon_\nu - \partial_\nu \epsilon_\mu. \quad (3.11)$$

Here,  $h_{\mu\nu}$  and  $\tilde{h}_{\mu\nu} = h_{\mu\nu} - \partial_\mu \epsilon_\nu - \partial_\nu \epsilon_\mu$  describe the same gravitational wave. We can thus make a gauge choice in which the Ricci tensor in Eq. 3.9 becomes simpler by imposing the so-called ‘‘harmonic gauge’’:

$$\partial_\lambda h_\nu^\lambda - \frac{1}{2} \partial_\nu h = 0. \quad (3.12)$$

To see if we can impose such condition, we must find an infinitesimal parameter  $\epsilon^\mu$  so that, starting from a generic  $h_{\mu\nu}$ ,  $\tilde{h}_{\mu\nu} = h_{\mu\nu} - \partial_\mu \epsilon_\nu - \partial_\nu \epsilon_\mu$  satisfies the harmonic gauge condition. If we choose  $\epsilon_\nu$  so that  $\square \epsilon_\nu = \partial_\lambda h_\nu^\lambda - \frac{1}{2} \partial_\nu h$ , it can be shown that the transformed field  $\tilde{h}_{\mu\nu}$  satisfies  $\partial_\lambda \tilde{h}_\nu^\lambda - \frac{1}{2} \partial_\nu \tilde{h} = 0$ . Therefore we are left with:

$$\begin{cases} \tilde{R}_{\mu\nu} = -\frac{1}{2} \square \tilde{h}_{\mu\nu} \\ \partial_\lambda \tilde{h}_\nu^\lambda - \frac{1}{2} \partial_\nu \tilde{h} = 0 \end{cases}. \quad (3.13)$$

and since the gravitational wave satisfies  $\tilde{R}_{\mu\nu} = 0$ , we have that:

$$\begin{cases} \square \tilde{h}_{\mu\nu} = 0 \\ \partial_\lambda \tilde{h}_\nu^\lambda - \frac{1}{2} \partial_\nu \tilde{h} = 0 \end{cases}. \quad (3.14)$$

The simplest gravitational wave in the harmonic gauge is a plane wave [63]:

$$h_{\mu\nu}(t, \bar{x}) = C_{\mu\nu} e^{ik \cdot x} \quad (3.15)$$

where  $C_{\mu\nu}$  is constant and  $k^\alpha = (k, \bar{k})$  is the 4-wavenumber. Indeed, it can be shown that the plane wave in Eq. 3.15 satisfies  $\square h_{\mu\nu} = 0$  if  $k^2 = 0$  (and this is the case). The 4-momentum of the gravitational wave can be written as  $p^\mu = \hbar k^\mu$ , and since we saw that  $k^2 = 0$ , also  $p^2 = 0$ . Therefore, a gravitational wave propagates along null geodesics with the speed of light [63].

However, the system in Eq. 3.14 does not admit a unique solution. Indeed, if  $\tilde{h}_{\mu\nu}$  is a solution, also  $\tilde{\tilde{h}}_{\mu\nu} = \tilde{h}_{\mu\nu} + \partial_\mu \tilde{\epsilon}_\nu + \partial_\nu \tilde{\epsilon}_\mu$  with  $\square \tilde{\epsilon}_\mu = 0$  is a solution of the system. Therefore, we have a residual gauge freedom, which we want to fix. Since  $\square \epsilon_\mu = 0$  (where for simplicity we dropped the tilde symbol), we can choose it to be a plane wave too:

$$\epsilon_\mu = \gamma_\mu e^{ik \cdot x}, \quad (3.16)$$

with  $\gamma_\mu$  constant and  $k^2 = 0$ . If we now insert this equation and Eq. 3.15 inside  $\tilde{h}_{\mu\nu} = h_{\mu\nu} - \partial_\mu \epsilon_\nu - \partial_\nu \epsilon_\mu$  we can find that:

$$\tilde{C}_{\mu\nu} = C_{\mu\nu} - ik_\mu \gamma_\nu - ik_\nu \gamma_\mu. \quad (3.17)$$

In order to fix the freedom, we can now select  $\gamma_0$  and  $\gamma_i$  with ( $i = 1, 2, 3$ ) so that we can find the following 4 extra constraints:

$$\tilde{C}_{00} = \tilde{C}_{01} = \tilde{C}_{02} = \tilde{C}_{03} = 0 \implies \tilde{C}_{00} = \tilde{C}_{0i} = 0 \implies \tilde{h}_{00} = \tilde{h}_{0i} = 0. \quad (3.18)$$

Thus, the system can now be written as:

$$\begin{cases} \square \tilde{h}_{\mu\nu} = 0 \\ \partial_\lambda \tilde{h}_\nu^\lambda - \frac{1}{2} \partial_\nu \tilde{h} = 0 \\ \tilde{h}_{00} = \tilde{h}_{0i} = 0 \end{cases} \longrightarrow \begin{cases} \square h_{\mu\nu} = 0 \\ \partial_\lambda h_\nu^\lambda - \frac{1}{2} \partial_\nu h = 0 \\ h_{00} = h_{0i} = 0 \end{cases}, \quad (3.19)$$

where again we dropped the tilde symbols for simplicity. Once we specify the initial conditions, this set of equations has no residual freedom and therefore it admits a unique solution [63].

We can now study the meaning of those 4 extra conditions: inserting the last line of the system in the harmonic gauge (second line of the system), we can see that:

- $\partial_0 h_{ii} = 0$ , and from the form of the plane wave solution we can write that  $h_{ii} = 0 \longrightarrow h = 0$ . This means that the gravitational wave is traceless.
- $\partial_i h_{ij} = 0$ , and this means that the gravitational wave is transverse.

Let us now understand what is  $h_{\mu\nu}$  and what are the consequences of the constraints. Before gauge fixing,  $h_{\mu\nu}$  is a symmetric  $4 \times 4$  object, with 16 total entries, but only 10 independent ones:

$$h_{\mu\nu} = \begin{pmatrix} \cdot & \cdot & \cdot & \cdot \\ \cdot & \cdot & \cdot & \cdot \\ \cdot & \cdot & \cdot & \cdot \\ \cdot & \cdot & \cdot & \cdot \end{pmatrix} \quad (3.20)$$

The harmonic gauge poses 4 conditions, and therefore we are left with  $10-4=6$  independent entries. The residual gauge fixing poses 4 additional conditions, and so eventually we are left with  $6-4=2$  independent entries. These are the two gravitational wave polarizations. To see explicitly this, let us consider the 3-dimensional space and orient the z-axis in the direction of motion of the wave, so that  $k_x = k_y = 0$  and  $k = k_z$ . We have seen that  $h_{00} = h_{0i} = h_{ii} = \partial_i h_{ij} = 0$  and since  $h_{\mu\nu}(t, \bar{x}) = C_{\mu\nu} e^{ik \cdot x}$ , these conditions can be rewritten as  $C_{00} = C_{0i} = C_{ii} = k_i C_{ij} = 0$ . We can use the last relation to find that  $C_{3j} = 0$ , and so  $C_{13} = C_{23} = C_{33} = 0$ . With  $C_{33} = 0$ , we can exploit the traceless condition  $C_{ii} = 0$  to write that  $C_{11} + C_{22} = 0 \longrightarrow C_{11} = -C_{22}$ . Eventually, we are left with the two independent possibilities

$$C_{11} = -C_{22} \quad \text{and} \quad C_{12} = C_{21}. \quad (3.21)$$

We have found explicitly the two gravitational wave polarizations. Then, let us introduce two basis elements:

$$e_{ij,+} \equiv \begin{pmatrix} 1 & 0 & 0 \\ 0 & -1 & 0 \\ 0 & 0 & 0 \end{pmatrix} \quad \text{and} \quad e_{ij,\times} \equiv \begin{pmatrix} 0 & 1 & 0 \\ 1 & 0 & 0 \\ 0 & 0 & 0 \end{pmatrix}. \quad (3.22)$$

A gravitational wave can be then decomposed as:

$$h_{ij} = (h_+ e_{ij,+} + h_\times e_{ij,\times}) e^{ik \cdot x} \quad (3.23)$$

where  $h_+$  and  $h_\times$  are the amplitudes of the two polarizations. Moreover, we can observe that the +-mode is the  $\times$ -mode rotated by  $45^\circ$ . Indeed:

$$R e_\times R^T = e_+ \quad \text{where} \quad R = \begin{pmatrix} \frac{1}{\sqrt{2}} & \frac{1}{\sqrt{2}} & 0 \\ -\frac{1}{\sqrt{2}} & \frac{1}{\sqrt{2}} & 0 \\ 0 & 0 & 1 \end{pmatrix}. \quad (3.24)$$

The effect of the two different polarizations of the gravitational wave on a circle of free masses is depicted in Fig. 3.1, taken from [64].

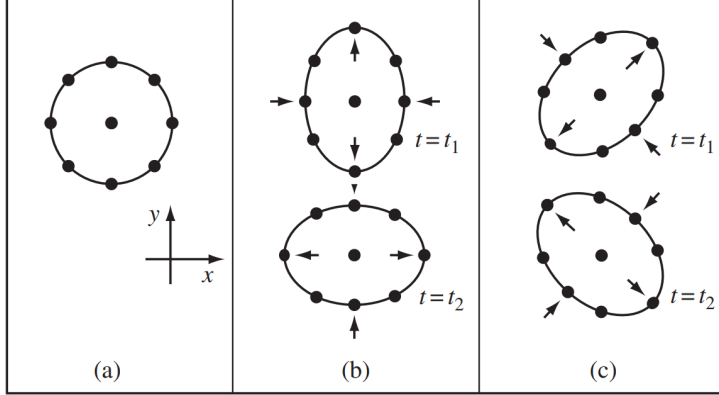


Figure 3.1: In panel (a) we can see a circle of free particles before a wave traveling in the  $z$  direction reaches them. Particles are positioned according to their proper distances from one another. In panel (b) we can observe distortions of the circle produced by a wave with the  $+$  polarization. The two pictures inside the panel represent the same wave at phases separated by  $180^\circ$ . Panel (c) is the same as panel (b), but for the  $\times$  polarization. [64]

We can detect gravitational waves in two ways: indirectly, by looking at the effects that GWs leave on astrophysical systems, or directly, by considering the imprints of GWs on the detectors. In Section 3.2 we briefly introduce the former techniques, while in Sec. 3.3 we will study gravitational waves directly detectable by Earth-based and space-based interferometers. In general, we can divide gravitational waves in four categories according to their sources:

**Compact binary inspiral:** These GWs are produced by orbiting pairs of massive compact objects like black holes, neutron stars and white dwarfs. So far, all of the objects the interferometers have detected fall into this category. [65] [46] As the orbit of the two objects shrinks, the frequency of the signal increases, until they finally merge. The frequency of the gravitational waves emitted by the binary will depend on the coalescing masses.

**Burst:** Gravitational waves in this category are characterized by short duration sources, such as supernovae and gamma ray bursts.

**Continuous:** Continuous GWs generate from single spinning massive object, e.g. neutron stars (NS), due to imperfections in their spherical shape.

**Stochastic:** This type of GWs is the uncoherent superposition of all the unresolved independent contributions in the Universe from both astrophysical and cosmological origin.

A detailed description of all these sources can be found in [63]. In this Master thesis, particularly in Chapter 4 and Chapter 5, we will focus on the stochastic gravitational wave signal.

## 3.2 Indirect evidence of gravitational waves

According to General Relativity, a binary system with objects orbiting around their center of mass loses energy emitting gravitational waves. As a result, their orbit shrinks [63]. The first detection of such phenomenon was in 1978, four years after the discovery of the PSR1913+16 binary system by R. A. Hulse and J. H. Taylor [66], [67]. This binary system consists of two neutron stars, one of which is a pulsar that emits electro-magnetic pulses at radio frequencies at precise, regular intervals as it rotates. However, the intervals between two consecutive pulses have been observed to shrink. Thus, it has been shown [67] that the orbit period is declining: the two astronomical bodies are rotating faster and faster around each other in an increasingly tight orbit, although the change is very small. It has been proven that the energy lost by the shrinking system agrees accurately with

the predicted energy that would be radiated by gravitational waves. This can be seen in Figure 3.2, which was taken from [67].

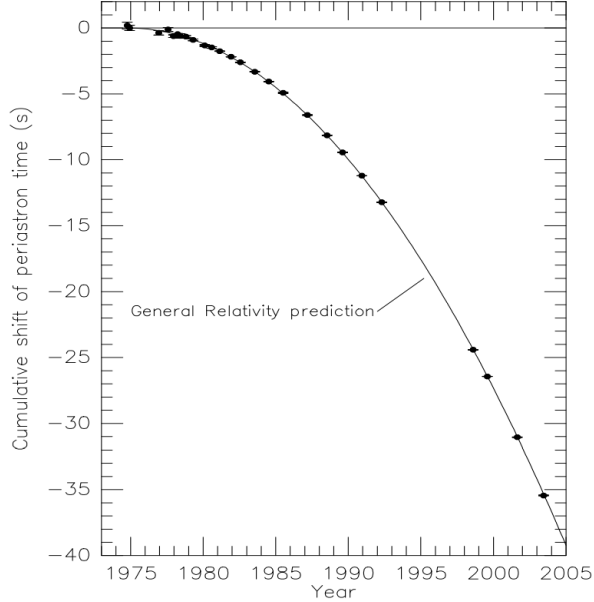


Figure 3.2: Comparison between the expected cumulative shift in time of the periastron for a system emitting gravitational radiation according to general relativity (solid line) and the observed shift in time of the periastron (dots) of the so-called Hulse-Taylor pulsar (PSR B1913+16) [67]. We can see that general relativity predicts very accurately the cumulative shift of periastron time.

### 3.3 Direct evidence of gravitational waves: GW Detectors

In order to test the current theories of gravitation and to observe gravitational waves, many gravitational wave detectors have been built, with many others planned in the future. On September 14, 2015 the first direct detection of gravitational waves was finally made [68]. Since then, gravitational physics and these observatories have given us a completely new tool to comprehend and study the Universe. In this section we are going to see and describe the current and future gravitational wave detectors. When discussing gravitational waves detectors, the most common parameter to describe their amplitude is a dimensionless strain, the so called characteristic strain  $h_c(f)$ . The characteristic strain is designed to include the effect of integrating an inspiralling signal, depends on the frequency  $f$  and it is defined as [69]:

$$[h_c(f)]^2 = 4f^2 |\tilde{h}(f)|^2 \quad (3.25)$$

where  $\tilde{h}_c(f)$  is the Fourier transform of the source signal.

#### 3.3.1 LIGO-Virgo-KAGRA collaboration

LIGO (Laser Interferometer Gravitational-wave Observatory)<sup>1</sup> is the world's largest gravitational wave observatory. It consists of two laser interferometers 3000 km apart, one in Hanford and the other in Livingston. Each of those is a L-shaped Michelson interferometer with a Fabri-Perot cavity integrated. The arms are 4 km long and mirrors, acting as test masses, are positioned at the arms' extremities. The laser beam is first split and then recombined in search for gravitational waves. Indeed, any alteration in the distance between mirrors produces a very small shift in phase between the two beams and thus a variation of the intensity of the light, which in turn is proportional to the

<sup>1</sup><https://www.ligo.org/>

GW's amplitude. Virgo<sup>2</sup> and KAGRA<sup>3</sup> (KAmioka GRAvitational wave detector) are two other gravitational wave interferometers, based on the same concepts, but with slightly shorter arms (3 km each) and located respectively in Italy and in Japan. Together, they search for gravitational waves in the frequency band between  $\sim 10$  Hz and  $\sim 10$  kHz. Their sensitivity at low frequencies is mainly limited by the arm lengths, by seismic noise and by interference from nearby moving masses. This range of frequencies is populated mostly by merging compact binaries of  $\sim 10 - 100 M_{\odot}$ . The gravitational wave sensitivities of the three interferometers using the characteristic strain can be seen in Figure 3.6 in black, orange and red.



Figure 3.3: LIGO, Virgo and KAGRA Interferometers.

Up to now, three observing runs (O1, O2 [65] and O3 [46]) have been completed and at least two are planned (O4 and O5). In the first observing run (September 12, 2015 to January 19, 2016) the LIGO collaboration reported three gravitational wave signals, while in the second one (November 30, 2016 to August 25, 2017) eight more detections were announced. The first (April 1, 2019 to October 1, 2019) and the second (November 1, 2019 to March 27, 2020) part of O3 brought eventually to 90 the total number of observed events since LIGO/Virgo operations began. In Figure 3.4 taken from [70], we can see the current catalog of all the detected events so far.

### 3.3.2 Pulsar Timing Array and SKA

A pulsar is a highly magnetized rotating neutron star that emits beams of electromagnetic radiation. A Pulsar Timing Array is a set of pulsars constantly monitored by several ground-based radio telescopes collecting the times of arrival of those pulses [71]. This type of experiments can be exploited in Gravitational-Wave astronomy. Indeed, GWs passages can stretch and compress space-time; as a result, the time of flight of the pulses is not constant, but longer or shorter depending on the presence of gravitational waves. The International Pulsar Timing Array (IPTA) [72] is a consortium of consortia, comprised of the European Pulsar Timing Array (EPTA), the North American Nanohertz Observatory for Gravitational waves (NANOGrav) and many others. Through sharing resources and creating combined pulsar timing data sets, the IPTA is constructing the most sensitive low-frequency gravitational wave detector possible. The frequency range to which PTAs are sensitive is determined by the duration of the observation campaign and the cadence of observations. The current observation campaign is thirteen years long, and observations are performed mainly once per week. This leads to sensitivity in the frequency range between  $10^{-9}$  Hz and  $10^{-6}$  Hz [71]. The advent of next generation radio telescope facilities, such as the Square Kilometer Array (SKA, planned to be operative in 2027 [73]), will improve the pulsar catalogs: such new facilities will be able to use hundreds of well timed millisecond pulsars rather than the few dozens in existing PTAs. The prospective sensitivity for SKA can be seen in blue in Figure 3.6. At the moment it is unlikely to detect single events by PTAs [71] and therefore the main goal of such experiments is measuring the amplitude of the background gravitational waves.

<sup>2</sup><https://www.virgo-gw.eu/>

<sup>3</sup><https://gwcenter.icrr.u-tokyo.ac.jp/en/>

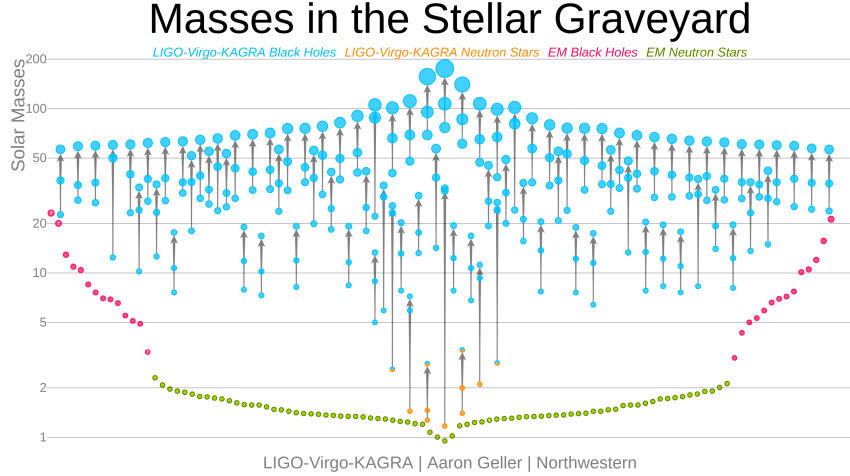


Figure 3.4: Current catalog of all the detected events so far from the LIGO-Virgo-KAGRA collaboration [70]

### 3.3.3 LISA

LISA (Laser Interferometer Space Antenna) [74] is a future experiment scheduled to launch in the 2030s that consists of three spacecraft forming an equilateral triangle in space. Its arms will be millions of kilometers long and will be following tens of millions of kilometers behind the Earth as we orbit the Sun. The three spacecrafts will transmit laser beams between the different spacecrafts and will study the interference between the signals to search for gravitational wave signatures. From space, LISA can avoid the seismic noise which Earth-based detectors have and access regions of the spectrum that are inaccessible from Earth due to these extremely long arms. The LISA observatory is designed to explore the low frequency portion of the GW spectrum between 0.1 mHz and 1 Hz [74]. The different frequency with respect to the LIGO-Virgo-KAGRA collaboration means that the waves LISA is looking for have a much longer wavelength, corresponding to objects in much wider orbits and potentially much heavier than those the current interferometers are searching for. LISA's gravitational wave sensitivity can be seen in green in Figure 3.6.

### 3.3.4 Einstein Telescope

The Einstein Telescope (ET) is a proposed underground infrastructure that will host a third-generation gravitational wave observatory [75]. One of the proposed configurations for ET consists in three arms composing an equilateral triangle, with two detectors in each corner. Its expected sensitivity, reported in violet in Figure 3.6, will be enhanced compared to that of current interferometers by increasing the size of the arms to 10 kilometers and by implementing a series of new technologies [75]. ET will thus be sensitive to frequencies from 1 Hz, all the way up to 10 kHz. Thanks to the Einstein Telescope, the entire population of stellar and intermediate mass black holes will be accessible over the entire history of the Universe.

## 3.4 Stochastic Gravitational Wave Background

The Stochastic Gravitational Wave Background (SGWB) is very different from the other sources of GWs. Unlike the other categories, whose GWs come from specific locations in the sky, the SGWB comes from all directions. At first approximation, the SGWB can be thought as isotropic, even if ultimately will be anisotropic [76]. Indeed, we can imagine the properties of the SGWB as similar to those of the Cosmic Microwave Background, where small anisotropies rise over an isotropic background. If detected, the SGWB would appear as noise in a single detector, while with two or more of them one could possibly extract the signal through the correlation of data [76]. The detection of the SGWB will be of great importance, since it will provide many useful information about the Universe, its components and the phases of its history.

As we have already seen, up to now gravitational waves observatories have only detected GW single events. One of the most interesting challenges for the future of gravitational wave astronomy will be to detect and characterize the stochastic gravitational wave background, possibly disentangling most of its contributions. Indeed, a variety of sources contribute to this background. We will now briefly revise some of its most important GWs contributions as depicted in [76], but we are aware that many other mechanisms that produce GWs are present in the Universe.

### *Inflation*

The theory of inflation posits that in the very early moments of life the Universe's size grew exponentially [4]. Many models exists for this, one of the most popular assume that this would be possibly caused by the presence of a certain inflationary scalar field  $\phi$ . When the scalar field decayed, the inflationary process ended. Gravitational waves could be produced in the decaying of  $\phi$  during the so-called pre-heating phase [76]. Moreover, quantum fields like  $\phi$  have vacuum fluctuations associated to them. Scalar fluctuations of the inflaton would be the seeds for the distributions of matter that we observe in the Universe. However, also tensor fluctuations could be present and those would produce Gravitational waves [76]. The wavelengths of all the GWs produced during and after inflation would be from the size of the observable Universe down to subatomic scales and would compose a cosmological SGWB. The magnitude of the stochastic background depends on the inflationary model adopted.

### *Cosmic strings*

Cosmic strings are theorized one-dimensional topological defects produced after a spontaneous symmetry phase transition from a great variety of field theories, including, for example, Grand Unified Theories (GUTs) applied in the early Universe [76]. These cosmic strings would form at the end of inflation. When strings intersect, they form the so-called cusps and kinks. Cosmic string kinks are discontinuities on the tangent vector of a string, while cusps are points where the string instantaneously reaches the speed of light. These objects will create bursts of gravitational waves, whose superposition will create a cosmological stochastic background of gravitational waves [76].

### *Supernovae*

A Supernova is an explosion of a massive star at the end of its life. At first approximation, the supernova event is spherical, but if it has some asymmetry it then produces gravitational waves [76]. The sum of all these gravitational waves from SN over the all Universe would thus compose an astrophysical stochastic background. The SGWB originated from Supernovae is predicted through the study of stellar formation and evolution from Population III (the oldest star population) to Population I (the youngest one) [76].



Figure 3.5: Artists' impressions of SKA, LISA and ET Interferometers.

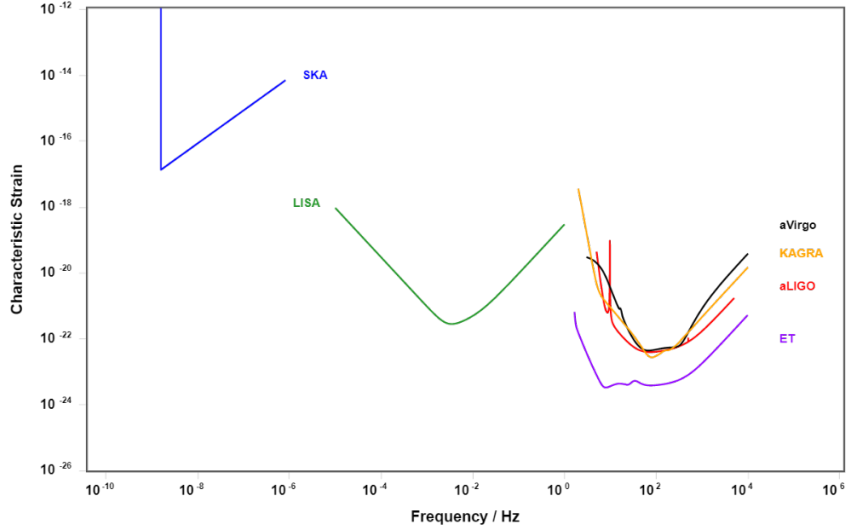


Figure 3.6: Gravitational wave sensitivity-curve plot using the characteristic strain defined in Eq. 3.25. [69]

### *Spinning neutron stars*

Non-axisymmetric spinning neutron stars are expected to be a detectable source of gravitational waves [76]. Indeed, GWs would be emitted if the neutron star is not perfectly spherical, namely if there is an asymmetry in its shape, e.g. a slight mountain on the neutron star surface. Pulsars are numerous in our galaxy, and presumably in the universe, and therefore they contribute to the astrophysical SGWB. The computation of the magnitude of that GW background depends both on the star formation rate and on the assumptions of the characteristics of such objects [76].

### *Binary Compact Objects*

Right after the first detection by LIGO of a binary black hole merger [68], it became clear that the Universe is populated by stellar mass black holes that are often bound in binaries. Therefore, a stochastic gravitational wave background of unresolved BH merger and inspiral events is present; in addition to that, a background component is present, due to all the interactions among COs which release gravitational waves, e.g. close hyperbolic encounters [76]. The magnitude and the shape of such a background depend on the characteristics of the underlying stellar population. In order to characterize the background we need to know, for example, the mechanisms by which binaries are formed, the star formation rate, the star evolution process, the distribution of mergers in redshift space, etc. This is as well true for pairs involving the other types of known compact object: at a certain level, also binary neutron stars and white dwarfs contribute to that background [76]. A special reference goes to Primordial Black Holes: if they exist, they produce a SGWB too. Indeed, the aim of the next sections of this Master thesis is to characterize and study it.



## Chapter 4

# Stochastic Gravitational Wave Background

The derivation of this Chapter will be applied only to the background from astrophysical sources, since the aim of this Master thesis is to characterize the SGWB from PBHs; for cosmological sources more information can be found in [77].

Now that we have seen its most important GWs contribution, we can begin to physically describe the general features of the Stochastic Gravitational Wave Background (SGWB), following the approach depicted in [78]. Its magnitude is usually expressed as the ratio between the gravitational wave energy density per unit interval of logarithmic frequency,  $\rho_{GW}$ , and the critical density of the Universe  $\rho_{c,0}$ , defined in Sec. 1.4:

$$\Omega_{GW}(f) \equiv \frac{1}{\rho_{c,0}} \frac{d\rho_{GW}(f)}{d \ln f}, \quad (4.1)$$

where  $f$  is the observed frequency, which is related to the frequency in the source frame through  $f_r = f(1+z)$ . Another important quantity in the context of the search for gravitational waves, used as well to express the amplitude of the wave, is the GW-strain amplitude, defined as:

$$h_c^2(f) = \frac{4G}{\pi f^2} \frac{d\rho_{GW}(f)}{d \ln f}. \quad (4.2)$$

The gravitational wave energy density per unit interval of logarithmic frequency introduced in Eq. 4.1 can be expressed in terms of  $F_f$ , the integrate flux received on Earth, as:

$$\frac{d\rho_{GW}(f)}{d \ln f} = \frac{f}{c^3} F_f, \quad (4.3)$$

where the integrate flux takes the following form:

$$F_f = \int d\theta p(\theta) \int dz \frac{dR^o(\theta, z)}{dz} f_f(\theta, z, f). \quad (4.4)$$

Here  $p(\theta)$  is the probability distribution of the parameters  $\theta$  that describe the source properties,  $\frac{dR^o(\theta, z)}{dz}$  is the number of sources in the interval  $[\theta, \theta + d\theta]$ , per unit of time in the observer frame and per redshift interval, and  $f_f(\theta, z, f)$  is the fluence of a source located at redshift  $z$ , that we can express as:

$$f_f(\theta, f) = \frac{1}{4\pi r(z)^2} \frac{dE_{GW}(\theta, f_r)}{df_r}, \quad (4.5)$$

where  $r(z)$ , which depends on the adopted cosmology, is the proper distance (Eq. 1.9) between the source and the observer, while  $E_{GW}$  is the gravitational spectral energy emitted in the source

frame  $\frac{dE_{GW}(\theta, f)}{df_r}$ . We can rewrite the first factor of the second integral as the observed event rate  $\dot{\rho}^o(\theta, z)$  (in  $\text{Mpc}^{-3}\text{yr}^{-1}$ ) times the comoving volume element  $\frac{dV}{dz}$ , getting:

$$\frac{dR^o(\theta, z)}{dz} = \dot{\rho}^o(\theta, z) \frac{dV}{dz} = \dot{\rho}^o(\theta, z) \frac{4\pi r(z)^2 c}{H(z)}, \quad (4.6)$$

where  $H(z)$  is the Hubble parameter, defined in Eq. 1.19. The observed event rate  $\dot{\rho}^o(\theta, z)$  can then be written as the intrinsic merger rate  $R(\theta, z)$  times the scale factor  $a(z) = (1+z)^{-1}$ :

$$\dot{\rho}^o(\theta, z) = \frac{R(\theta, z)}{1+z}. \quad (4.7)$$

By substituting all these contributions inside the original formulas for the magnitude of the SGWB (Eq. 4.1) and for the GW-strain amplitude (Eq. 4.2) we finally get [78]:

$$\Omega_{GW}(f) = \frac{1}{\rho_c c^2} \int d\theta p(\theta) \int dz \frac{R(\theta, z)}{(1+z)H(z)} \frac{dE_{GW}(\theta, f_r)}{df_r}, \quad (4.8)$$

and

$$h_c^2(f) = \frac{4G}{\pi c^2} \frac{1}{f} \int d\theta p(\theta) \int dz \frac{R(\theta, z)}{(1+z)H(z)} \frac{dE_{GW}(\theta, f_r)}{df_r}. \quad (4.9)$$

Therefore, by specifying the probability distribution of the source parameters, the observed event rate and the gravitational spectral energy emitted in the source frame, one can eventually find the explicit expression for  $\Omega_{GW}(f)$  or  $h_c^2(f)$ .

## 4.1 SGWB from astrophysical sources

All the known objects in the Universe (such as binary stars, binary astrophysical BHs, binary NSs, binary BH-NSs, Supernovae, etc.) contribute to a certain level to the stochastic gravitational wave background. To characterize it, we just saw that we need the probability distribution of the parameters of the source, the intrinsic merger rate and the gravitational spectral energy emitted in the source frame.

We can start from the middle one by considering that, regardless of the specific typology, all these objects share a common progenitor: stars. Then, the intrinsic merger rate of astrophysical objects can be written as the product of two pieces [78]:

$$R(\theta, z) = \lambda(\theta, z) \dot{\rho}_*(z) \quad (4.10)$$

where  $\lambda(\theta, z)$  is the mass fraction of a star that has been converted into a compact objects, which in turn depends on the initial mass function (IMF) of that star, while  $\dot{\rho}_*(z)$  represents the cosmic star formation rate (SFR, often given in  $M_\odot \text{yr}^{-1}$ ) which describes the total mass of stars formed per year. As we can see from Figure 4.1 taken from [79], the SFR is expected to increase rapidly between  $z \sim 0 - 1$ , peak around  $z \sim 1.7 - 1.8$  and then smoothly decrease at larger redshifts [79]. For what concerns the initial mass function, it seems that top heavy IMFs are preferred to the traditional Salpeter IMF, and the fits to observations of progenitor stars are optimized for IMFs of the form [78]:

$$\xi(m) \propto \begin{cases} \left(\frac{m}{m_0}\right)^{-1.5} & \text{for } 0.1M_\odot < m < m_0 \\ \left(\frac{m}{m_0}\right)^{-2.35} & \text{for } m_0 < m < 100M_\odot \end{cases} \quad (4.11)$$

where  $m_0 = 0.5M_\odot$  and the function is normalized within the mass interval  $0.1M_\odot - 100M_\odot$  so that  $\int m \xi(m) dm = 1$ .

The other important ingredient to characterize the SGWB is the gravitational spectral energy emitted by the source under consideration. Of course, this will depend on the specific typology of the source. We can now briefly analyze some examples to picture the different forms that the gravitational spectral energy could assume, saving for the next subsection a more detailed analysis:

- In the quadrupolar approximation, the gravitational wave energy spectrum emitted by a binary system (e.g. BNSs, BBHs, BHNSs) which inspirals in a circular orbit is given up to the last stable orbit by [78]:

$$\frac{dE_{GW}}{df} = \frac{\pi^{2/3}}{3} \frac{\mathcal{M}_c^{5/3} G^{2/3}}{f^{1/3}} \quad (4.12)$$

where  $\mathcal{M}_c$  is the Chirp Mass of the system, defined as  $\mathcal{M}_c^{5/3} = m_A m_B M^{-1/3}$ , with  $M = m_A + m_B$  being the total mass.

- Rotating neutron stars with a triaxial shape may have a time varying quadrupole moment and hence radiate GWs at twice their rotational frequency. The total spectral gravitational energy emitted by a neutron star is given by [78]:

$$\frac{dE_{GW}}{df} = K f^3 \left(1 + \frac{K}{\pi I_{zz}} f^2\right)^{-1} \quad (4.13)$$

where

$$K = \frac{192\pi^4 G I^3 \epsilon^2}{5c^5 R^6 B^2} \quad (4.14)$$

and  $R$  is the radius of the star,  $\epsilon$  is the ellipticity,  $I_{ij}$  are the principal axis of the moment of inertia  $I$  and  $B$  the projection of the magnetic dipole in the direction orthogonal to the rotation axis.

- Core collapse supernovae of stars with mass  $m$  resulting in black holes with mass  $M$  may generate GWs with spectral energy given by [78]:

$$\frac{dE_{GW}}{df} = \epsilon \alpha m c^2 \delta(f - f_*(M)) \quad (4.15)$$

where  $f$  is the frequency,  $\epsilon$  is an efficiency coefficient for axisymmetric collapse,  $\alpha = M/m$  is the fraction of the mass of the progenitor star converted in the BH,  $M$  is the BH mass and

$$f_*(m) = \frac{c^3 [1 - 0.63(1 - a)^{0.3}]}{2\pi G \alpha m (M_\odot)}, \quad (4.16)$$

is a characteristic frequency with  $a$  the dimensionless spin parameter of the black hole.

Many other examples could be made. In the next subsection we will analyze in detail a robust numerical approach to compute the SGWB for those that are thought to be the three main astrophysical contribution.

### 4.1.1 CLASS\_GWB

CLASS\_GWB is a robust numerical approach to simulate the astrophysical gravitational wave background developed by Bellomo *et al* [80]. We will now review the framework under which CLASS\_GWB has been developed, following the original paper by N. Bellomo *et al.* [80].

The main idea to simulate the SGWB is to generate a population of gravitational wave events, their signal and the detector capability to detect them. To generate a catalog of GW events which provides a fair sample of the underlying GW events population, the schematic approach depicted in Fig. 4.2 taken from [80] has been used.

First of all, the category of events must be selected. Since this work focuses on the astrophysical contributions to the SGWB, the three possible choices for mergers are BBH, BNS and BHNS. We note that up to now all the BHs under consideration are generated after stellar evolution. We can begin with the first step of this methodology: the arrival time of the signal at Earth must be computed. This can be done by supposing that the arrival time of the signal is a Poisson process. Then, the probability distribution function (pdf) of time intervals  $\Delta t$  between two subsequent events follows an exponential probability function:

$$p(\Delta t) = \frac{e^{-\Delta t/\bar{\Delta t}}}{\bar{\Delta t}}, \quad (4.17)$$

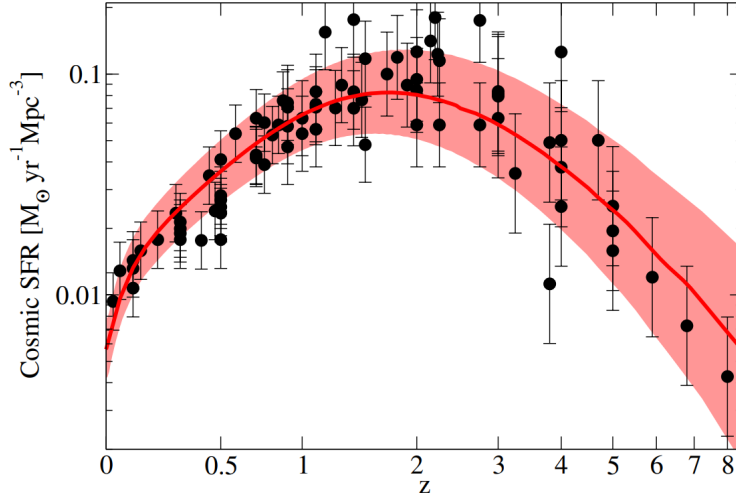


Figure 4.1: Observational constraints on the cosmic star formation rate (black points), compared to the best-fit model (red solid line) and the posterior  $1\sigma$  distribution (red shaded region). [79]

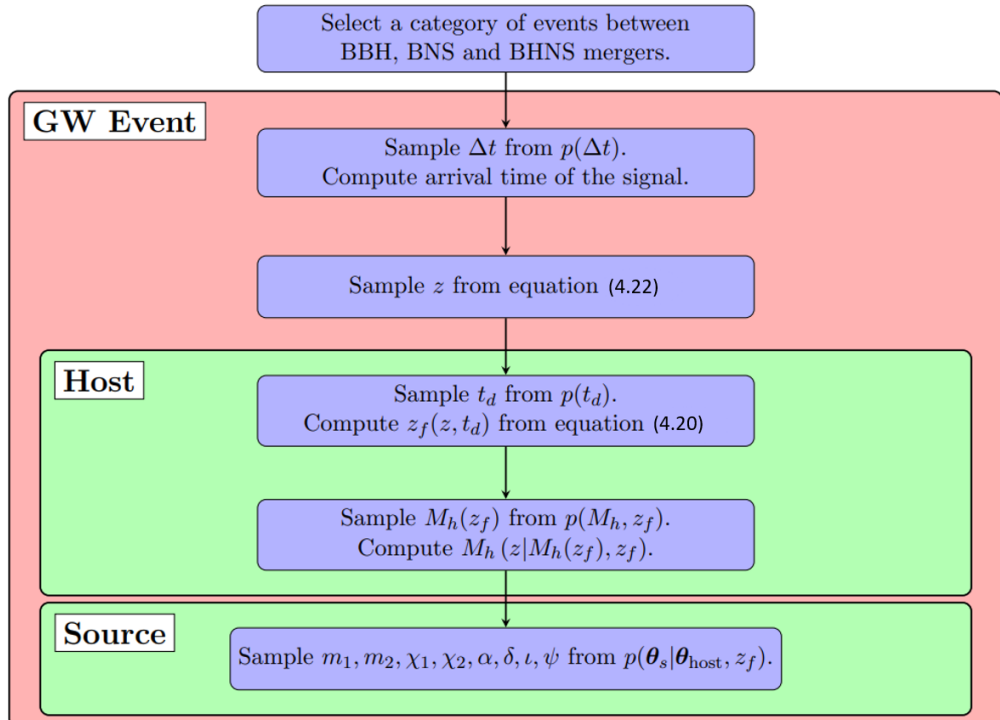


Figure 4.2: CLASS\_GWB operational scheme, taken from [80]

where  $\overline{\Delta t}$  is the average waiting time between signals. Fixing an initial time for the observations  $t_{in}$ , the events will arrive at the Earth at time  $t_1 = t_{in} + \Delta t_1$ ,  $t_2 = t_1 + \Delta t_2$  and so on, with every time interval  $\Delta t_j$  drawn from the same exponential pdf. The average waiting time is given by the inverse of the total coalescence rate:

$$\overline{\Delta t} = \left[ \int dz \frac{R(z)}{1+z} \frac{dV}{dz} \right]^{-1} \quad (4.18)$$

where  $R(z)$  is the intrinsic merger rate density and  $\frac{dV}{dz}$  is the comoving volume element. We can then write the intrinsic merger rate density as:

$$R(z) = \mathcal{A}_1 \int_{t_{d,min}}^{t(z)} dt_d p(t_d) R_f(z_f), \quad (4.19)$$

where  $\mathcal{A}_1 \leq 1$  is a factor that accounts the fact that not all binaries merge in less than a Hubble time,  $R_f$  is the binary formation rate density,  $z_f$  is the binary formation redshift and

$$t_d = - \int_{z_f}^z d\tilde{z} \frac{1}{(1+\tilde{z})H(\tilde{z})}, \quad (4.20)$$

is the delay time, i.e., the time between the formation and coalescence;  $t_{d,min}$  is the minimum time delay and

$$t(z) = - \int_{\infty}^z d\tilde{z} \frac{1}{(1+\tilde{z})H(\tilde{z})}, \quad (4.21)$$

is the age of the Universe at given redshift  $z$ . Once that the arrival time of the signal has been computed, we can sample the redshift of the source from the observed merger rate pdf, defined as:

$$\mathcal{P}(z) = \frac{R(z)}{1+z} \frac{dV}{dz} \left[ \int dz \frac{R(z)}{1+z} \frac{dV}{dz} \right]^{-1}. \quad (4.22)$$

We then proceed with the second step i.e., by sampling the properties of the dark matter halos that host the mergers. As depicted in their work [80], N. Bellomo *et al.* choose the halo mass  $M_h$  as the characterizing parameter of the host itself. In this framework, the cosmic star formation rate density  $\rho_*$  is the parameter governing the merger rate:

$$\rho_* = \int dM_h \langle SFR(M_h, z) \rangle \frac{dn_h}{dM_h} \quad (4.23)$$

where  $\langle SFR(M_h, z) \rangle$  is the average star formation rate per halo and  $dn_h/dM_h$  is the comoving halo mass function.

Therefore, when running CLASS\_GWB, as first passage the time delay pdf must be sampled, from which the redshift of the binary formation  $z_f$  can be inferred. Then, the host mass at the time of binary formation  $M_h(z_f)$  can be established by sampling the pdf  $p(M_h, z_f) \propto \langle SFR(M_h, z) \rangle \frac{dn_h}{dM_h}$ . Finally, by considering the average growth of dark matter halos across cosmic time, the mass of the host at the time of the merger  $M_h(z)$  can be computed.

The next step is to sample the astrophysical parameters of the source. The parameters that describe the source are:

- Compact object masses ( $m_A, m_B$ ).
- Compact object spins ( $\chi_A, \chi_B$ ).
- Sky localization in the geocentric equatorial coordinate system  $(\alpha, \delta)$ =(right ascension, declination).
- Inclination of the binary total angular momentum with respect the line-of-sight ( $\iota$ ).
- Polarization angle, which quantifies the alignment between the GW frame and those of the detector frame ( $\psi$ ).

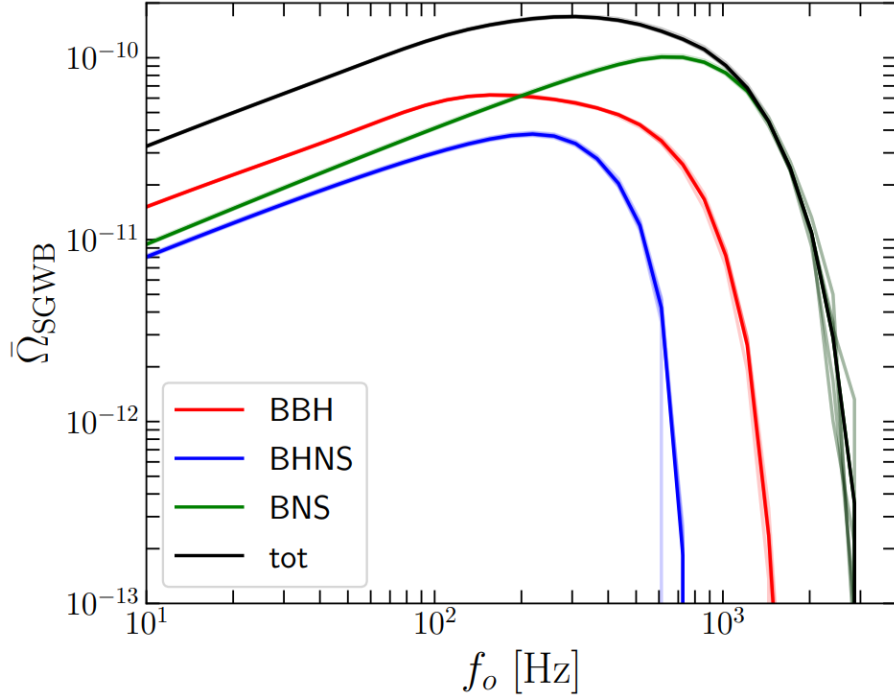


Figure 4.3: Isotropic astrophysical SGWB relative energy density obtained from catalogs of  $10^5$  BBH (in red), BHNS (in blue) and BNS (in green) events using CLASS\_GWB. The black line represents the sum of all these contributions. [80]

With respect to all the quantities, the authors of [80] have decided to work with time-independent and host-independent pdfs.

The second step in the algorithm developed by CLASS\_GWB is the modelling of the detectors and the signal of gravitational waves. Indeed, the detectability of a gravitational wave depends on the relative position of the detector compared to that of the source. The detector coordinates are implemented inside CLASS\_GWB, while all the angles useful to characterize the source are sampled as described above. With an accurate description of the possible orientations, the code can discriminate the detectable sources from those which can not be seen. Once that the source catalog has been created, the waveform of the gravitational waves emitted by each binary system can be computed throughout all the three stages of coalescence: inspiralling, merging and ringdown. The last step to compute the SGWB involves establishing whether or not the single events are detected by the instrument under consideration. By selecting a detector and a threshold for the SNR, CLASS\_GWB discriminates the events between “detected” (if the SNR is greater than the selected threshold, commonly set to 8 for a single observatory and to 12 for a network of detectors) and “undetected”: the first ones would be observed by the detector as resolved events, therefore have to be removed from the catalog providing the SGWB sources. Finally, the stochastic gravitational wave background is computed as the sum over all the unresolved events in the catalog.

Since BNS and BHNS rates are still very uncertain [46], from now on we only consider BBH mergers as the unique contribution of the SGWB from astrophysical compact objects. On top of that, also hyperbolic encounters among COs can contribute to the SGWB. The proper analysis of this contribution is an open topic in the literature (see e.g. [61] [81] [82] [62] for recent works on the topic).

## 4.2 SGWB from early PBH binaries

As we have seen in the previous sections, Primordial Black Holes may be paired in binary systems. Indeed, BH binaries can either form primordially, when two PBHs decouple together from the Hubble flow (Subsection 2.7.1), or later, when two PBHs' trajectories cross sufficiently close to each others so that they become bound (Subsection 2.7.2). Now we will consider the first case, i.e. PBH binaries decoupled primordially.

The gravitational waves emitted by shrinking and merging PBHs' binary systems during the whole history of the Universe may contribute to the stochastic gravitational wave background. In the introduction of this chapter (Eq. 4.8) we saw that three quantities are needed to compute the magnitude of the stochastic gravitational wave background: the probability distribution of the parameters of the source  $p(\theta)$ , the intrinsic merger rate  $R(\theta, z)$  and the gravitational spectral energy emitted in the source frame  $dE_{GW}/df$ .

We can begin by characterizing the intrinsic merger rate of PBH binaries formed in the early Universe. Indeed, considering two PBHs of mass  $m_A$  and  $m_B$ , the intrinsic merger rate of such binaries can be written as [35]:

$$R(m_A, m_B, z) = \frac{1.6 \times 10^6}{\text{Gpc}^3 \text{yr}} f_{PBH}^{\frac{53}{37}} \left( \frac{t(z)}{t_0} \right)^{-\frac{34}{37}} \left( \frac{M}{1M_\odot} \right)^{-\frac{32}{37}} \eta^{-\frac{34}{37}} S[m_A, m_B, f_{PBH}] \quad (4.24)$$

where  $t$  is the time defined in terms of the current age of the Universe  $t_0 \simeq 13.78$  Gyr  $\simeq 43.46 \cdot 10^{16}$  s,  $M = m_A + m_B$  is the total mass,  $\eta = m_A m_B / M^2$  is the symmetric mass ratio of the binary. Finally,  $f_{PBH}$  is the fraction of dark matter in PBH defined in Eq. 2.7, while  $S[m_A, m_B, f_{PBH}] = S = S_1 \times S_2 = (S_{1,A} + S_{1,B}) \times S_2$  is a suppression factor that accounts for the effect of the surrounding inhomogeneities in the dark matter fluid on the binary formation ( $S_{1,A}$ ) and the disruption of the binary by other PBHs. This disruption may be caused by two mechanisms: PBHs close to the initial PBH pair (next near neighbor) may fall into the binary ( $S_{1,B}$ ); moreover, later the PBH binary could be absorbed by a PBH cluster ( $S_2$ ) [36]. Indeed, the gravitational interactions from these external disturbances could alter the orbital parameters of the binary, resulting in its disruption. We can write the first suppression factors as [35]:

$$S_1 = S_{1,A} + S_{1,B} = 1.42 \left[ \frac{\langle m^2 \rangle}{\langle m \rangle^2 (\bar{N}(y) + C)} + \frac{\sigma_M^2}{f_{PBH}^2} \right]^{-\frac{21}{74}} \exp [\bar{N}(y)], \quad (4.25)$$

with  $\langle m \rangle$  the average of the PBH mass distribution and

$$\bar{N}(y) \equiv \frac{M}{\langle m \rangle} \frac{f_{PBH}}{f_{PBH} + \sigma_M}, \quad (4.26)$$

$$C = f_{PBH}^2 \frac{\langle m^2 \rangle}{\sigma_M^2 \langle m \rangle^2} \left\{ \left[ \frac{\Gamma(29/37)}{\sqrt{\pi}} U\left(\frac{21}{74}, \frac{1}{2}, \frac{5f_{PBH}^2}{6\sigma_M^2}\right) \right]^{-\frac{74}{21}} - 1 \right\}^{-1}. \quad (4.27)$$

In the previous equations,  $\sigma_M^2 \simeq 3.6 \cdot 10^{-5}$  is the rescaled variance of the matter density perturbation,  $\Gamma(\cdot)$  is the gamma function and  $U(\cdot, \cdot, \cdot)$  denotes the confluent hypergeometric function, whose integral representation can be written as [83]:

$$U(a, b, z) = \frac{1}{\Gamma(a)} \int_0^\infty e^{-zt} t^{a-1} (1+t)^{b-a-1} dt \quad (4.28)$$

The second suppression factor can be written instead as [35]:

$$S_2 = \min [1, 9.6 \cdot 10^{-3} x^{-0.65} \exp(0.03 \ln^2 x)], \quad (4.29)$$

with

$$x \equiv f_{PBH} \left( \frac{t(z)}{t_0} \right)^{0.44}, \quad (4.30)$$

where the time dependence can be translated in redshift dependence with the following relation, valid for all redshifts [84]:

$$t(z) = \frac{2}{H_0} \frac{1}{1 + (1+z)^2}. \quad (4.31)$$

Now that we have characterized the merger rate, we can see that it depends on only two parameters, i.e. the masses of the PBHs. Thus,  $\theta = \{m_A, m_B\}$  and we are interested only in the probability distribution of the masses  $\Psi(m)$ . As done in most of the recent literature (e.g. [29] [35] [36]), we characterize  $\Psi(m)$  as a log-normal distribution of central mass  $\mu$  and width  $\sigma$ , since this type of function is very flexible:

$$\Psi(m) = \frac{1}{m} \frac{1}{\ln(10)\sqrt{2\pi\sigma^2}} \exp\left(-\frac{\log_{10}^2(\frac{m}{\mu})}{2\sigma^2}\right). \quad (4.32)$$

As we saw in Sec. 2.5, depending on the values of these parameters different PBH formation scenarios can be probed: for big values of  $\sigma$  the mass function is extended, while for small  $\sigma$  the function can be considered as monochromatic.

The last thing to describe is the gravitational spectral energy emitted in the source frame. This is given by the phenomenological expression in the non-spinning limit using the frequency in the source frame  $f_r = f(1+z)$  [85]:

$$\frac{dE_{GW}(m_A, m_B, f_r)}{df_r} = \frac{\pi^{2/3} G^{2/3}}{3} M^{5/3} \eta \mathcal{F}(f_r), \quad (4.33)$$

where

$$\mathcal{F}(f) = \begin{cases} \frac{1}{f^{1/3}} (1 + \alpha_2 f^2)^2 & \text{for } f < f_1 \\ \omega_1 f^{2/3} (1 + \epsilon_1 f + \epsilon_2 f^2)^2 & \text{for } f_1 \leq f < f_2 \\ \omega_2 f^2 \frac{\sigma^4}{[4(f-f_2)^2 + \sigma^2]^2} & \text{for } f_2 \leq f < f_3 \end{cases} \quad (4.34)$$

with  $\alpha_2 = -323/224 + \eta 451/168$ ,  $\epsilon_1 = -1.8897$ ,  $\epsilon_2 = 1.655$  and

$$\omega_1 = \frac{1}{f_1} \frac{[1 + \alpha_2(\pi M f_1)^{2/3}]^2}{[1 + \epsilon_1(\pi M f_1)^{1/3} + \epsilon_2(\pi M f_1)^{2/3}]^2}, \quad (4.35)$$

$$\omega_2 = \frac{\omega_1}{f_2^{4/3}} [1 + \epsilon_1(\pi M f_2)^{1/3} + \epsilon_2(\pi M f_2)^{2/3}]^2, \quad (4.36)$$

$$\pi M f_1 = (1 - 4.455 + 3.521) + 0.6437\eta - 0.05822\eta^2 - 7.092\eta^3, \quad (4.37)$$

$$\pi M f_2 = (1 - 0.63)/2 + 0.1469\eta - 0.0249\eta^2 + 2.325\eta^3, \quad (4.38)$$

$$\pi M f_3 = 0.3236 - 0.1331\eta - 0.2714\eta^2 + 4.922\eta^3, \quad (4.39)$$

$$\pi M \sigma = (1 - 0.63)/4 - 0.4098\eta + 1.829\eta^2 - 2.87\eta^3. \quad (4.40)$$

By collecting and substituting all the terms we just found in either Eq. 4.9 or Eq. 4.8, we are finally able to characterize the SGWB emitted by PBH early binaries. Indeed, we can find that:

$$\Omega_{GW}(f) = \frac{\pi^{2/3} G^{2/3}}{3c^2 \rho_c} f \int dm_A dm_B dz \frac{R(m_A, m_B, z)}{(1+z)H(z)} M^{5/3} \eta \mathcal{F}(f_r) \Psi(m_A) \Psi(m_B). \quad (4.41)$$

### 4.3 SGWB from late PBH binaries

In this section we will analyze PBH binaries formed by gravitational capture in the late Universe; throughout this section we will follow the procedure depicted in the paper of Clesse and García-Bellido [37].

Once bound, two objects in a binary system will shrink their orbit emitting gravitational waves, until they eventually merge, releasing gravitational radiation. The gravitational waves emitted by shrinking and merging PBHs' binary systems formed in late times may thus contribute to the stochastic gravitational wave background.

First of all, we begin the discussion by specifying the initial conditions of the system. As we have seen in the previous section, in order to compute the magnitude of the stochastic gravitational wave background we need to characterize three key quantities: the probability distribution of the parameters of the source, the intrinsic merger rate and the gravitational spectral energy emitted in the source frame. We thus begin making some assumptions on the parameters of the source. We start from an ansatz on the masses of the PBHs: as we have already done in the previous section, we select a log-normal distribution of central mass  $\mu$  and width  $\sigma$  for the mass function. The probability density function  $\Psi(m)$  reads then:

$$\Psi(m) = \frac{1}{m} \frac{1}{\ln(10)\sqrt{2\pi\sigma^2}} \exp\left(-\frac{\log_{10}(\frac{m}{\mu})}{2\sigma^2}\right). \quad (4.42)$$

We then consider  $N$  Primordial Black Holes clustered in virialized galactic sub-halos, with virial velocity  $v_{vir}$ ; some expected virial velocity for PBH clusters could go from  $2 \text{ km s}^{-1}$  to  $200 \text{ km s}^{-1}$ . In the following analysis we take an intermediate value of  $20 \text{ km s}^{-1}$ . Inside those halos, the local dark matter overdensity compared to the cosmological dark matter density  $\rho_{DM}$  is described by the parameter  $\delta_{loc}$ . As reference, values of  $\delta_{loc} \sim 10^9$  are typical of the cold dark matter density in ultra-faint dwarf galaxies and globular clusters [37]. We can thus consider a binary system of eccentricity  $e < 1$  with two PBHs with masses  $m_A$  and  $m_B$  with relative velocity at infinity  $v_0$ . When simulating a binary, we will assume that  $v_0 = v\sqrt{2}$ , where the velocity  $v$  will be sampled from a certain probability density function (pdf)  $P(v)$ . We consider a Maxwell-Boltzmann distribution:

$$P(v) = \frac{1}{v_{vir}^3} \sqrt{\frac{2}{\pi}} \exp\left(-\frac{v^2}{2v_{vir}^2}\right). \quad (4.43)$$

Summarizing, our parameters for PBH late binaries are then  $\theta = \{m_A, m_B, v\}$  with pdfs  $\Psi(m)$  and  $P(v)$ .

The second piece we need to compute for the stochastic gravitational wave background is the gravitational spectral energy released by the binary system and expressed in terms of the frequency in the source frame  $f_r$ . The energy released by a binary with orbit approximated to the Newtonian limit can be written as:

$$\frac{dE_{GW}(m_A, m_B, e)}{df_r} = \frac{\pi^{2/3}}{3} \frac{\mathcal{M}_c^{5/3} G^{2/3}}{f_r^{1/3}} F(e) = \frac{\pi^{2/3}}{3} \frac{\mathcal{M}_c^{5/3} G^{2/3}}{f^{1/3}(1+z)^{1/3}} F(e), \quad (4.44)$$

where  $\mathcal{M}_c$  is the Chirp Mass of the system, defined as  $\mathcal{M}_c^{5/3} = m_A m_B M^{-1/3}$ , with  $M = m_A + m_B$  being the total mass.  $F(e)$  is a function that accounts the effects of the eccentricity that takes the following form:

$$F(e) = (1 - e^2)^{-7/2} \left(1 + \frac{73}{24}e^2 + \frac{37}{96}e^4\right). \quad (4.45)$$

However, as described in [37], the time it takes the system to radiate its angular momentum and to reach  $e \simeq 0$  is less than a single orbit and therefore  $F(e)$  and the effects of eccentricity can be safely neglected when computing the stochastic gravitational wave background. From now on we

will thus consider  $F(e) = 1$ .

We can define the initial separation  $a_0$  between the two black holes as:

$$a_0 = \frac{GM}{v_0^2} \left[ \left( \frac{b}{b_{max}} \right)^{-7} - 1 \right]^{-1} \quad (4.46)$$

with  $b$  being the impact parameter described in Subsection 2.7.2 and  $b_{max}$  the maximum value it can reach to form a binary, which is defined by Eq. 2.30. When simulating a source, we can choose for the impact parameter a uniform distribution between 0 and  $b_{max}$ :

$$P(b) = \begin{cases} \frac{1}{b_{max}} & \text{if } 0 < b < b_{max} \\ 0 & \text{otherwise} \end{cases} \quad (4.47)$$

The formula for the gravitational spectral energy, given in Eq. 4.44, is valid in the range  $f_{min} < f < f_{max}$ . From Kepler's third law, together the fact that GW frequency in a circular binary is twice the orbital frequency [63], we can write the minimum frequency as:

$$f_{min} = \frac{(GM)^{1/2}}{\pi a_0^{3/2}}, \quad (4.48)$$

while the maximum frequency corresponds to the frequency of the innermost stable circular orbit:

$$f_{max} = f_{ISCO} \simeq 4.4 \text{ kHz} \left( \frac{1M_\odot}{M} \right). \quad (4.49)$$

The last ingredient for the characterization of the stochastic gravitational wave background is the intrinsic merger rate  $R(\theta, z) = R(m_A, m_B, v)$ , that here we take as redshift independent, since at first approximation the halo is virialized between  $z = 0$  and  $z = 10$  (i.e. the redshift range we are going to analyze); therefore, we expect that the merger rate remains constant in redshift. However, we could easily extend the formulation in the case of a merger rate with separable functions of time and other parameters:  $R(m_A, m_B, v, z) = t(z) \cdot R(m_A, m_B, v)$ . We can define the number density of a PBH with mass  $m_i$  in a DM halo as

$$n(m_i) = \frac{\rho_{DM,halo}}{m_i} = \frac{\rho_{DM} \cdot \delta_{loc}}{m_i}, \quad (4.50)$$

where  $\rho_{DM,halo}$  is the dark matter density in the halo. We can thus write the merger rate term as:

$$R(m_A, m_B, v) = \tau_{capt}(m_A, m_B, v) \cdot n(m_B) \cdot \frac{f_{PBH}}{\delta_{loc}}, \quad (4.51)$$

where  $\tau_{capt}(m_A, m_B, v)$  is the capture rate, that we can rewrite as:

$$\tau_{capt}(m_A, m_B, v) = n(m_A) \cdot \bar{\sigma}(m_A, m_B, v) \cdot v. \quad (4.52)$$

The term  $\bar{\sigma}(m_A, m_B, v)$  represents the capture cross section of two black holes in dense clusters. Note that this is a completely different term with respect to the width of the log-normal mass distribution referred before as  $\sigma$ . The capture cross section can be rewritten as:

$$\bar{\sigma}(m_A, m_B, v) = \pi \cdot b_{max}^2 = 2\pi \left( \frac{85\pi}{6\sqrt{2}} \right)^{2/7} \frac{G^2 M^{10/7}}{c^4} (m_A m_B)^{2/7} \left( \frac{c}{v_0} \right)^{18/7}, \quad (4.53)$$

where, as previously shown,  $b_{max}$  is the maximal impact parameter. We can now rewrite the explicit expression for the intrinsic merger rate of PBH late binaries, collecting all the different pieces:

$$R(m_A, m_B, v) = \rho_{DM}^2 \delta_{loc} f_{PBH} G^2 \cdot \frac{\pi}{2^{2/7}} \left( \frac{85\pi}{6\sqrt{2}} \right)^{2/7} \frac{M^{10/7}}{(m_A m_B)^{5/7}} \frac{1}{c^{10/7}} \frac{1}{v^{11/7}}. \quad (4.54)$$

Now that we have found all the terms needed, we can substitute all these expressions in either Eq. 4.9 or Eq. 4.8 to characterize the SGWB. The choice is equivalent and for consistency with the results in this thesis, we will use the first one. The total merger rate is given by one half the integral of  $R$  over the whole mass range; this is to take into consideration the fact that  $R(m_A, m_B, v) = R(m_B, m_A, v)$ . Thus, recalling that  $\theta = \{m_A, m_B, v\}$  we can finally write:

$$\Omega_{GW}(f) = \frac{f}{c^2} \frac{1}{2} \int dm_A \Psi(m_A) \int dm_B \Psi(m_B) \int dv P(v) \int dz \frac{R(m_A, m_B, v)}{(1+z)H(z)} \frac{\pi^{2/3}}{3} \frac{\mathcal{M}_c^{5/3} G^{2/3}}{f^{1/3}(1+z)^{1/3}} = \quad (4.55)$$

$$= \frac{1}{6} \frac{(G\pi)^{2/3}}{\rho_{c,0} c^2} f^{2/3} \int dz \frac{1}{(1+z)^{4/3} H(z)} \iiint dm_A dm_B dv R(m_A, m_B, v) \mathcal{M}_c^{5/3} \Psi(m_A) \Psi(m_B) P(v) \quad (4.56)$$



# Chapter 5

## Original results

As we saw in Subsection 4.1.1, CLASS\_GWB [80] is a robust numerical method to compute the Stochastic Gravitational Wave Background (SGWB) from astrophysical sources. However, since the aim of this thesis is to characterize the SGWB from PBH mergers, a modification of the CLASS\_GWB code has been implemented.

### 5.1 Modification of CLASS\_GWB

The first passage, as in the original version of CLASS\_GWB, consists of selecting the category of events: for the modified version, the new category is “PBH”. The second passage requires the sampling of time intervals between two consecutive events. This can be done using the same exponential probability function exploited for the astrophysical SGWB (Eq. 4.17). Also the expression for the average waiting time remains the same (Eq. 4.18), but now the intrinsic merger rate density has to be computed using the results seen in Sec. 4.3 and Sec. 4.2. Indeed, two possible intrinsic merger rate density can be used, depending on the time formation of the PBH binary:

- When computing the SGWB from binaries formed in the early Universe we use the merger rate as written in Eq. 4.24.
- When computing the SGWB from binaries formed in the late Universe we use the merger rate as written in Eq. 4.52

As we have seen in Chapter 4, those merger rates depend in turn on some parameters  $\theta$ : in the case of early PBH binaries  $\theta = m_A, m_B$ , while for late gravitational capture  $\theta = m_A, m_B, v_{PBH}$ . Since the merger rates are separable functions of redshift and of other parameters, we can write that  $R(z, \theta) = R_1(z) \cdot R_2(\theta)$ . To get rid of the parameter dependence, first we sample the parameters  $\theta$  from their respective distributions, and then we average the merger rate over some large realization ( $N$ ) of them. Therefore, we can write the mean intrinsic merger rate  $\bar{R}(z)$  as:

$$\bar{R}(z) = R_1(z) \cdot \frac{1}{N} \sum_i R_{2,i}(\theta_i) \quad (5.1)$$

where the subscript  $i$  goes from 1 to  $N$ . With this mean intrinsic merger rate density now we are able to sample the time intervals. The next step is to sample the redshift of the source from Eq. 4.22 using the mean intrinsic merger rate density just described. Also, it is not necessary to sample the properties of the host as in the original version of CLASS\_GWB, since the merger rate does not depend on those properties. We can proceed directly by sampling the various astrophysical parameters of the source, which are the same as the ones generated for the astrophysical SGWB ( $m_A, m_B, \chi_A, \chi_B, \alpha, \delta, \iota, \psi$ ). The new schematic approach can be seen in Fig. 5.1, where the only difference from the previous version of CLASS\_GWB is the fact that the host part is now bypassed as not necessary. The remaining passages to compute the SGWB are the same as for the original version of CLASS\_GWB.

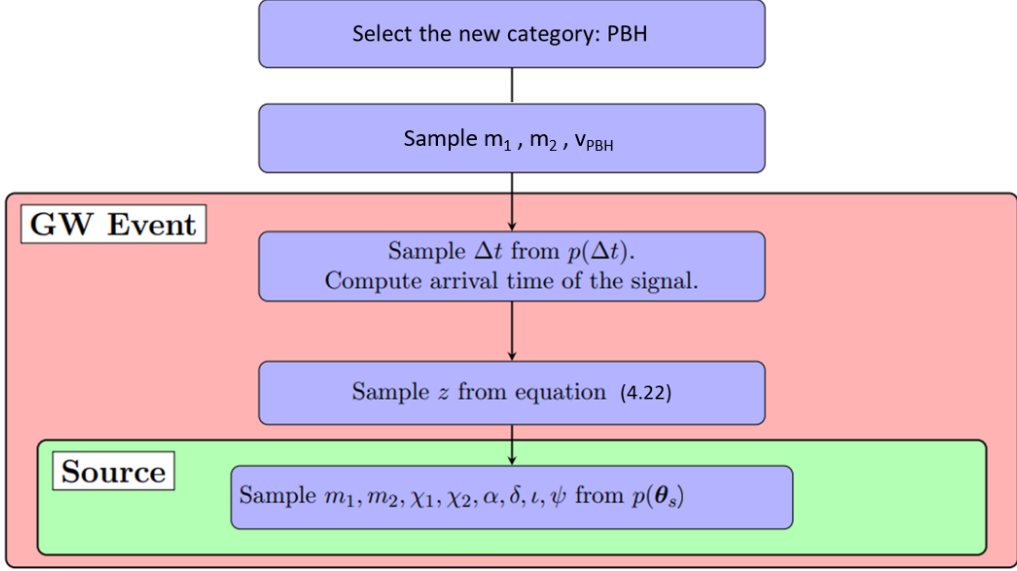


Figure 5.1: New scheme of CLASS\_GWB adapted for Primordial Black Holes. The image has been taken from [80] and modified to describe the new approach used in this thesis.

## 5.2 Initial parameters' setup

To compute the average intrinsic merger rate and to generate the GW catalog we need to sample the astrophysical properties of the GW events. The probability density functions of the parameters are selected as follows:

- Compact object masses ( $m_A, m_B$ ): As we saw in Sec. 2.4, usually a log-normal distribution (Eq. 2.10) is used, with mean mass  $\mu$  and width  $\sigma$ . However, other different choices are possible. To probe different scenarios, in this thesis we exploited five different mass functions, as explained in the following two sections. At the beginning of each of them we will clarify what are the mass prescriptions for that section.
- Velocities ( $v_{PBH}$ ): The sampling of the velocity will be useful only in the case of PBH binaries formed in the late Universe. For those binaries, a Maxwell-Boltzmann probability distribution function (Eq. 4.43) has been selected, completely characterized by the virial velocity, here set to  $v_{vir} = 20 \text{ km s}^{-1}$ . This can be seen in Figure 5.3.
- Compact object spins ( $\chi_A, \chi_B$ ): As we saw in Sec. 2.4, Primordial Black Holes are expected to have negligible spins. Therefore, a monochromatic distribution of  $\chi_i = 0$  has been selected.
- Sky localization ( $\alpha, \delta$ ): As in the original version of CLASS\_GWB, we will assume that the right ascension  $\alpha$  and the sine of declination  $\sin \delta$  are drawn from a uniform probability distribution function. This can be seen in Figure 5.2.
- Inclination ( $\iota$ ): As in the original version of CLASS\_GWB, we will assume that the cosine of the inclination  $\cos \iota$  is drawn from a uniform probability distribution function. This can be seen in Figure 5.2.
- Polarization angle ( $\psi$ ): As in the original version of CLASS\_GWB, we will assume that the polarization angle  $\psi$  is drawn from a uniform probability distribution function. This can be seen in Figure 5.2.

By specifying the various PBHs' mass functions we want to probe, we can compute the stochastic gravitational wave background as described for CLASS\_GWB.

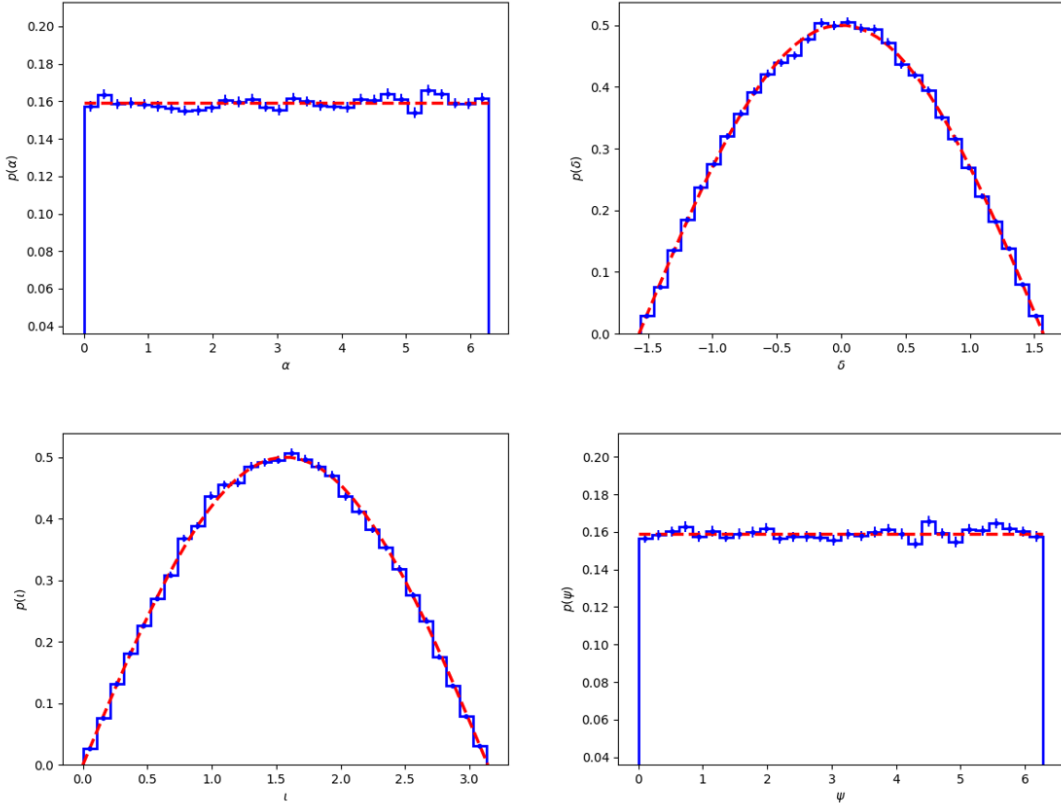


Figure 5.2: Probability density functions of the parameters common for all the sources, namely astrophysical BHs, early PBH and late PBH binaries. In the top left and right panels, respectively the right ascension  $\alpha$  and the declination  $\delta$  are depicted. The bottom left panel represents the inclination  $i$ , while the bottom right panel shows the polarization angle  $\psi$ . The red lines are the theoretical distributions, while the blue histograms collect the events we generate for the catalog. This plot has been made with CLASS\_GWB.

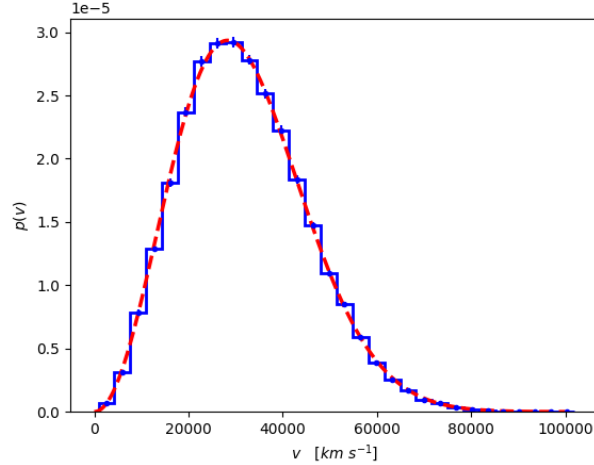


Figure 5.3: Probability density function of the velocities of PBHs inside halos with virial velocity  $v_{vir} = 20 \text{ km s}^{-1}$ . The red line is the theoretical distribution, while the blue histogram collects the events we generate for the catalog. This plot has been made with CLASS\_GWB.

### 5.3 General considerations

To begin with, an important aspect should be clarified: this modification of CLASS\_GWB allows the user to compute the SGWB for both early PBH binaries and late PBH binaries. In the code, they are treated separately and one source can be analysed independently of the other. However, in principle the two formation mechanisms are related. Indeed, if a significant amount of PBHs decoupled from the Hubble flow and formed a binary in the early Universe, the fraction of PBHs in the late Universe would be affected by it: greater the fraction of PBHs decoupled in the early Universe, smaller the fraction of PBHs available to form binaries by gravitational interaction. This holds only in principle, since some recent works [86] [87] showed how the fraction of binaries decoupled in the early Universe is very tiny, of the order of  $\mathcal{O}(0.01f_{PBH}^{16/37})$ : even for  $f_{PBH} = 1$  the formation of binaries in the early Universe is a subdominant process. Therefore, in the analysis of the SGWB we consider two independent population of PBH binaries that in principle could coexist.

We simulate a total of  $N = 10^5$  events per catalog. When simulating the sources of the SGWB, we noted that the final signal would spread more for the early binaries than for the late ones. This is reasonably imputable to the more complex dependencies the merger rate of early binaries has on the source parameters. To obviate the problem and to get a more reliable final estimate for the signal, 10 catalogs of late binaries and 20 catalogs of early binaries have been simulated. Subsequently, the final signal for each of the two PBHs' binary populations has been averaged between the realization of the same category. Consequently, the mean signal reported in every figure could have some sharp feature; this is due to the average between the realization and it has not strong physical meaning. Moreover, we point out that the local value of the merger rate for early binaries is still really uncertain. In Section 4.2, and particularly in Eq. 4.24, we described the state of the art for what concerns its analysis; however, some recent works (e.g. [88] and references therein) pointed out how this merger rate could be overestimated by a factor of  $10^2$ . As a reference to discuss this issue and for only a mass distribution (i.e. the monochromatic mass function peaked at  $\mu = 30M_\odot$ ), we compute also the SGWB for the merger rate in Eq. 4.24 divided by  $10^2$ .

As reference for a possible detection of the stochastic gravitational wave background, the Einstein Telescope detector has been selected (see section 3.3.4). The dimensionless energy density in GWs  $\Omega_{GW}$  is related to the detector noise one-sided power spectral density  $S_n$  described in [89] as described in [69]:

$$\Omega_{GW}(f) \sim \frac{8}{9} \frac{2\pi^2 f^3}{3H_0^2} S_n(f), \quad (5.2)$$

where  $f$  is the observed frequency and the 8/9 factor descend from the signal-to-noise ratio (SNR) computation related with the particular shape of ET considered (see [90] for details). However, as [91] describes, the SGWB is observed over frequency bins  $\Delta f$ : this improves the SNR, since the signal has to be integrated over  $f$ . To account for this, we follow the indications of [91] and we further divide by 10 the curve obtained in Eq. 5.2. We note that with this prescription and the mass functions proposed in the original version of CLASS\_GWB, the stochastic gravitational wave background from Astrophysical Black Holes should be almost undetectable. This depends on both the astrophysical assumptions on the masses and the uncertainties in the detector network and should be taken carefully: as can be seen in other works [75] [78], changing prescriptions lead to a possible detection of the astrophysical black hole background. Moreover, other CO binaries should be taken into account and could increase the signal of the background [80].

## 5.4 Monochromatic mass function

For monochromatic mass functions, the current constraints on PBH abundance are those depicted in Sec. 2.5 and particularly in Figure 2.3 and Figure 2.4. In this section, we will analyze the stochastic gravitational wave background resulting from three different monochromatic mass functions in which PBHs could still provide a non-negligible fraction of dark matter ( $f_{PBH} \sim 0.1$ ):

- $M_{PBH} = 30 M_\odot$ ,
- $M_{PBH} = 0.1 M_\odot$ ,
- $M_{PBH} = 10^{-5} M_\odot$ .

More than the ones we take under consideration, there is another important window in which PBHs could still provide the totality of dark matter, namely the  $10^{-16} M_\odot < M_{PBH} < 10^{-11} M_\odot$  mass window. However, if we use Eq. 2.1 to compute the Schwarzschild radius of such PBHs, we can see how  $R_S \sim 1.5 \times 10^{-13} - 1.5 \times 10^{-8}$  m. For such small values of the Schwarzschild radius, we expect the physics to be different (namely, quantum-gravity effects could arise), and thus a detailed analysis, which goes beyond the scope of this work, would be needed. Moreover, as we are going to see in the following subsections, lower the values of the masses selected, higher in frequency the peak would be. Even for frequencies correspondent to  $M = 0.1 M_\odot$  it would be challenging to create experiments sensitive enough to detect those (possible) signals, even if some proposals can already be found in the literature (see e.g. [92, 93] and references therein). For  $M_{PBH} < 10^{-11} M_\odot$  the signal, if present, would have frequencies so high that it would not be testable by any (current or planned) detectors. Lastly, for such small masses the numerical implementation would be much more complex than the one presented here. Therefore, the proper investigation of this mass windows has been left for future studies.

### 5.4.1 $M_{PBH} = 30 M_\odot$

One interesting mass window to test is the one between  $10^{-2} M_\odot < M_{PBH} < 10^2 M_\odot$ . To compare it to stellar mass black holes seen by LIGO-Virgo, we can select a monochromatic mass function peaked at  $M_{PBH} = 30 M_\odot$ . To compute the stochastic gravitational wave background with the modified version of CLASS\_GWB, we need to specify the mass function. In this analysis, we choose a very sharp ( $\sigma = 0.01$ ) log-normal mass distribution (Eq. 2.10) peaked at  $\mu = 30 M_\odot$ . The mass distribution as sampled with the new version of the code is represented in the bottom left panel of Figure 5.4 and Figure 5.5. We then consider both an early population of PBH binaries and a late one. For both of them, we display the redshift probability distribution function of a merger event and the merger rate of the population respectively in the top right and bottom right panels of Figure 5.4 (for early PBH binaries) and of Figure 5.5 (for late PBH binaries). We compute for the two populations also the time interval between two subsequent signals, which can be seen in the top left panels in Figure 5.4 for early PBH binaries and in Figure 5.5 for late PBH binaries. We can see that all the parameters follow very well the theoretical distributions. Once the parameters have been sampled, we can compute the stochastic gravitational wave background for both early and late PBH binaries, using the prescriptions underlined in Sec. 5.3. The result can be seen in Figure 5.6, where as a reference also the signal from astrophysical BBHs has been reported. We remind that, only for this case, we computed the SGWB for early PBH binaries with both the merger rate as in Eq. 4.24 and a merger rate divided artificially by  $10^2$ , to take into account the uncertainties in the derivation of Eq. 4.24. We can see how, in the best case scenario (Eq. 4.24), the stochastic gravitational wave background from early PBH binaries could be detected by the Einstein Telescope. On the other hand, if the merger rate of Eq. 4.24 will actually turn to be a great overestimation, then the SGWB from these sources could fall even below the SGWB from late PBH binaries. However, from now on, we take Eq. 4.24 as the more reliable estimate for the merger rate of early PBH binaries. If this is the case, we can see clearly that the total SGWB will be dominated by the signal of early PBH binaries. This is due to both the local merger rate, higher than the other two, and the general shape of the merger rate, which grows in redshift.

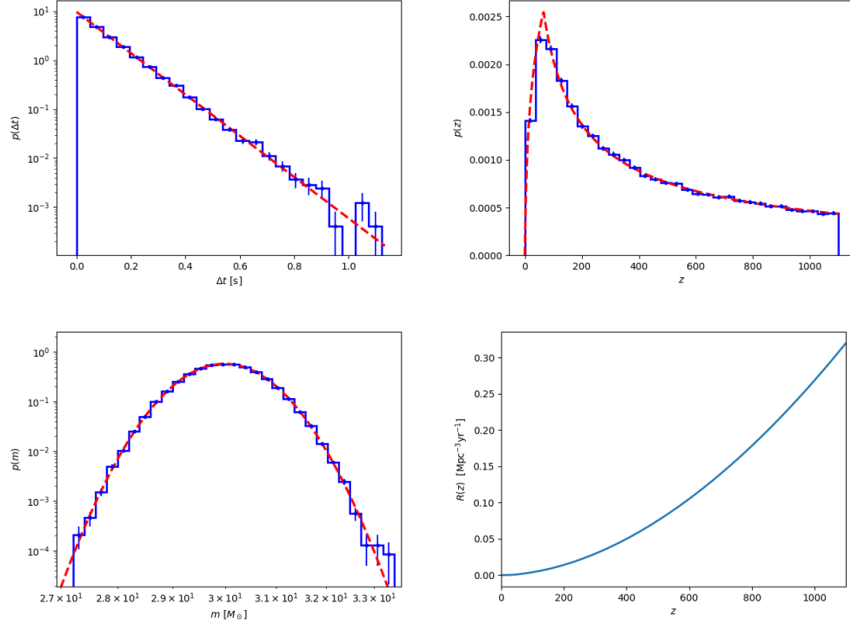


Figure 5.4: Parameters sampled for a monochromatic mass function of early binaries of  $30M_{\odot}$  PBHs. In the top left panel the distribution of time intervals is depicted. The top right panel represents the redshift probability distribution function, while the bottom left panel shows the mass function. Lastly, in the bottom right panel the merger rate as a function of redshift is depicted. The red lines are the theoretical distributions, while the blue histograms collect the events we sample for the catalog.

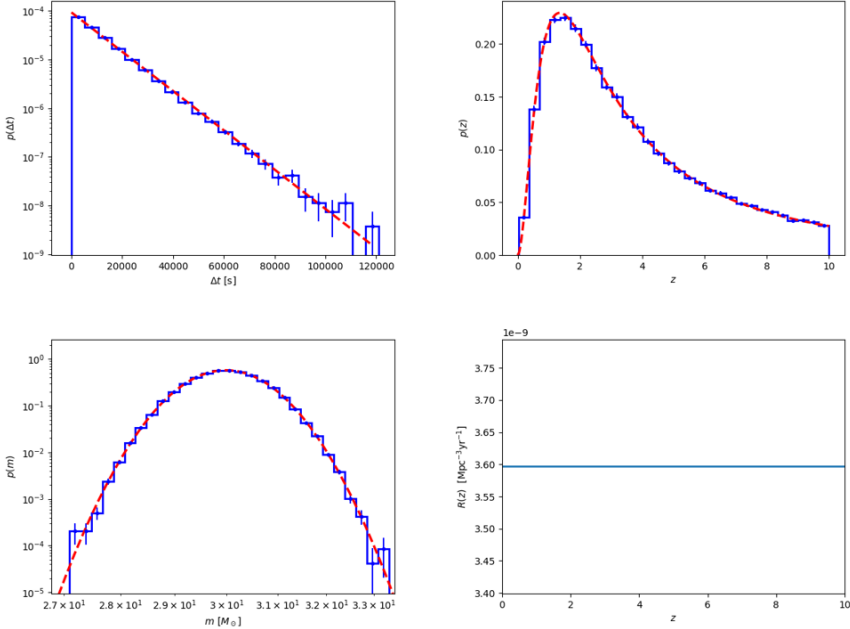


Figure 5.5: Parameters sampled for a monochromatic mass function of late binaries of  $30M_{\odot}$  PBHs. In the top left panel the distribution of time intervals is depicted. The top right panel represents the redshift probability distribution function, while the bottom left panel shows the mass function. Lastly, in the bottom right panel the merger rate as a function of redshift is depicted. The red lines are the theoretical distributions, while the blue histograms collect the events we sample for the catalog.

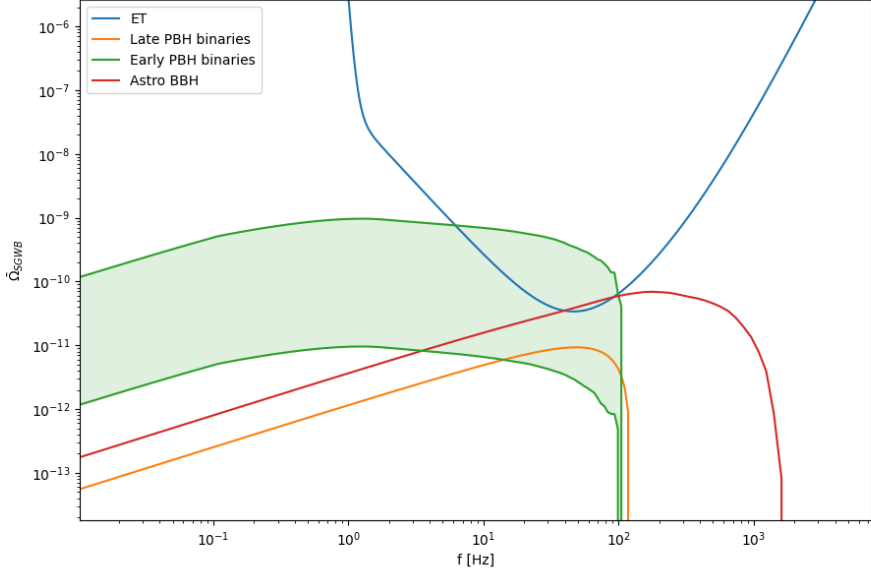


Figure 5.6: Stochastic gravitational wave background as a function of frequency computed for various sources. The three sources of the stochastic background reported are astrophysical black holes (in red), early PBH binaries (in green, for the two different values of the merger rate) and late PBH binaries (in orange). The SGWB from PBHs has been computed for a monochromatic mass distribution of  $30M_{\odot}$ . The minimum signal detectable through Einstein Telescope (ET) is depicted in blue.

#### 5.4.2 $M_{PBH} = 0.1 M_{\odot}$

It is interesting to test also the lower part of the mass window described in the previous subsection ( $10^{-2} M_{\odot} < M_{PBH} < 10^2 M_{\odot}$ ): we can analyze a monochromatic mass function peaked at  $M_{PBH} = 0.1 M_{\odot}$ , since some models (e.g. [94]) predict PBHs peaked in the sub-solar mass range. We then choose a very sharp ( $\sigma = 0.01$ ) log-normal mass distribution (Eq. 2.10) peaked at  $\mu = 0.1 M_{\odot}$ . We proceed by sampling the parameters in the exact same way as before. The parameters are reported in Appendix 6 in Figure A.1 for early PBH binaries and in Figure A.2 for late PBH binaries. From these parameters, the SGWB has been computed as before. The result can be seen in Figure 5.7, where again we take as a reference the signal from astrophysical BBHs. We can see how, the situation has changed: since now we are considering smaller masses compared to those analyzed in the previous subsection, the signal frequency peak has changed too, shifting to higher values. We can see from Figure 5.7 that the low frequency tail of the stochastic gravitational wave background signal from early binaries could be seen by ET. Moreover, it is expected to dominate over the other two (i.e. astrophysical BHs and late PBH binaries). This is ascribable to the higher local merger rate of early PBH binaries compared to the merger rate of the other two. Moreover, the merger rate of early PBH binaries increases greatly in redshift, contributing to an increment of the total signal.

#### 5.4.3 $M_{PBH} = 10^{-5} M_{\odot}$

The last mass window to test is the one between  $10^{-7} M_{\odot} < M_{PBH} < 10^{-4} M_{\odot}$ . Therefore, we can analyze a monochromatic mass function peaked at  $M_{PBH} = 10^{-5} M_{\odot}$ . In this subsection, we then choose a very sharp ( $\sigma = 0.01$ ) log-normal mass distribution (Eq. 2.10) peaked at  $\mu = 10^{-5} M_{\odot}$ . Also for this case, all the parameters have been sampled and are reported in Appendix 6 in Figure A.3 for early PBH binaries and in Figure A.4 for late PBH binaries. We note that if for the population of late binaries the sampled time intervals follow very well the theoretical distribution, this is not the case for the early ones: indeed, the very small mass of the PBHs together with the

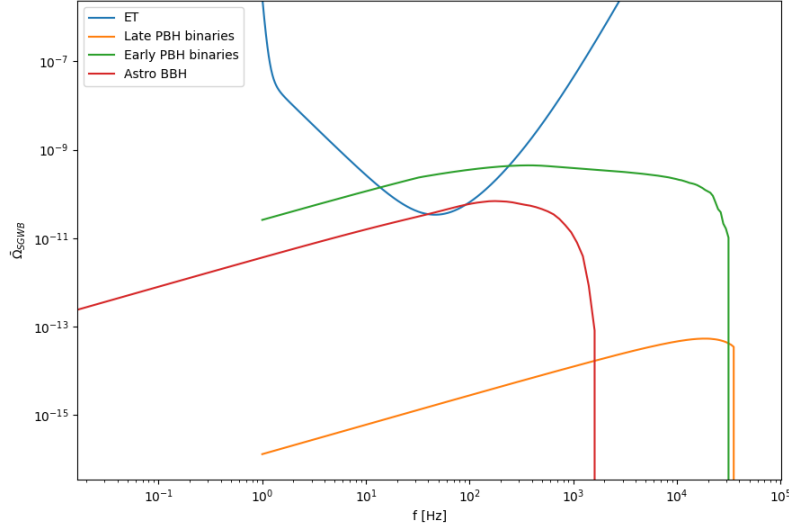


Figure 5.7: Stochastic gravitational wave background as a function of frequency. The three sources of the stochastic background reported are astrophysical black holes (red), early PBH binaries (green) and late PBH binaries (orange). The SGWB from PBHs has been computed for a monochromatic mass distribution of  $0.1M_{\odot}$ . The minimum signal detectable through Einstein Telescope (ET) is depicted in blue.

extremely high merger rate determine a nearly continuous signal, with a consequently Dirac delta in the distribution of time intervals. From these parameters, the SGWB has been computed as before. The result is reported in Figure 5.8. We can see how the SGWB from both early and late PBH binaries can not be seen by the Einstein Telescope. This is not because of the amplitude of the SGWB, but because of its frequency range. Indeed, even if the amplitude of such a SGWB could be comparable to that of astrophysical BHs, the frequency range for a possible detection is shifted to higher values. This is because the extremely small masses we are considering: the higher the masses, the higher the frequency peak. Moreover, we can note that the SGWB from early PBH binaries is expected to dominate over the one from late binaries due to the extremely high merger rate throughout the whole Universe history, which leads a nearly continuous signal.

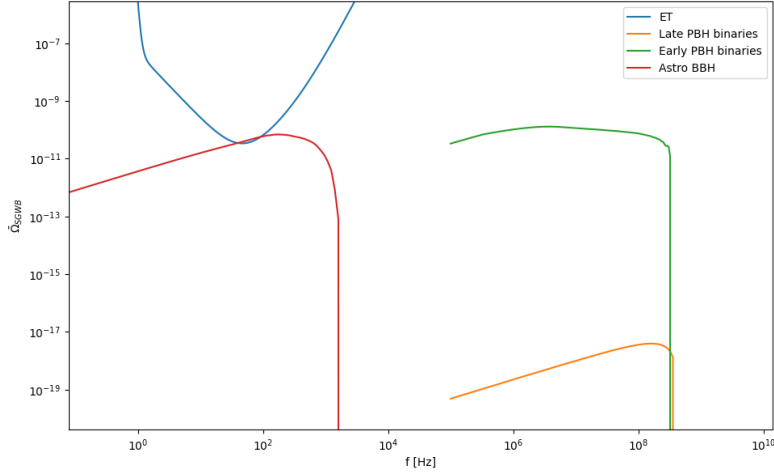


Figure 5.8: Stochastic gravitational wave background as a function of frequency. The three sources of the stochastic background reported are astrophysical black holes (red), early PBH binaries (green) and late PBH binaries (orange). The SGWB from PBHs has been computed for a monochromatic mass distribution of  $10^{-5} M_\odot$ . The minimum signal detectable through Einstein Telescope (ET) is depicted in blue.

## 5.5 Extended mass function

For extended mass functions, the current constraints on PBH abundance depicted in Sec. 2.5 and particularly in Figure 2.3 and Figure 2.4 are no longer valid. Indeed, those constraints were computed for monochromatic mass functions and must be redetermined for extended mass functions. This has been done in [95], where the authors select two extended mass functions as a reference: an extended log-normal mass distribution and an extended power-law distribution. They compute the maximum PBH abundance  $f_{PBH}$  for these distributions as a function of their parameters. Depending on the parameters that characterize the distributions, the maximum PBH abundance changes. In this section we explore two PBH mass functions for which they could still provide the totality of dark matter ( $f_{PBH} \sim 1$ ):

- An extended ( $\sigma = 0.1$ ) log-normal (Eq. 2.10) mass distribution peaked at  $\mu = 35M_\odot$ .
- An extended power-law distribution of the form:

$$\Psi(m) = \frac{\mathcal{N}_{PL}}{m^{1-\gamma}} \Theta(m - M_{min}) \Theta(M_{max} - m), \quad (5.3)$$

characterized by an exponent  $\gamma$ , a mass range ( $M_{min} = 28M_\odot, M_{max} = 40M_\odot$ ) and a normalization factor  $\mathcal{N}_{PL}$  that reads:

$$\mathcal{N}_{PL} = \begin{cases} \frac{\gamma}{M_{max}^\gamma - M_{min}^\gamma} & \text{if } \gamma \neq 0 \\ \log^{-1}\left(\frac{M_{max}}{M_{min}}\right) & \text{if } \gamma = 0 \end{cases}. \quad (5.4)$$

The exponent  $\gamma$  is related to the equation of state parameter  $w$  of the Universe when PBHs are formed through the following relation:

$$\gamma = -\frac{2w}{1+w}. \quad (5.5)$$

For Primordial Black Holes formed during the radiation dominated epoch ( $w = 1/3$ ) then  $\gamma = -0.5$ .

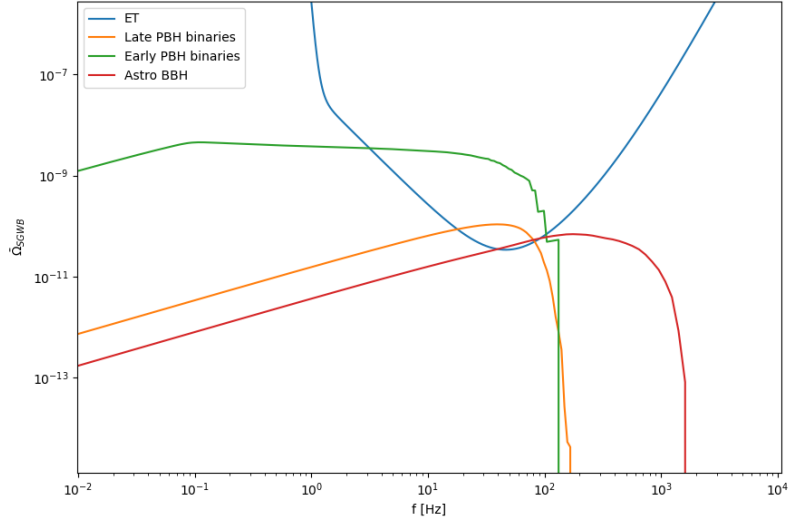


Figure 5.9: Stochastic gravitational wave background as a function of frequency computed for various sources. The three sources of the stochastic background reported are astrophysical black holes (in red), early PBH binaries (in green) and late PBH binaries (in orange). The SGWB from PBHs has been computed for an extended log-normal mass distribution of  $35 M_{\odot}$  PBH. The minimum signal detectable through Einstein Telescope (ET) is depicted in blue. We remind that the sharp shape of the curve that can be seen for the early population of PBH binaries is due to the average over the total of realization and it is then only a numerical artefact.

### 5.5.1 Log-normal mass function

We now consider the first extended mass distribution, the broad ( $\sigma = 0.1$ ) log-normal mass distribution (Eq. 2.10) peaked at  $\mu = 35 M_{\odot}$ . The parameters are sampled as the previous cases and are reported in Figure A.5 for early PBH binaries and in Figure A.6 for late PBH binaries. The result of the computation of the stochastic gravitational wave background can be seen in Figure 5.9. We can see that for the case under exam, the stochastic gravitational wave background from early PBH binaries dominate over the other components and it could be seen by the Einstein Telescope. Most importantly, we note that also the contribution from late PBH binaries, which is less uncertain, exceeds the signal from astrophysical BHs and could be seen by ET.

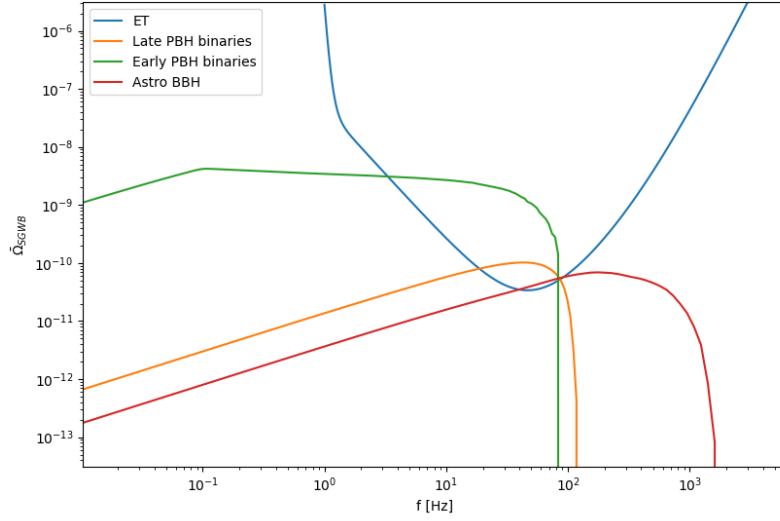


Figure 5.10: Stochastic gravitational wave background as a function of frequency computed for various sources. The three sources of the stochastic background reported are astrophysical black holes (in red), early PBH binaries (in green) and late PBH binaries (in orange). The SGWB from PBHs has been computed for an extended power-law mass function of  $28M_{\odot} < M_{PBH} < 40M_{\odot}$  PBHs. The minimum signal detectable through Einstein Telescope (ET) is depicted in blue.

### 5.5.2 Power law mass function

We can finally proceed by considering the second extended mass distribution. We choose the power-law mass distribution as presented in Eq. 5.4. All the parameters needed for the computation of the SGWB are reported in Figure A.7 for early PBH binaries and in Figure A.8 for late PBH binaries. The SGWB resulting from this analysis can be seen in Figure 5.10. We can see that this case is very similar to the previous one: the SGWB from early binaries is expected to dominate the signal and to be detected by ET in the best case scenario. Even if this is not the case, the SGWB from late binaries could still be detected.

## 5.6 Future prospects

The detection of the stochastic gravitational wave background is the aim of most of GW detectors planned for the next years. As we have seen, the SGWB from PBH binaries could dominate the other contributions and it could be seen by the Einstein Telescope. Therefore, the future target for ET is the detection of the total SGWB and possibly the disentanglement of its components; eventually, we could be able to discriminate also between models of PBHs. If the SGWB from Primordial Black Holes will be observed, it will be a major breakthrough in both Astrophysics and Cosmology.

On top of that, we have seen how very light Primordial Black Holes, if present, will generate a signal in the high frequency range. Gravitational waves of so high frequency have more recently garnered renewed interest: a number of intriguing proposals and operating detectors for high-frequency GW detection already exist, including interferometers, microwave, optical cavities and many others [92, 93]. In the future it could be possible to probe also that high frequency regime. Other mass windows, such as high mass PBHs, could also be relevant if extended mass functions are taken into account.

Finally, all the treatment we have done in this Master thesis could be refined, mainly with respect to the modelling of the binary merger rates. As we discussed, this is a major issue for early PBH binaries, but also the case of astrophysical black holes implies a lot of uncertainties, mainly related with the astrophysical processes. Moreover, even if it is expected to be subdominant, the SGWB should be estimated also for hyperbolic encounters among Primordial Black Holes in order to develop a fully self-consistent analysis.

# Chapter 6

## Conclusions

Before gravitational waves, astronomers and astrophysicists had to rely just on the information given by electro-magnetic radiation coming from the Universe. Now that the gravitational wave era has begun, scientists have a completely new insight of the Universe. Indeed, we can now receive information also from dark objects that could not be detected otherwise, while also exploiting complementary information between the gravitational sector and the electro-magnetic one. This is a powerful and useful tool to probe a plethora of theories, gaining physical information in many fields. Gravitational-wave Astronomy has just begun and it will surely make significant progress in the coming years.

“I think over the coming decades we will see enormous numbers of things. Just as electro-magnetic astronomy was begun in essence by Galileo pointing his telescope in the sky and discovering Jupiter’s moons. This is the same thing but for gravitational waves . . .”

Kip S. Thorne [96]

Cosmological studies can gain from gravitational waves under many different perspectives: for example, GWs could probe the inflation or even the Big Bang itself. Moreover, GW surveys can be used to trace the Large Scale Structures, providing insights on the structure and evolution of the Universe at late times. The work we realized in this Master thesis place itself in this context. Focusing on the stochastic gravitational wave background that primordial black hole binaries could possibly generate, we provided a new way to place interesting constraints on the existence of such sources and the possibility they are part of the dark matter content in the Universe, which nature is still unknown.

We assess the contribution from early and late Primordial Black Hole binaries, describing the models under which they can be estimated and underlying the main limitations and uncertainties these have: from the experimental point of view, new generation detectors spanning large frequency range should be built; from the theoretical side, many refinements should be considered. We saw how Primordial Black Holes could play a major role in the signal of the stochastic gravitational wave background, possibly dominating its entirety. Depending on the observed frequencies, the SGWB could be used to probe different PBH scenarios.

Our analysis was based on forecasts dedicated to the next generation of GW detectors, which will become available in the next decade. If the existence of a SGWB from PBH will be confirmed, it would be a revolution in our understanding of the Universe.



## **Appendix A**

### **Plots**

This appendix collects the sample plots, which were not reported in Chapter 5 for seek of neatness.

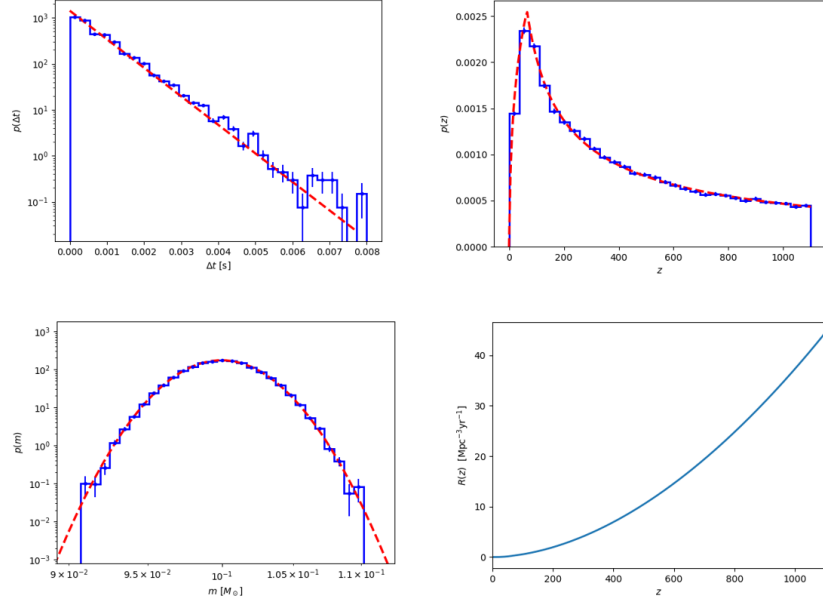


Figure A.1: Parameters sampled for a monochromatic mass function of early binaries of  $0.1 M_\odot$  PBHs. In the top left panel the distribution of time intervals is depicted. The top right panel represents the redshift probability distribution function, while the bottom left panel shows the mass function. Lastly, in the bottom right panel the merger rate as a function of redshift is depicted. The red lines are the theoretical distributions, while the blue histograms collect the events we sample for the catalog.

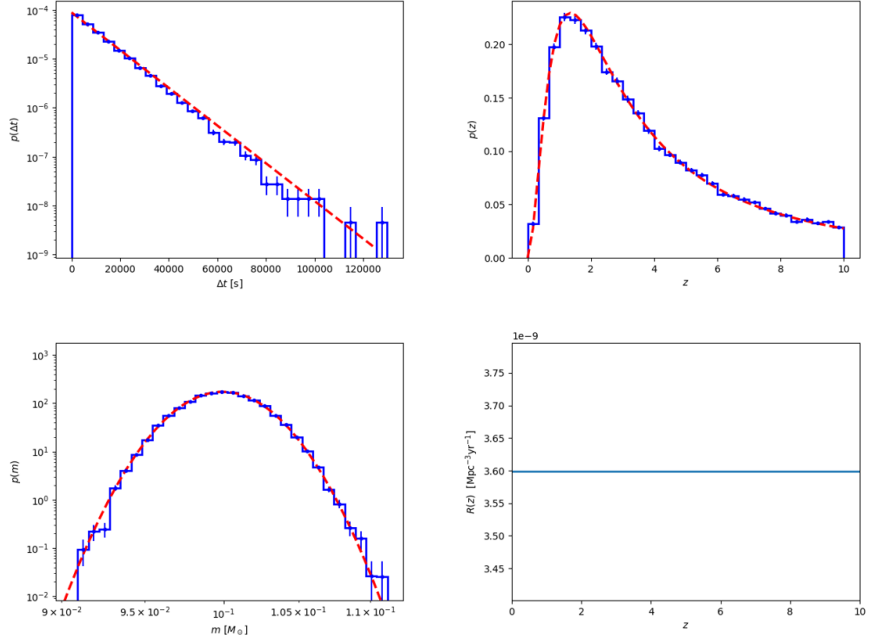


Figure A.2: Parameters sampled for a monochromatic mass function of late binaries of  $0.1 M_\odot$  PBHs. In the top left panel the distribution of time intervals is depicted. The top right panel represents the redshift probability distribution function, while the bottom left panel shows the mass function. Lastly, in the bottom right panel the merger rate as a function of redshift is depicted. The red lines are the theoretical distributions, while the blue histograms collect the events we sample for the catalog.

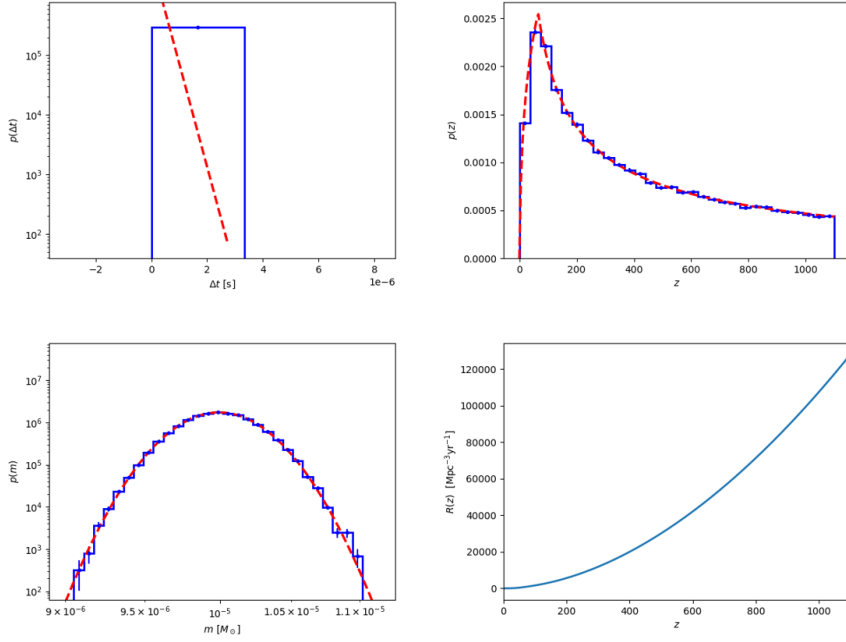


Figure A.3: Parameters sampled for a monochromatic mass function of early binaries of  $10^{-5} M_{\odot}$  PBHs. In the top left panel the distribution of time intervals is depicted. The top right panel represents the redshift probability distribution function, while the bottom left panel shows the mass function. Lastly, in the bottom right panel the merger rate as a function of redshift is depicted. The red lines are the theoretical distributions, while the blue histograms collect the events we sample for the catalog. We note that, as explained in the relative subsection, the time intervals sampled are so small that they create a Dirac delta and the signal can be considered as continuous.

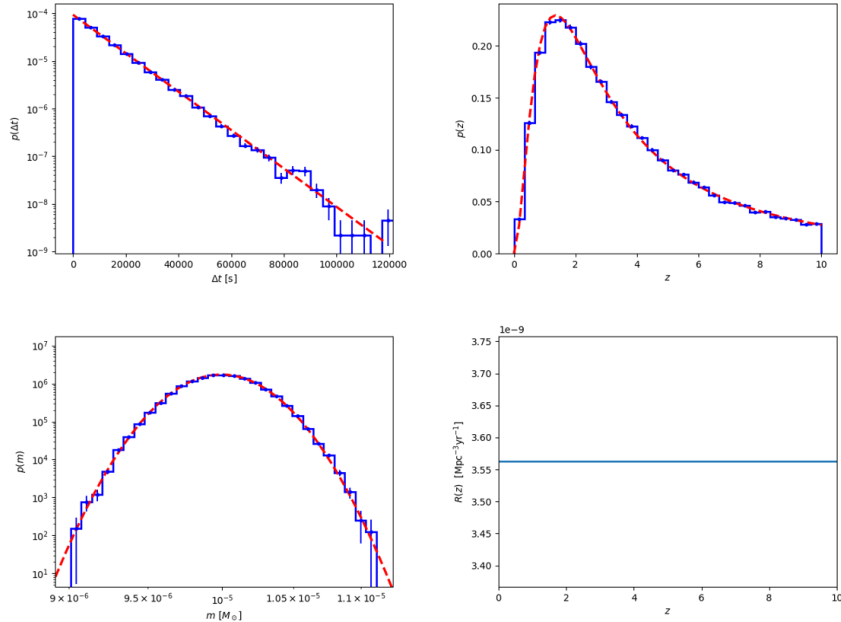


Figure A.4: Parameters sampled for a monochromatic mass function of late binaries of  $10^{-5} M_{\odot}$  PBHs. In the top left panel the distribution of time intervals is depicted. The top right panel represents the redshift probability distribution function, while the bottom left panel shows the mass function. Lastly, in the bottom right panel the merger rate as a function of redshift is depicted. The red lines are the theoretical distributions, while the blue histograms collect the events we sample for the catalog.

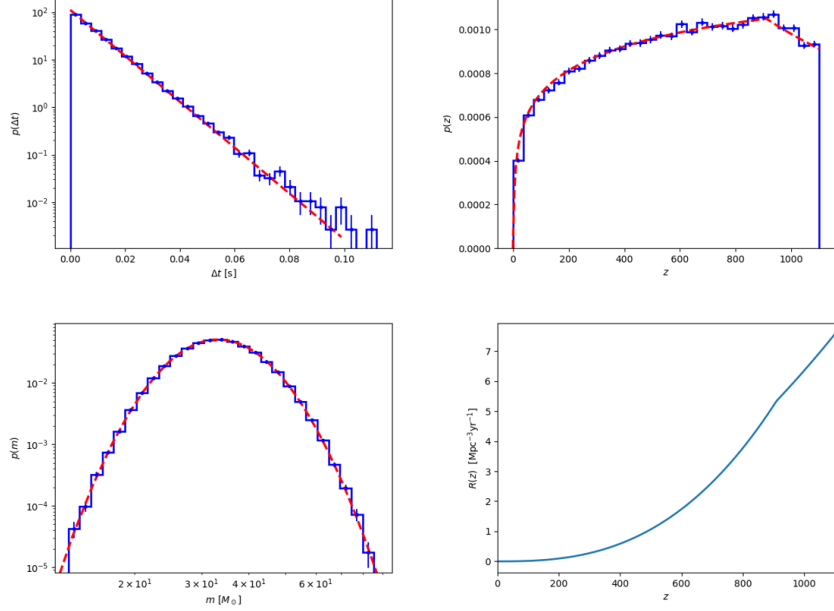


Figure A.5: Parameters sampled for an extended log-normal mass function of early binaries of  $35 M_{\odot}$  PBHs. In the top left panel the distribution of time intervals is depicted. The top right panel represents the redshift probability distribution function, while the bottom left panel shows the mass function. Lastly, in the bottom right panel the merger rate as a function of redshift is depicted. The red lines are the theoretical distributions, while the blue histograms collect the events we sample for the catalog.

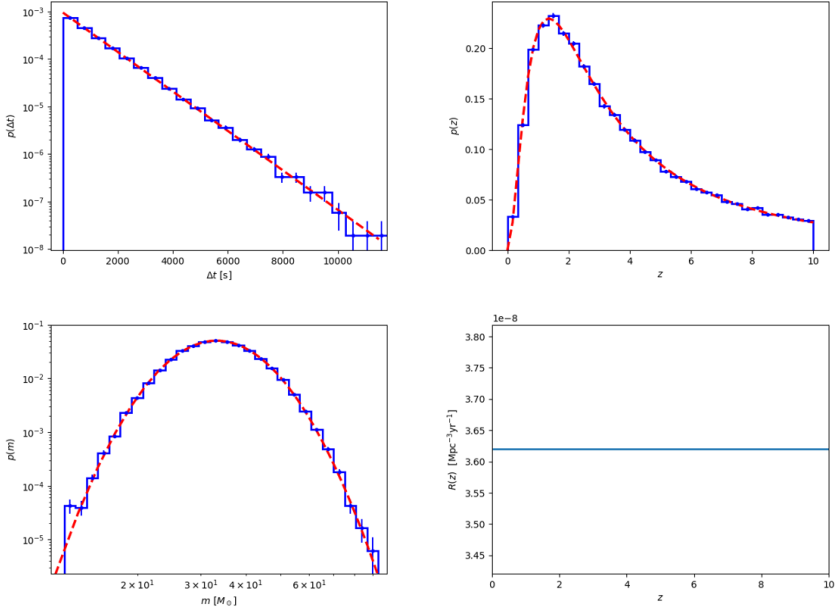


Figure A.6: Parameters sampled for an extended log-normal mass function of late binaries of  $35 M_{\odot}$  PBHs. In the top left panel the distribution of time intervals is depicted. The top right panel represents the redshift probability distribution function, while the bottom left panel shows the mass function. Lastly, in the bottom right panel the merger rate as a function of redshift is depicted. The red lines are the theoretical distributions, while the blue histograms collect the events we sample for the catalog.

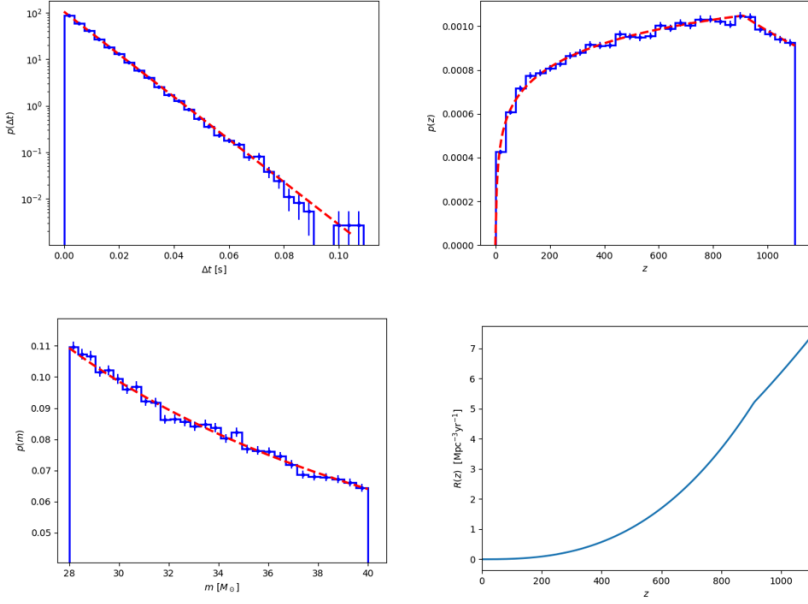


Figure A.7: Parameters sampled for an extended power-law mass function of early binaries of  $28M_\odot < M_{PBH} < 40M_\odot$  PBHs. In the top left panel the distribution of time intervals is depicted. The top right panel represents the redshift probability distribution function, while the bottom left panel shows the mass function. Lastly, in the bottom right panel the merger rate as a function of redshift is depicted. The red lines are the theoretical distributions, while the blue histograms collect the events we sample for the catalog.

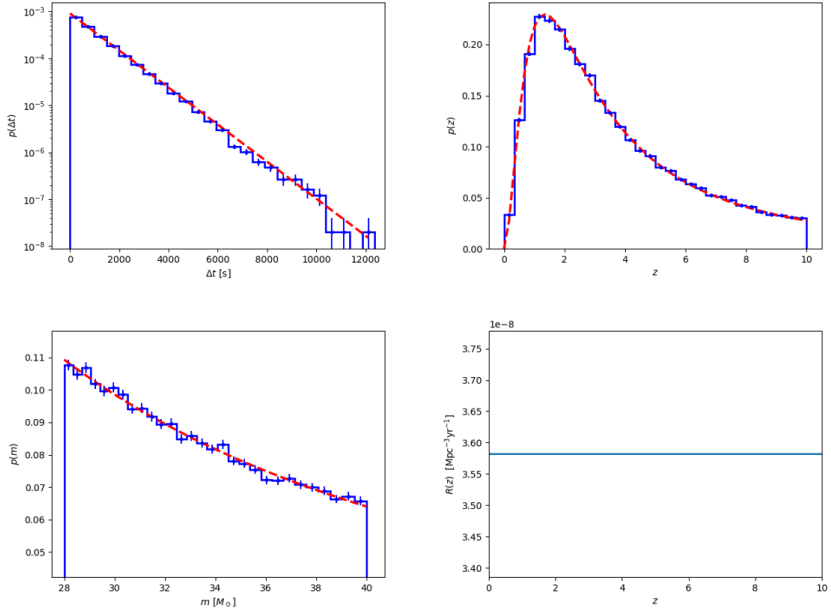


Figure A.8: Parameters sampled for an extended power-law mass function of late binaries of  $28M_\odot < M_{PBH} < 40M_\odot$  PBHs. In the top left panel the distribution of time intervals is depicted. The top right panel represents the redshift probability distribution function, while the bottom left panel shows the mass function. Lastly, in the bottom right panel the merger rate as a function of redshift is depicted. The red lines are the theoretical distributions, while the blue histograms collect the events we sample for the catalog.



# Bibliography

- [1] N. Aghanim *et al.*, “Planck 2018 results. VI. Cosmological parameters,” *Astron. Astrophys.*, vol. 641, p. A6, 2020. [Erratum: *Astron.Astrophys.* 652, C4 (2021)].
- [2] D. H. Lyth and A. R. Liddle, *The primordial density perturbation: Cosmology, inflation and the origin of structure*. Cambridge Univ. Press, 2009.
- [3] W. Keel, *The Road to Galaxy Formation*. Springer Praxis Books, Springer Berlin Heidelberg, 2009.
- [4] S. Dodelson, *Modern cosmology*. San Diego, CA: Academic Press, 2003.
- [5] [https://wmap.gsfc.nasa.gov/universe/uni\\_shape.html](https://wmap.gsfc.nasa.gov/universe/uni_shape.html). NASA/WMAP Science Team, Sponsor: National Aeronautics and Space Administration, Publication date: 24-01-2014.
- [6] A. Raccanelli, *Tests of Cosmological Structure Growth*. PhD dissertation, University of Portsmouth, 2013.
- [7] K. Schwarzschild, “On the gravitational field of a mass point according to Einstein’s theory,” *Sitzungsber. Preuss. Akad. Wiss. Berlin (Math. Phys.)*, vol. 1916, pp. 189–196, 1916.
- [8] D. Finkelstein, “Past-future asymmetry of the gravitational field of a point particle,” *Phys. Rev.*, vol. 110, pp. 965–967, May 1958.
- [9] A. Heger, C. L. Fryer, S. E. Woosley, N. Langer, and D. H. Hartmann, “How massive single stars end their life,” *The Astrophysical Journal*, vol. 591, pp. 288–300, jul 2003.
- [10] J. R. Oppenheimer and G. M. Volkoff, “On Massive neutron cores,” *Phys. Rev.*, vol. 55, pp. 374–381, 1939.
- [11] S. W. Hawking, “Gravitational radiation from colliding black holes,” *Phys. Rev. Lett.*, vol. 26, pp. 1344–1346, May 1971.
- [12] B. J. Carr and S. W. Hawking, “Black Holes in the Early Universe,” *Monthly Notices of the Royal Astronomical Society*, vol. 168, pp. 399–415, 08 1974.
- [13] J. Silk, “Feedback by massive black holes in gas-rich dwarf galaxies,” *The Astrophysical Journal*, vol. 839, p. L13, apr 2017.
- [14] B. Carr and J. Silk, “Primordial black holes as generators of cosmic structures,” *Monthly Notices of the Royal Astronomical Society*, vol. 478, p. 3756–3775, May 2018.
- [15] B. Carr and F. Kuhnel, “Primordial black holes as dark matter,” 2020.
- [16] M. Sasaki, T. Suyama, T. Tanaka, and S. Yokoyama, “Primordial black holes - perspectives in gravitational wave astronomy -,” 2018.
- [17] F. Zwicky, “Die rotverschiebung von extragalaktischen nebeln,” *Helvetica Physica Acta*, vol. 6, pp. 110–127, 1933.
- [18] G. A. Mamon and E. L. Lokas, “Dark matter in elliptical galaxies — II. Estimating the mass within the virial radius,” *Monthly Notices of the Royal Astronomical Society*, vol. 363, pp. 705–722, 11 2005.

- [19] V. C. Rubin, “The rotation of spiral galaxies,” *Science*, vol. 220, no. 4604, pp. 1339–1344, 1983.
- [20] R. Massey, T. Kitching, and J. Richard, “The dark matter of gravitational lensing,” *Reports on Progress in Physics*, vol. 73, p. 086901, jul 2010.
- [21] B. Carr and F. Kühnel, “Primordial black holes as dark matter candidates,” *SciPost Physics Lecture Notes*, may 2022.
- [22] P. Villanueva-Domingo, O. Mena, and S. Palomares-Ruiz, “A brief review on primordial black holes as dark matter,” *Frontiers in Astronomy and Space Sciences*, vol. 8, may 2021.
- [23] A. M. Green, “Primordial black holes: sirens of the early universe,” 2014.
- [24] A. Kalaja, “Primordial black holes from inflation,” Master’s thesis, Università di Padova, 2018.
- [25] J. L. Bernal, A. Raccanelli, L. Verde, and J. Silk, “Signatures of primordial black holes as seeds of supermassive black holes,” *Journal of Cosmology and Astroparticle Physics*, vol. 2018, pp. 017–017, may 2018.
- [26] A. M. Green and B. J. Kavanagh, “Primordial black holes as a dark matter candidate,” *Journal of Physics G: Nuclear and Particle Physics*, vol. 48, p. 043001, feb 2021.
- [27] S. W. Hawking, I. G. Moss, and J. M. Stewart, “Bubble collisions in the very early universe,” *Phys. Rev. D*, vol. 26, pp. 2681–2693, Nov 1982.
- [28] A. M. Dizgah, G. Franciolini, and A. Riotto, “Primordial black holes from broad spectra: abundance and clustering,” *Journal of Cosmology and Astroparticle Physics*, vol. 2019, pp. 001–001, nov 2019.
- [29] S. Clesse and J. García-Bellido, “The clustering of massive primordial black holes as dark matter: Measuring their mass distribution with advanced LIGO,” *Physics of the Dark Universe*, vol. 15, pp. 142–147, mar 2017.
- [30] M. Mirbabayi, A. Gruzinov, and J. Noreñ a, “Spin of primordial black holes,” *Journal of Cosmology and Astroparticle Physics*, vol. 2020, pp. 017–017, mar 2020.
- [31] M. Trashorras, J. García-Bellido, and S. Nesseris, “The clustering dynamics of primordial black holes in n-body simulations,” *Universe*, vol. 7, no. 1, 2021.
- [32] K. M. Belotsky, V. I. Dokuchaev, Y. N. Eroshenko, E. A. Esipova, M. Y. Khlopov, L. A. Khromykh, A. A. Kirillov, V. V. Nikulin, S. G. Rubin, and I. V. Svadkovsky, “Clusters of primordial black holes,” *The European Physical Journal C*, vol. 79, mar 2019.
- [33] S. W. Hawking, “Black hole explosions?,” *Nature*, vol. 248, pp. 30–31, 1974.
- [34] B. Carr, F. Kühnel, and M. Sandstad, “Primordial black holes as dark matter,” *Phys. Rev. D*, vol. 94, p. 083504, Oct 2016.
- [35] M. Raidal, C. Spethmann, V. Vaskonen, and H. Veermäe, “Formation and evolution of primordial black hole binaries in the early universe,” *Journal of Cosmology and Astroparticle Physics*, vol. 2019, pp. 018–018, feb 2019.
- [36] V. D. Luca, G. Franciolini, P. Pani, and A. Riotto, “The minimum testable abundance of primordial black holes at future gravitational-wave detectors,” *Journal of Cosmology and Astroparticle Physics*, vol. 2021, p. 039, nov 2021.
- [37] S. Clesse and J. García-Bellido, “Detecting the gravitational wave background from primordial black hole dark matter.” <https://doi.org/10.48550/arxiv.1610.08479>, 2016.
- [38] J. H. MacGibbon and B. R. Webber, “Quark- and gluon-jet emission from primordial black holes: The instantaneous spectra,” *Phys. Rev. D*, vol. 41, pp. 3052–3079, May 1990.
- [39] D. N. Page and S. W. Hawking, “Gamma rays from primordial black holes.,” *The Astrophysical Journal*, vol. 206, pp. 1–7, May 1976.

- [40] W. DeRocco and P. W. Graham, “Constraining primordial black hole abundance with the galactic 511 kev line,” *Phys. Rev. Lett.*, vol. 123, p. 251102, Dec 2019.
- [41] M. Boudaud and M. Cirelli, “Voyager 1  $e^{\pm}$  further constrain primordial black holes as dark matter,” *Phys. Rev. Lett.*, vol. 122, p. 041104, Jan 2019.
- [42] A. Einstein, “Lens-like action of a star by the deviation of light in the gravitational field,” *Science*, vol. 84, no. 2188, pp. 506–507, 1936.
- [43] C. Alcock, R. A. Allsman, D. R. Alves, T. S. Axelrod, A. C. Becker, D. P. Bennett, K. H. Cook, N. Dalal, A. J. Drake, K. C. Freeman, M. Geha, K. Griest, M. J. Lehner, S. L. Marshall, D. Minniti, C. A. Nelson, B. A. Peterson, P. Popowski, M. R. Pratt, P. J. Quinn, C. W. Stubbs, W. Sutherland, A. B. Tomaney, T. Vandehei, and D. Welch, “The MACHO project: Microlensing results from 5.7 years of large magellanic cloud observations,” *The Astrophysical Journal*, vol. 542, pp. 281–307, oct 2000.
- [44] EROS Collaboration and N. P.-D. e. al, “Microlensing towards the small magellanic cloud. eros 2 first year survey,” 1997.
- [45] I. Soszynski, R. Poleski, A. Udalski, M. K. Szymanski, M. Kubiaik, G. Pietrzynski, L. Wyrzykowski, O. Szewczyk, and K. Ulaczyk, “The optical gravitational lensing experiment. the ogle-iii catalog of variable stars. i. classical cepheids in the large magellanic cloud,” 2008.
- [46] The LIGO Scientific Collaboration, The Virgo Collaboration, The KAGRA Collaboration, and R. Abbott et al., “Gwtc-3: Compact binary coalescences observed by ligo and virgo during the second part of the third observing run,” 2021.
- [47] R. Murgia, G. Scelfo, M. Viel, and A. Raccaelli, “Lyman-  $\alpha$  forest constraints on primordial black holes as dark matter,” *Physical Review Letters*, vol. 123, aug 2019.
- [48] H. Niikura, M. Takada, N. Yasuda, R. H. Lupton, T. Sumi, S. More, T. Kurita, S. Sugiyama, A. More, M. Oguri, and M. Chiba, “Microlensing constraints on primordial black holes with subaru/HSC andromeda observations,” *Nature Astronomy*, vol. 3, pp. 524–534, apr 2019.
- [49] H. Niikura, M. Takada, S. Yokoyama, T. Sumi, and S. Masaki, “Constraints on earth-mass primordial black holes from ogle 5-year microlensing events,” *Phys. Rev. D*, vol. 99, p. 083503, Apr 2019.
- [50] L. Wyrzykowski and I. Mandel, “Constraining the masses of microlensing black holes and the mass gap with Gaia DR2,” *Astronomy & Astrophysics*, vol. 636, p. A20, apr 2020.
- [51] M. R. S. Hawkins, “The signature of primordial black holes in the dark matter halos of galaxies,” *Astronomy & Astrophysics*, vol. 633, p. A107, jan 2020.
- [52] E. Mediavilla, J. Jiménez-Vicente, J. A. Muñoz, H. Vives-Arias, and J. Calderón-Infante, “Limits on the mass and abundance of primordial black holes from quasar gravitational microlensing,” *The Astrophysical Journal*, vol. 836, p. L18, feb 2017.
- [53] N. Cappelluti, A. Kashlinsky, R. G. Arendt, A. Comastri, G. G. Fazio, A. Finoguenov, G. Hasinger, J. C. Mather, T. Miyaji, and S. H. Moseley, “Cross-correlating Cosmic Infrared and X-Ray Background Fluctuations: Evidence of Significant Black Hole Populations among the CIB Sources,” *The Astrophysical Journal*, vol. 769, p. 68, May 2013.
- [54] S. Bird, I. Cholis, J. B. Muñoz, Y. Ali-Haïmoud, M. Kamionkowski, E. D. Kovetz, A. Raccaelli, and A. G. Riess, “Did ligo detect dark matter?,” *Physical Review Letters*, vol. 116, May 2016.
- [55] M. Sasaki, T. Suyama, T. Tanaka, and S. Yokoyama, “Primordial black hole scenario for the gravitational-wave event gw150914,” *Phys. Rev. Lett.*, vol. 117, p. 061101, Aug 2016.
- [56] N. Fernandez and S. Profumo, “Unraveling the origin of black holes from effective spin measurements with LIGO-virgo,” *Journal of Cosmology and Astroparticle Physics*, vol. 2019, pp. 022–022, aug 2019.

- [57] R. Abbott, T. D. Abbott, S. Abraham, F. Acernese, K. Ackley, and Adams, “Gw190521: A binary black hole merger with a total mass of 150  $M_{\odot}$ ,” *Phys. Rev. Lett.*, vol. 125, p. 101102, Sep 2020.
- [58] Y. Ali-Haïmoud, E. D. Kovetz, and M. Kamionkowski, “Merger rate of primordial black-hole binaries,” *Phys. Rev. D*, vol. 96, p. 123523, Dec 2017.
- [59] M. Turner, “Gravitational radiation from point-masses in unbound orbits: Newtonian results.,” *The Astrophysical Journal*, vol. 216, pp. 610–619, Sept. 1977.
- [60] J. García-Bellido, S. Jaraba, and S. Kuroyanagi, “The stochastic gravitational wave background from close hyperbolic encounters of primordial black holes in dense clusters,” *Physics of the Dark Universe*, vol. 36, p. 101009, jun 2022.
- [61] M. Gröbner, P. Jetzer, M. Haney, S. Tiwari, and W. Ishibashi, “A note on the gravitational wave energy spectrum of parabolic and hyperbolic encounters,” *Classical and Quantum Gravity*, vol. 37, p. 067002, feb 2020.
- [62] L. Valbusa Dall’Armi, E. Vanzan, S. Libanore, N. Bellomo, and A. RAccanelli, “*In prep:* Stochastic gravitational wave background from astrophysical and primordial black holes in star clusters,” 2022.
- [63] M. Maggiore, *Gravitational Waves. Vol. 1: Theory and Experiments*. Oxford Master Series in Physics, Oxford University Press, 2007.
- [64] B. Schutz, *A First Course in General Relativity*. Cambridge University Press, 2nd ed., June 2009.
- [65] R. Abbott et al., “Open data from the first and second observing runs of advanced ligo and advanced virgo,” *SoftwareX*, vol. 13, p. 100658, 2021.
- [66] R. A. Hulse and J. H. Taylor, “Discovery of a pulsar in a binary system.,” *The Astrophysical Journal*, vol. 195, pp. L51–L53, Jan. 1975.
- [67] J. M. Weisberg and J. H. Taylor, “Relativistic binary pulsar b1913+16: Thirty years of observations and analysis,” 2004.
- [68] B. P. Abbott et al., “Observation of gravitational waves from a binary black hole merger,” *Phys. Rev. Lett.*, vol. 116, p. 061102, Feb 2016.
- [69] C. J. Moore, R. H. Cole, and C. P. L. Berry, “Gravitational-wave sensitivity curves,” *Classical and Quantum Gravity*, vol. 32, p. 015014, dec 2014.
- [70] <https://www.ligo.caltech.edu/image/ligo20211107a>. LIGO-Virgo / Aaron Geller / Northwestern University, Publication date: 7-11-2021.
- [71] M. Maiorano, F. D. Paolis, and A. A. Nucita, “Principles of gravitational-wave detection with pulsar timing arrays,” *Symmetry*, vol. 13, p. 2418, dec 2021.
- [72] J. P. W. Verbiest et al., “The international pulsar timing array: First data release,” *Monthly Notices of the Royal Astronomical Society*, vol. 458, pp. 1267–1288, feb 2016.
- [73] P. E. Dewdney, P. J. Hall, R. T. Schilizzi, and T. J. L. W. Lazio, “The Square Kilometre Array,” *IEEE Proceedings*, vol. 97, pp. 1482–1496, Aug. 2009.
- [74] P. Amaro-Seoane et al., “Laser interferometer space antenna,” 2017.
- [75] M. Maggiore et al., “Science case for the einstein telescope,” *Journal of Cosmology and Astroparticle Physics*, vol. 2020, pp. 050–050, mar 2020.
- [76] N. Christensen, “Stochastic gravitational wave backgrounds,” *Reports on Progress in Physics*, vol. 82, p. 016903, nov 2018.
- [77] C. Caprini and D. G. Figueroa, “Cosmological backgrounds of gravitational waves,” *Classical and Quantum Gravity*, vol. 35, p. 163001, jul 2018.

- [78] T. Regimbau, “The astrophysical gravitational wave stochastic background,” *Research in Astronomy and Astrophysics*, vol. 11, pp. 369–390, mar 2011.
- [79] P. S. Behroozi, R. H. Wechsler, and C. Conroy, “The average star formation histories of galaxies in dark matter halos from  $z=0\text{--}8$ ,” *The Astrophysical Journal*, vol. 770, p. 57, may 2013.
- [80] N. Bellomo, D. Bertacca, A. C. Jenkins, S. Matarrese, A. Raccanelli, T. Regimbau, A. Ricciardone, and M. Sakellariadou, “CLASS\_GWB: robust modeling of the astrophysical gravitational wave background anisotropies,” *Journal of Cosmology and Astroparticle Physics*, vol. 2022, p. 030, jun 2022.
- [81] G. Morrás, J. García-Bellido, and S. Nesseris, “Search for black hole hyperbolic encounters with gravitational wave detectors,” *Physics of the Dark Universe*, vol. 35, p. 100932, 2022.
- [82] S. Mukherjee, S. Mitra, and S. Chatterjee, “Gravitational wave observatories may be able to detect hyperbolic encounters of black holes,” *Monthly Notices of the Royal Astronomical Society*, vol. 508, pp. 5064–5073, Dec. 2021.
- [83] M. Abramowitz and I. A. Stegun, eds., *Handbook of Mathematical Functions with Formulas, Graphs, and Mathematical Tables*. Washington, DC, USA: U.S. Government Printing Office, tenth printing ed., 1972.
- [84] M. Carmeli, J. G. Hartnett, and F. J. Oliveira, “The cosmic time in terms of the redshift,” *Foundations of Physics Letters*, vol. 19, pp. 277–283, apr 2006.
- [85] P. Ajith, M. Hannam, S. Husa, Y. Chen, B. Brügmann, N. Dorband, D. Müller, F. Ohme, D. Pollney, C. Reisswig, L. Santamaría, and J. Seiler, “Inspiral-merger-ringdown waveforms for black-hole binaries with nonprecessing spins,” *Physical Review Letters*, vol. 106, jun 2011.
- [86] L. Liu, Z.-K. Guo, and R.-G. Cai, “Effects of the merger history on the merger rate density of primordial black hole binaries,” *The European Physical Journal C*, vol. 79, aug 2019.
- [87] K. W. Wong, G. Franciolini, V. D. Luca, V. Baibhav, E. Berti, P. Pani, and A. Riotto, “Constraining the primordial black hole scenario with bayesian inference and machine learning: The GWTC-2 gravitational wave catalog,” *Physical Review D*, vol. 103, jan 2021.
- [88] O. Truttero, “Non-gaussianity and merger rate of primordial black holes,” Master’s thesis, Università di Padova, 2021.
- [89] S. Hild, S. Chelkowski, and A. Freise, “Pushing towards the ET sensitivity using ‘conventional’ technology,” 10 2008.
- [90] E. Collaboration, “Base sensitivity.”
- [91] E. Thrane and J. D. Romano, “Sensitivity curves for searches for gravitational-wave backgrounds,” *Physical Review D*, vol. 88, dec 2013.
- [92] N. Aggarwal *et al.*, “Challenges and opportunities of gravitational-wave searches at MHz to GHz frequencies,” *Living Rev. Rel.*, vol. 24, no. 1, p. 4, 2021.
- [93] A. Berlin, D. Blas, R. T. D’Agnolo, S. A. Ellis, R. Harnik, Y. Kahn, and J. Schütte-Engel, “Detecting high-frequency gravitational waves with microwave cavities,” *Physical Review D*, vol. 105, jun 2022.
- [94] S. Shandera, D. Jeong, and H. S. G. Gebhardt, “Gravitational waves from binary mergers of subsolar mass dark black holes,” *Physical Review Letters*, vol. 120, jun 2018.
- [95] N. Bellomo, J. L. Bernal, A. Raccanelli, and L. Verde, “Primordial black holes as dark matter: converting constraints from monochromatic to extended mass distributions,” *Journal of Cosmology and Astroparticle Physics*, vol. 2018, pp. 004–004, jan 2018.
- [96] K. S. Thorne. 2017 Interview, Nobelprize.org, Nobel Media AB 2014, Web, 25 Oct 20, [https://www.nobelprize.org/nobel\\_prizes/physics/laureates/2017/thorne-interview.html](https://www.nobelprize.org/nobel_prizes/physics/laureates/2017/thorne-interview.html).